Publicly Accessible Penn Dissertations

2017

Mechanics Of Fluctuating Elastic Plates And Fiber Networks

Xiaojun Liang

University of Pennsylvania, liangxj_156@163.com

Mechanics Of Fluctuating Elastic Plates And Fiber Networks

Abstract

Lipid membranes and fiber networks in biological systems perform important mechanical functions at the cellular and tissue levels. In this thesis I delve into two detailed problems -- thermal fluctuation of membranes and non-linear compression response of fiber networks. Typically, membrane fluctuations are analysed by decomposing into normal modes or by molecular simulations. In the first part of my thesis, I propose a new semi-analytic method to calculate the partition function of a membrane. The membrane is viewed as a fluctuating von Karman plate and discretized into triangular elements. Its energy is expressed as a function of nodal displacements, and then the partition function and co-variance matrix are computed using Gaussian integrals. I recover well-known results for the dependence of the projected area of a lipid bilayer membrane on the applied tension, and recent simulation results on the ependence of membrane free energy on geometry, spontaneous curvature and tension. As new applications I use this technique to study a membrane with heterogeneity and different boundary conditions. I also use this technique to study solid membranes by taking account of the non-linear coupling of in-plane strains with out-of-plane deflections using a penalty energy, and apply it to graphene, an ultra-thin two-dimensional solid. The scaling of graphene fluctuations with membrane size is recovered. I am able to capture the dependence of the thermal expansion coefficient of graphene on temperature. Next, I study curvature mediated interactions between inclusions in membranes. I assume the inclusions to be rigid, and show that the elastic and entropic forces between them can compete to yield a local maximum in the free energy if the membrane bending modulus is small. If the spacing between the inclusions is less than this local maximum then the attractive entropic forces dominate and the separation between the inclusions will be determined by short range interactions; if the spacing is more than the local maximum then the elastic repulsive forces dominate and the inclusions will move further apart. This technique can be extended to account for entropic effects in other methods which rely on quadratic energies to study the interactions of inclusions in membranes. In the second part of this thesis I study the compression response of two fiber network materials -- blood clots and carbon nanotube forests. The stress-strain curve of both materials reveals four characteristic regions, for compression-decompression: 1) linear elastic region; 2) upper plateau or softening region; 3) non-linear elastic region or re-stretching of the network; 4) lower plateau in which dissociation of some newly made connections occurs. This response is described by a phase transition based continuum model. The model is inspired by the observation of one or more moving interfaces across which densified and rarefied phases of fibers co-exist. I use a quasi-static version of the Abeyaratne-Knowles theory of phase transitions for continua with a stick-slip type kinetic law and a nucleation criterion based on the

critical stress for buckling to describe the formation and motion of these interfaces in uniaxial compression experiments. Our models could aid the design of biomaterials and carbon nanotube forests to have desired mechanical properties and guide further understanding of their behavior under large deformations.

Degree Type
Dissertation

Degree Name
Doctor of Philosophy (PhD)

Graduate Group
Mechanical Engineering & Applied Mechanics

First Advisor
Prashant K. Purohit

Subject Categories
Biomechanics | Engineering Mechanics | Mechanics of Materials

MECHANICS OF FLUCTUATING ELASTIC PLATES AND FIBER NETWORKS

Xiaojun Liang

A DISSERTATION

in

Mechanical Engineering and Applied Mechanics

Presented to the Faculties of the University of Pennsylvania

in

Partial Fulfillment of the Requirements for the

Degree of Doctor of Philosophy

2017

Supervisor of Dissertation:

Prashant K. Purohit, Associate Professor
Department of Mechanical Engineering and Applied Mechanics

Graduate Group Chairperson:

Kevin T. Turner, Professor, and Associate Chair for Graduate Affairs and Graduate Group
Chair, Department of Mechanical Engineering and Applied Mechanics

Dissertation Committee:

John L. Bassani, Richard H. and S.L. Gabel Professor
Department of Mechanical Engineering and Applied Mechanics

Kevin T. Turner, Professor, and Associate Chair for Graduate Affairs and Graduate Group
Chair, Department of Mechanical Engineering and Applied Mechanics

Ravi Radhakrishnan, Professor
Department of Chemical and Biomolecular Engineering
Department of Bioengineering

MECHANICS OF FLUCTUATING ELASTIC PLATES AND FIBER NETWORKS

Acknowledgments

I am raised in a family of teachers. It was my parents who strongly supported me to finish my bachelor degree and guided me to pursue the PhD degree at the University of Pennsylvania. Without their help and encouragement I could not have had the opportunity to study at this beautiful campus.

It is a great pleasure to work with my PhD advisor, Dr. Prashant K. Purohit. He is a very nice and knowledgeable gentleman, and willing to patiently share both his ideas and experience with me. I would like to express my sincere gratitude to him for being an enthusiastic mentor as well as a reliable friend. I deeply appreciate the help I received from Oleg Kim, Dr. Irina Chernysh, Dr. Rustem Litvinov and Dr. John Weisel with whom I collaborated while researching blood clots. It was a pleasure also to work with Jungho Shin, Daniel Magagnosc, Yijie Jiang, Dr. Sei-Jin Park, Dr. John Hart and Dr. Daniel Gianola with whom I wrote the chapter on carbon nanotube forests. Their enlightening suggestions helped me conquer the difficulties in my thesis step by step. I would like to thank Dr. John L. Bassani, Dr. Kevin Turner, and Dr. Ravi Radhakrishnan whom I have the privilege to have in my dissertation committee.

My thanks also go to my senior lab mates Tianxiang Su, Qiwei Shi, Xin Wang, Reza Avazmohammadi, Morteza Hakimi Siboni, David Argudo, Sheng Mao, and Qingze Zhao, who offered me useful suggestions and timely help for both my research and life at Penn. I also thank my friends Xiaoguai Li, Chenchen Liu, Dawei Song, Jaspreet Singh, and Shuvrangsu Das, who are my colleagues in the lab. We share an enjoyable and treasurable journey to the same target - PhD graduation.

I also want to thank my roommate Yanhao Dong, and other friends who also

ABSTRACT

MECHANICS OF FLUCTUATING ELASTIC PLATES AND FIBER
NETWORKS

Xiaojun Liang

Prashant K. Purohit

Lipid membranes and fiber networks in biological systems perform important mechanical functions at the cellular and tissue levels. In this thesis I delve into two detailed problems – thermal fluctuation of membranes and non-linear compression response of fiber networks. Typically, membrane fluctuations are analysed by decomposing into normal modes or by molecular simulations. In the first part of my thesis, I propose a new semi-analytic method to calculate the partition function of a membrane. The membrane is viewed as a fluctuating von Karman plate and discretized into triangular elements. Its energy is expressed as a function of nodal displacements, and then the partition function and co-variance matrix are computed using Gaussian integrals. I recover well-known results for the dependence of the projected area of a lipid bilayer membrane on the applied tension, and recent simulation results on the dependence of membrane free energy on geometry, spontaneous curvature and tension. As new applications I use this technique to study a membrane with heterogeneity and different boundary conditions. I also use this technique to study solid membranes by taking account of the non-linear coupling of in-plane strains with out-of-plane deflections using a penalty energy, and apply it to graphene, an ultra-thin two-dimensional solid. The scaling of graphene fluctuations with membrane size is recovered. I am able to capture the dependence of the thermal expansion coefficient of graphene on temperature. Next, I study curvature mediated interactions between inclusions in membranes. I assume the inclusions to be rigid, and show that the elastic and entropic forces between them can compete to yield a local maximum in the free energy if the membrane bending modulus is small. If the spacing between the inclusions is less than this local maximum then the attractive entropic forces dominate and the separation between the inclusions will be determined by short range interactions; if the spacing is more than the local maximum then the elastic repulsive forces dominate and the inclusions will move further apart. This technique can be extended to account for entropic effects in other methods which rely on quadratic energies

to study the interactions of inclusions in membranes. In the second part of this thesis I study the compression response of two fiber network materials – blood clots and carbon nanotube forests. The stress-strain curve of both materials reveals four characteristic regions, for compression-decompression: 1) linear elastic region; 2) upper plateau or softening region; 3) non-linear elastic region or re-stretching of the network; 4) lower plateau in which dissociation of some newly made connections occurs. This response is described by a phase transition based continuum model. The model is inspired by the observation of one or more moving interfaces across which densified and rarefied phases of fibers co-exist. I use a quasi-static version of the Abeyaratne-Knowles theory of phase transitions for continua with a stick-slip type kinetic law and a nucleation criterion based on the critical stress for buckling to describe the formation and motion of these interfaces in uniaxial compression experiments. Our models could aid the design of biomaterials and carbon nanotube forests to have desired mechanical properties and guide further understanding of their behavior under large deformations.

Contents

List of Tables

List of Figures

xviii

Chapter 1

Introduction

Living cells are able to sense external mechanical forces and react to them both chemically and mechanically. The boundary between the interior and exterior of the cell is the plasma membrane. It serves as a protecting shell for the cell organelles as shown in Figure 1.1a. This membrane has a very complex structure, and elaborate assembly of distinct components is required for morphological or topological change in its shape. It mainly consists of an organized bilayer of lipids, which are fatty acid molecules surrounded by fluid. The bilayer is about 5 nm thick with a bending modulus around 20 $k_B T$ at $T = 300$ K. It is stable against thermal motions, but is considerably soft to be flexible for shape transformation. The cell membrane is regarded as a fluid interface, thermodynamic properties of which are influenced by its stretching and bending stiffness, induced curvature field and thermal fluctuations Ramakrishnan et al. (2014). In addition to the lipid bilayer, the cell membrane itself also has a large number of proteins embedded in it and is often described in terms of the 'fluid mosaic model' (see Figure 1.1b). The embedded proteins occupy volume fraction between 18% to 75% with a corresponding ratio of numbers of protein to lipid varying from $0.23 - 1.6$ Guidotti (1972). The embedded proteins can diffuse on the membrane and can interact with each other and with the lipids in the membrane sterically, electrostatically, mechanically and through other means. Their interactions are the key factor determining the shape and thus function of the cell membrane. The cell membrane is supported underneath by the cytoskeleton which is a mesh-work of filaments that extends throughout the cytoplasm (see Figure 1.1c) and could include actin, spectrin, intermediate filaments, microtubules and proteins that cross-link them. It works intimately with the cell membrane

1
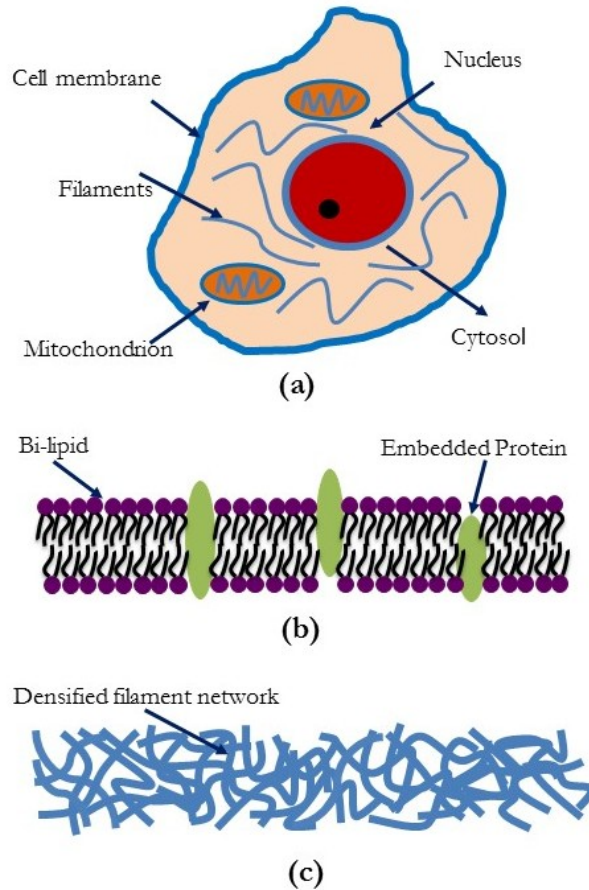
Figure 1.1: (a) Schematic diagram of a typical cell structure, which contains many in-cell organelles. (b) Schematic diagram of a lipid bilyer membrane, whose mechanical rigidity is altered by the presence of embedded protein molecules. (c) Schematic diagram of a filament network.

to spatially organize the components of the cell, and also connects the cell physically and biologically to the surrounding substance in its exterior. It helps a cell to resist deformation, to transport cross-cellular force and to adjust shape during functioning Fletcher & Mullins (2010). Both in-cell and cross-cell physical forces can act on the cytoskeleton to modify local mechanical properties and biological function. The exterior of the cell often consists of a matrix of filaments called the extra-cellular matrix (ECM). Much of the biology of a cell depends on the mechanics of the ECM. Therefore, it is extremely important to understand quantitatively the mechanics of cell membranes, cytoskeleton and the ECM.

Mechanical and thermodynamic properties of the cell membrane have been quantitatively studied using *in vitro* experimental methods Evans & Rawicz (1990). These studies from a few decades ago have revealed that in the mechanics of cell membranes, thermal fluc-

tuations play an important role Helfrich (1973), Weeks (1977). Early analytic results that successfully explained the behavior of liquid-vapor interfaces also explained the fluctuations of lipid bilayers Helfrich (1975), Milner & Safran (1987), Boal & Boal (2012). Following this idea, people developed analytic Helfrich (1973, 1975), Evans (1974) and computational methods Weeks (1977), Milner & Safran (1987) to understand how lipid membranes respond mechanically and thermodynamically to different applied loading and boundary conditions. Later, atomic modeling methods were applied to understand highly complex two-dimensional systems, such as lipid bilayers, by using sophisticated computational techniques Lindahl & Edholm (2000). Both experimental and computational methods were able to determine not just how lipids assemble to form membranes, but also how membrane inclusions sense local membrane curvature, and then affect membrane local structure (lipid bilayer thickness, tilt of the lipids, etc.). However, it is not always possible to design an experiment for large scale problems involving membrane protein interactions, and also the sample scale is too large for molecular simulations. To overcome these difficulties, researchers turned to continuum modeling to study large scale (more than several microns) membrane-protein problems. In this approach the lipid membrane is treated as a thin plate because its in-plane dimensions are much larger than its thickness. The infinite microscopic degrees of freedom of the two dimensional system are represented by several macroscopic variables of the plate that define the system mechanical and thermodynamic properties. Similar strategies together with molecular dynamic tools are applied to extract the mechanical properties of two-dimensional solids, such as, graphene Fasolino et al. (2007) and polymeric membranes Rodríguez-García et al. (2011). These two-dimensional solids are regarded as elastic plates suffering from out-of-plane fluctuation. However, the term 'membrane' is more commonly used in the literature for these two-dimensional systems. In this thesis I will use 'plate' and 'membrane' interchangeably when referring to these objects.

While the effect of thermal fluctuations on the mechanics of homogeneous lipid membranes is relatively well understood, the same cannot be said about heterogeneous lipid membranes, such as those that have proteins embedded in them or have domains in which different types of lipids are present. One of our goals in this thesis is to study exactly this type of heterogeneous membranes. Most treatments of such membranes in the computational/theoretical literature are based on Fourier methods and/or Monte Carlo, molecular dynamics or Brownian dynamics computations which require significant computational re-

sources. We propose a different semi-analytic technique that requires much less computational effort and can be used to study two-dimensional systems which involve elastic and entropic effects, such as, fluctuating heterogeneous lipid membranes, fluctuating graphene sheets and protein interactions on lipid membranes.

We treat inclusions, such as proteins, in lipid membranes as defects in a solid (imagine an impurity atom occupying a site in a crystal lattice). In mechanics the forces of interaction between defects in an elastic body are well understood. For example, two screw dislocations with Burger's vectors b and b' at a distance r from each other interact with a force per unit length F of magnitude $F = \mu bb'/(2\pi r)$ where μ is the shear modulus of the solid. This interaction force arises because the defects produce elastic fields around them which can overlap. The interaction between the defects could be attractive or repulsive depending on whether the total elastic energy of the solid decreases or increases due to the overlapping of stress and strain fields produced by the defects Weertman & Weertman (1992). Interactions between defects in an elastic solid can also arise due to entropic effects. For example, the equilibrium concentration of vacancies in a solid is a result of the competition between the elastic energy and the entropy of the vacancies. The elastic part of the free energy of the solid, U_{el}, increases if the vacancy concentration increases because the vacancies create elastic fields around them that store energy. On the other hand, the entropic part of the free energy of the solid decreases as the vacancy concentration increases because the entropic part of the free energy goes as $-TS \approx -Tk_B(c \log c + (1-c)\log(1-c))$ for dilute vacancy concentrations, or $c << 1$. This competition gives rise to a non-zero vacancy concentration at which the free energy is a minimum Christian (2002). In a similar vein, the chemical force on a dislocation has its origins in the entropy of vacancies Weertman & Weertman (1992). The physics of elastic and entropic interactions described above is applicable to any kind of defect of in an elastic material. Since lipid membranes can be modeled as elastic continua we will apply concepts similar to those described above to inclusions, such as proteins, in them.

While lipid membranes could be studied *in vitro*, the cytoskeleton is not a simple and isolated object that could be completely studied without other cell organelles. However, its structure as an isotropic filament network has been identified and reconstructed *in vitro* to circumvent cell complexity Zagar et al. (2011). Researchers have used both experimental and computational methods to understand its mechanical response under different applied

loading condition Howard et al. (2001), Huisman et al. (2007), Stricker et al. (2010). It has been realized that their mechanics in compression is similar to that of foams Gent & Thomas (1959, 1963). Recall that foams or cellular solids, like networks, consist of interconnected solid material and large voids that contain fluids like air or water. Examples of other natural foam material are bone, wood and cork, which have a prismatic, or honeycomb-like cells that support the overall structure. Following this realization materials with a similar cellular structure are being designed, such as carbon nanotube (CNT) forests Cao et al. (2005) and porous scaffolds in tissue engineering Gibson (2005). The mechanical response of a foam material strongly depends on that of the solid making up the foam, as well as its microstructural features, especially the length of filament between cross-links and the volume fraction of the solid filaments. The volume fraction is also equivalent to the ratio of the density of the cellular solid to that of the solid it is made from, which is called the relative density in literature Gibson & Ashby (1999), Gibson (2005). The volume fraction of the filament ranges from 0.1 to 0.4 for different kind of materials, and could be as low as 0.001 for special ultra-low-density foams. People started to represent the foam structure by an organized model of repeating unit cells, such as a hexagon in two dimensions, a cube or dodecahedron in three dimension as in Ko (1965), Finnie & Patel (1970), Gibson & Ashby (1982). On the other hand, dimensional analysis is also used to estimate the stiffness of foam network without specifying the exact geometrical model for single cell as done by Gibson and Ashby Gibson & Ashby (1999). This shows that the expression for axial and shear stiffness of foam material is proportional to the length scale between cross-links and the volume fraction of the solid filaments, and leaves the coefficient to be determined by experiment. Other than theoretical methods, computational methods such as the finite element method have also been developed to understand random foam structures as in Silva et al. (1995), Van der Burg et al. (1997). Finite element models are able to include imperfections in the foam structure as in Chen et al. (2001).

In recent biophysical studies of filament networks most attention has been devoted to shear loading, but little has been done for compressive loading. When filament networks are loaded in compression they give stress-strain curves that are similar to those of foams which have three regions. In the small strain region, there is an initial linear relation between stress and strain which is similar to any elastic solid. In this region, the stiffness is well understood and can be obtained by considering a unit cell or by dimensional analysis Gibson & Ashby
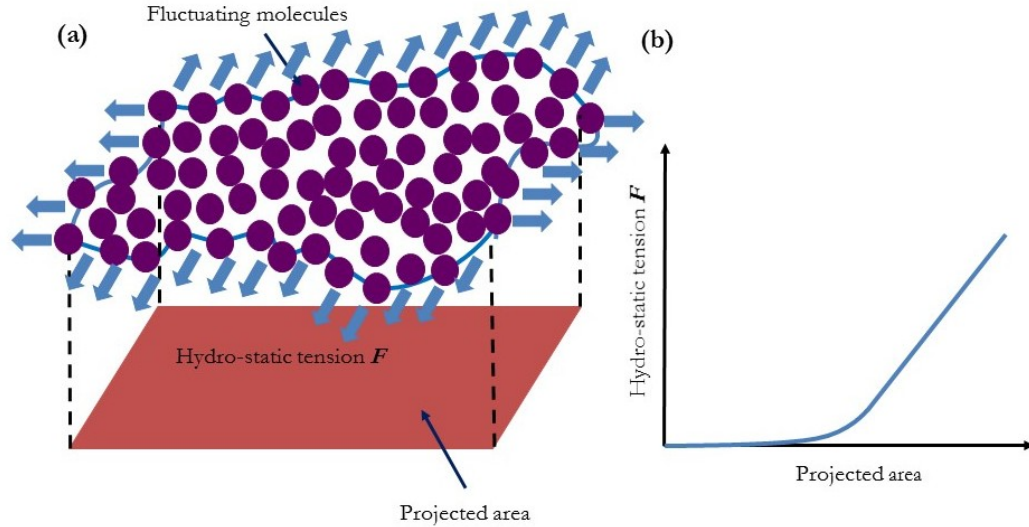
Figure 1.2: (a) A two dimensional system suffering from out-of-plane fluctuations. There is hydro-static tension on the boundary of the system. (b) The projected area increases as hydro-static tension increases.

(1999). As the compressive load is increased to a critical value, filaments in the network start to bend and buckle, and thus the stress-strain curve turns into a plateau. The critical load could be somehow estimated by viewing each filament as an Euler-Bernoulli beamKim et al. (2016). Along the plateau region, the fraction of buckled filaments gradually increases until most of the filaments are buckled. Finally, network densification occurs forming many more inter-filament contacts resulting in steep rise of the stress-strain curve. In this region, the stress dependence on fiber volume fraction is given by a power law relation Van Wyk (1946), Toll (1998). This behavior is typical and has been summarized in Figure 1.3. Often in compressed fiber networks in the plateau region of the stress-strain curve one observes regions of locally densified network coexisting with a rarefied network with straight fibers and few contacts. Our major insight is that these are two phases of the same material with a mobile interface separating them. Thus, compression of fiber networks can be tackled using a continuum theory of phase transitions. We utilize this insight to model compression of fibrin networks (which are one type of ECM with fibrin filaments), CNT foams, as well as blood clots which consist of fibrin networks with embedded platelets and red blood cells.
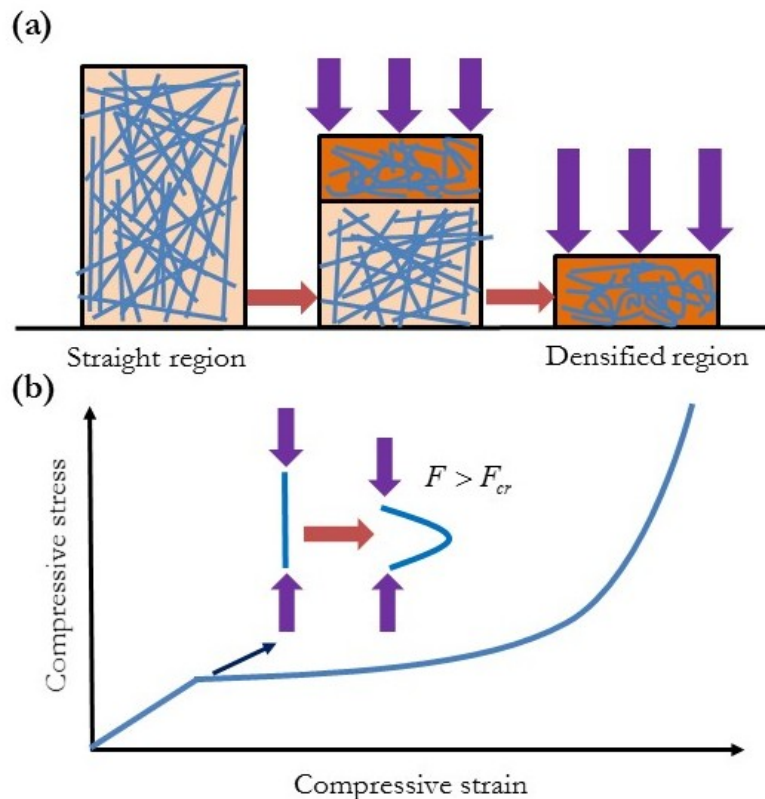
Figure 1.3: (a) Schematic diagram of a foam-like material under compression. The small compression configuration with straight filament is on the left. The large compression configuration with densified network is on the right and a mixture of these two phases for intermediate load in the middle. (b) A typical tri-phasic stressstrain response of such a material assuming quasi-static loading. There is a critical load at the end of the linear region at which filaments start buckling, and the overall curve turns into a plateau region due to increasing fraction of buckled filaments. Finally, there is sharp increase following the plateau due to network densification.

1.1 Scope of the thesis

This thesis is organized as follows. Following the introduction, **Part I** describes a new method combining continuum mechanics and statistical mechanics to understand how thermal fluctuation of two-dimensional materials influences their mechanical behavior. **Chapter 2** applies the method to lipid bilayer membranes. A membrane is viewed as a fluctuating von Karman plate and discretized into triangular elements. Its energy is expressed as a function of nodal displacements, and the partition function and co-variance matrix is computed using Gaussian integrals. Well-known results for the dependence of the projected area of the membrane on the applied tension and recent simulation results on the dependence of

7

membrane free energy on geometry, spontaneous curvature and tension are recovered. As new applications we compute the fluctuations of the membrane of a malaria infected cell and analyze the effects of boundary conditions on fluctuations.

Chapter 3 applies the above method to a solid membrane, graphene. The non-linear coupling of in-plane strains with out-of-plane deflections in solid membranes is captured using a penalty energy. We recover well-known results for the scaling of the fluctuations with membrane size, but show that the fluctuation profile strongly depends on boundary conditions and type of loading applied on the membrane. Our method quantitatively predicts the dependence of the thermal expansion coefficient of graphene on temperature in agreement with several experiments. We also make falsifiable predictions for the dependence of thermal expansion coefficient and the heat capacity of graphene on applied loads and temperature.

Chapter 4 accounts for membrane inclusions such as proteins, bringing us a step closer to realistic cell membranes. The elastic energy of such a system has been well studied Kim et al. (1998), Yolcu et al. (2014); however, the entropic part has not. The embedded proteins in this thesis are modeled as stiff objects which impose a fixed contact angle boundary condition on the membrane producing regions of local curvature. Both elastic contribution and entropic contribution to the free energy of a two-protein and multi-protein system (or cluster) as function of separation distance is computed. An equilibrium spacing between two or more proteins is determined using our computation where the elastic interaction force is balanced by the entropic force. This critical spacing can be modlulated by applying a tension as well as by changing membrane bending modulus. Furthermore, we can compute free energies of a cluster of proteins on a membrane and show how the membrane mechanical properties are affected.

Part II introduces a phase transition theory with specific phase boundary kinetic laws to study the compression behavior of foams. **Chapter 5** applies the theory to a fibrin network. By characterization of the network structure with synchronous measurement of the fibrin storage and loss moduli at increasing degrees of compression, we show that the compressive behavior of fibrin networks is similar to that of cellular solids. A non-linear stress-strain response of fibrin consists of three regimes, same as a foam. Importantly, the spatially non-uniform network deformation includes formation of a moving "compression front" along the axis of strain, which segregated the fibrin network into compartments with different fiber

densities and structure. The Young's modulus of the linear phase depends quadratically on the fibrin volume fraction while that in the densified phase depends cubically on it. The viscoelastic plateau regime corresponds to a mixture of these two phases in which the fractions of the two phases change during compression. We model this regime using a continuum theory of phase transitions and analytically predict the storage and loss moduli which are in good agreement with the experimental data.

Chapter 6 further applies our analysis to platelet poor plasma (PPP) clots, platelet rich plasma (PRP) clots and whole blood clots with a combination of experiment and theory. The experimental analysis is carried out in the lab of Professor John Weisel using a custom built apparatus that combines a rheometer and a confocal microscope. Using this apparatus they can measure the compression stress-strain curve at various strain rates while simultaneously tracking the evolution in clot structure. In addition to the phase transition theory of pure fibrin networks, we also account for the pre-stress caused by platelets, the adhesion of fibrin fibers in the densified phase, the compression of red-blood cells, and the pumping of liquids through the clot during compression.

Chapter 7 applies our phase transition theory to CNT forests, which are well-known as foam-like materials. Our model is inspired by the observation of one or more propagating interfaces across which densified and rarefied phases of the CNT forests co-exist. The same phase transitions model for continua with a stick-slip type kinetic law and a nucleation criterion based on the critical stress for buckling of CNT forests is used to describe the formation and propagation of these interfaces in uniaxial compression experiments. We consider pillars made from bare CNTs, as well as those coated with different thicknesses of alumina using atomic layer deposition (ALD). The effect of ALD coating thickness on the parameters entering the phase transition model are described. We also carry out nanoindentation experiments on the CNT pillars and interpret the load-indentation data by incorporating a constitutive law allowing for phase transitions into solutions for the indentation of a linearly elastic half-space. Even though the state of stress in a nanoindentation experiment is more complex than that in a uniaxial compression test, we find that the parameters obtained from fitting the nanoindentation experiments are close to those from uniaxial compression. Our nanoindentation experiments also reveal dissipation which, we believe, has its origins in inter-fiber contacts in the densified phase. Our models could therefore aid the design of CNT forests to have engineered mechanical properties, and guide further understanding of

their behavior under large deformations.

Chapter 8 concludes the thesis by summarizing and discussing the new results and pointing to future research directions.

Part I

Thermal fluctuation of elastic bodies

Chapter 2

Lipid membranes

Many previous analytic studies of the thermal fluctuation of membranes relied on Fourier series (or series expansions in other orthogonal bases) Fasolino et al. (2007), Helfrich (1973, 1975), Milner & Safran (1987), Boal & Boal (2012) to decompose the membrane fluctuation into normal modes. Then the mean square amplitude of each mode was obtained using the equipartition theorem. Finally, integration over all wave-lengths lead to an expression for the change in projected area of the membrane as a function of the tension. However, these treatments did not examine the role of boundary conditions on membrane fluctuations. For example, I expect smaller fluctuations if I apply clamped-clamped boundary conditions on a fluctuating plate than when I apply simply supported boundary conditions.

Membrane statistical mechanics has also been studied using different simulation methods. In these studies the membrane is first discretized and its energy is written in terms of the discretized variables. Fluctuations are then analyzed using Monte Carlo techniques Auth & Gompper (2013), Ramakrishnan et al. (2010), Tourdot et al. (2014), Lin et al. (2006), Harmandaris & Deserno (2006), Hanlumyuang et al. (2014). Unlike the Fourier series approaches, Monte Carlo methods are not restricted to small fluctuations of membranes. They are general enough to account for the coupling of out-of-plane displacement to in-plane strains Fasolino et al. (2007), Nelson et al. (2004), as well as different types of boundary conditions. Using Monte Carlo simulations the effects of proteins on membranes have also been studied Tourdot et al. (2014), Lin et al. (2006), Ramakrishnan et al. (2014). Another class of simulation methods that has been used to study membrane fluctuations is the time dependent Ginzburg-Landau (TDGL) method. The advantage of these methods

is that they can capture the temporal response of membranes Agrawal & Radhakrishnan (2009), Lin et al. (2006) while Monte Carlo methods give only the equilibrium response. However, it is time consuming to compute membrane free energies using Monte Carlo or TDGL methods. I refer the reader to a review by Ramakrishnan et al. (2014) for a detailed description of the state of the art in simulation methods for membranes.

Here I propose a new approach to compute membrane free energies and fluctuations. I discretize a membrane using equilateral triangle elements Hughes (2000). Then I express the energy of the membrane in terms of displacements of each node exactly as in finite elements, like many Monte Carlo and other simulations do Gompper & Kroll (1996), Nelson et al. (2004). However, I compute the partition function of the membrane using a different strategy based on Gaussian integrals Weiner (2012), D & M. (1980), Zhang & Crothers (2003) that has been successfully applied to fluctuating elastic rodsSu & Purohit (2010, 2011) and fiber networksSu & Purohit (2012), Flory et al. (1969). This has the advantage that it involves lesser computational effort than Monte Carlo or TDGL methods if the size of the membrane is not very large. The disadvantage is that I am confined to fluctuations that are not so large as to cause overhangs in the membrane configuration (this is similar to the Monge gauge Boal & Boal (2012)) resulting in non-quadratic Hamiltonians. Using our method I first recover some known results on membrane fluctuations. Then, I show how different boundary conditions can affect the fluctuations. I also use our method to compute free energies of a membrane with regions of different spontaneous curvature. Our method allows us to study heterogeneous membranes which are the norm in biological cells. I apply it to a recent experiment on the fluctuations of cell membranes infected with malarial parasite Park et al. (2008).

2.1   von Karman energy

Consider a thin square membrane (or plate) of side L with a finite bending modulus K_b everywhere as shown in Figure 2.1. Here I assume that K_b is a constant everywhere, but later in the paper I allow K_b to be a function of reference coordinates x and y. I assume that the plate is under tension, but due to thermal fluctuations it can suffer moderately large deflections. According to the von Karman plate theory, the elastic energy E of such a plate can be expressed as a combination of the stretching and bending energies as in Audoly

13
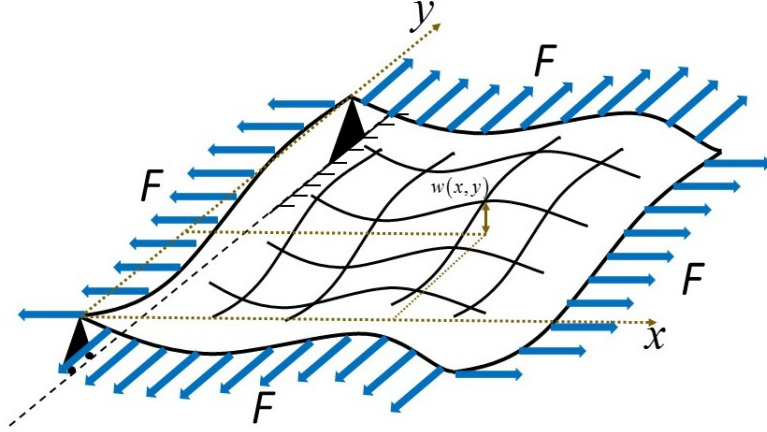
Figure 2.1: Fluctuating elastic plate with applied hydro-static tension F. The out-of-plane deflection of reference point (x, y) is $w(x, y)$.

& Pomeau (2010):

$$E = E_s + E_b = \frac{Yh}{2(1-\nu^2)} \iint \mathrm{d}x\mathrm{d}y \left[(\varepsilon_x + \varepsilon_y)^2 - 2(1-\nu)\left(\varepsilon_x\varepsilon_y - \varepsilon_{xy}^2\right) \right]$$
$$+ \frac{Yh^3}{24(1-\nu^2)} \iint \mathrm{d}x\mathrm{d}y \left[(w_{,xx} + w_{,yy})^2 - 2(1-\nu)\left(w_{,xx}w_{,yy} - w_{,xy}^2\right) \right], \tag{2.1}$$

where Y and ν are the Young's modulus and Poisson ratio of the material respectively, and h is the thickness of the membrane. The variables ε_x, ε_y, ε_{xy}, and w in the integral are respectively the in-plane strains and out-plane displacement of the neutral plane. The sub index $_{,xx},_{,xy},_{,yy}$ represent second derivatives respectively with respect to the reference coordinates. von Karman also deduced the geometrical relation that links the in-plane strains to $w(x, y)$ and the two in-plane displacements u, v respectively in the x and y directions. This relation is summarized by

$$\begin{aligned}
\varepsilon_x &= u_{,x} + \frac{w_{,x}^2}{2}, \\
\varepsilon_y &= v_{,y} + \frac{w_{,y}^2}{2}, \\
\varepsilon_{xy} &= \frac{u_{,y} + v_{,x}}{2} + \frac{w_{,x}w_{,y}}{2}.
\end{aligned} \tag{2.2}$$

The in-plane strains $\varepsilon_x, \varepsilon_y, \varepsilon_{xy}$ are related to the out-of-plane displacement $w(x, y)$ through a compatibility condition which involves the Gauss curvature of the membrane Audoly & Pomeau (2010). Now, consider applying a two-dimensional hydro-static tension of magnitude F along all the edges of our fluctuating membrane, as shown in Figure 2.1. Then from

14

Eqn. (2.2), the potential energy due to this tension is given by

$$PE = -\iint F\,(u_{,x} + v_{,y})\,\mathrm{d}x\mathrm{d}y = -\iint F\left(\varepsilon_x - \frac{w_{,x}^2}{2} + \varepsilon_y - \frac{w_{,y}^2}{2}\right)\mathrm{d}x\mathrm{d}y. \qquad (2.3)$$

Assuming two-dimensional plane stress, let us define $K = Y/(2-2\nu)$ as the two-dimensional bulk modulus. I use K and shear modulus $G = Y/(2 + 2\nu)$ instead of Young's modulus Y and Poisson's ratio ν as the two mechanical parameters for an isotropic material, then

$$\frac{Y}{1 - \nu^2} = \frac{1}{2}\left(\frac{Y}{1 + \nu} + \frac{Y}{1 - \nu}\right) = K + G. \qquad (2.4)$$

Using this I can rewrite the expression for the von-Karman energy as

$$\begin{aligned}
E_s &= \iint \mathrm{d}x\mathrm{d}y \left\{\frac{Kh}{2}(\varepsilon_x + \varepsilon_y)^2 + \frac{Gh}{2}\left[(\varepsilon_x - \varepsilon_y)^2 + \varepsilon_{xy}^2\right]\right\}, \\
E_b &= \iint \mathrm{d}x\mathrm{d}y \left\{\frac{Kh^3}{24}(w_{,xx} + w_{,yy})^2 + \frac{Gh^3}{24}\left[(w_{,xx} - w_{,yy})^2 + w_{,xy}^2\right]\right\}.
\end{aligned} \qquad (2.5)$$

Adding the potential energy to this expression and denoting $Kh^3/12$ as a new bending modulus K_b, I get the total energy of the fluctuating plate as $E = E_s + E_b$, where

$$\begin{aligned}
E_s &= \iint \mathrm{d}x\mathrm{d}y \left\{\frac{Kh}{2}(\varepsilon_x + \varepsilon_y)^2 + \frac{Gh}{2}\left[(\varepsilon_x - \varepsilon_y)^2 + \varepsilon_{xy}^2\right] - F(\varepsilon_x + \varepsilon_y)\right\}, \\
E_b &= \iint \mathrm{d}x\mathrm{d}y \left\{\frac{K_b}{2}(w_{,xx} + w_{,yy})^2 + \frac{Gh^3}{24}\left[(w_{,xx} - w_{,yy})^2 + w_{,xy}^2\right] + \frac{F}{2}(w_{,x}^2 + w_{,y}^2)\right\}.
\end{aligned} \qquad (2.6)$$

We will use this energy to calculate the partition function Z of our plate. But, in order to calculate the partition function I must first discretize our plate and express the energy in terms of the discretized variables.

2.2 Discretization into triangular elements

In this section I specialize to a liquid membrane and show how I discretize it to compute the energy. The in-plane shear modulus G is assumed to be zero. Then the energy

15

expressions reduce to

$$E_s = \iint \mathrm{d}x\mathrm{d}y \left\{ \frac{Kh}{2}(\varepsilon_x + \varepsilon_y)^2 - F(\varepsilon_x + \varepsilon_y) \right\},$$
$$E_b = \iint \mathrm{d}x\mathrm{d}y \left\{ \frac{K_b}{2}(w_{,xx} + w_{,yy})^2 + \frac{F}{2}(w_{,x}^2 + w_{,y}^2) \right\}. \tag{2.7}$$

To further simplify the problem let us assume that our membrane is inextensible, or $\varepsilon_x + \varepsilon_y = 0$ everywhere. Hence, the only terms left in the energy expression are the bending energy and potential energy of the applied tension F caused by out-of-plane displacement of the membrane. For any given ε_x, ε_y and w, I can choose an appropriate ε_{xy} to satisfy the compatibility equation because in-plane shears do not cost any energy for a liquid plate. If the in-plane shear modulus was non-zero then this would not be the case and I would have to impose the compatibility condition as a constraint everywhere on the plate. For the discretized plate this would require computation of the Gauss curvature at every node. This point has been treated in detail in Fasolino et al. (2007), Nelson & Peliti (1987).

We discretize the membrane into $Q \approx \frac{4N^2}{\sqrt{3}}$ equilateral triangles with $P \approx \frac{2N(N+1)}{\sqrt{3}}$ node points, where $N = L/l$, L is the length of the membrane and l is the side of each triangle. The discretization scheme is shown in Figure 2.2a. If the out-of-plane displacements at the nodes are known I assume that the displacements in the interior of the triangular element can be obtained by linear interpolation. Thus, our planar triangle element in the reference configuration goes to a planar triangle in the deformed configuration (see Figure 2.2a). Then I can discretize the total energy into the expression below as discussed in several papers Gompper & Kroll (1996), Abad et al. (1986), Fraternali & Marcelli (2012).

$$E = \frac{K_b}{2} \sum_{(i,j)} A_{ij} \left| \frac{\hat{n}_i - \hat{n}_j}{l_{ij}} \right|^2 + \frac{F}{2} \sum A_e \left(w_{,x}^2 + w_{,y}^2 \right). \tag{2.8}$$

Here, the mean curvature term due to the out-of-plane displacement $w_{,xx} + w_{,yy}$ is expressed in terms of the difference of normal vectors $\hat{n}$ of the two adjacent triangle elements. The summation in the potential energy of the tension F runs over all the triangle elements, and the summation in the bending energy term runs over all the adjacent triangle element pairs that share one edge linked by nodes i, j. l_{ij} is the length between the centers of these two triangle elements. $A_e = L^2/Q$ is the reference area of one triangle element, A_{ij} is the area associated with edge ij, which equals $2A_e/3$ in the reference configuration. l_{ij} and A_{ij} are

16
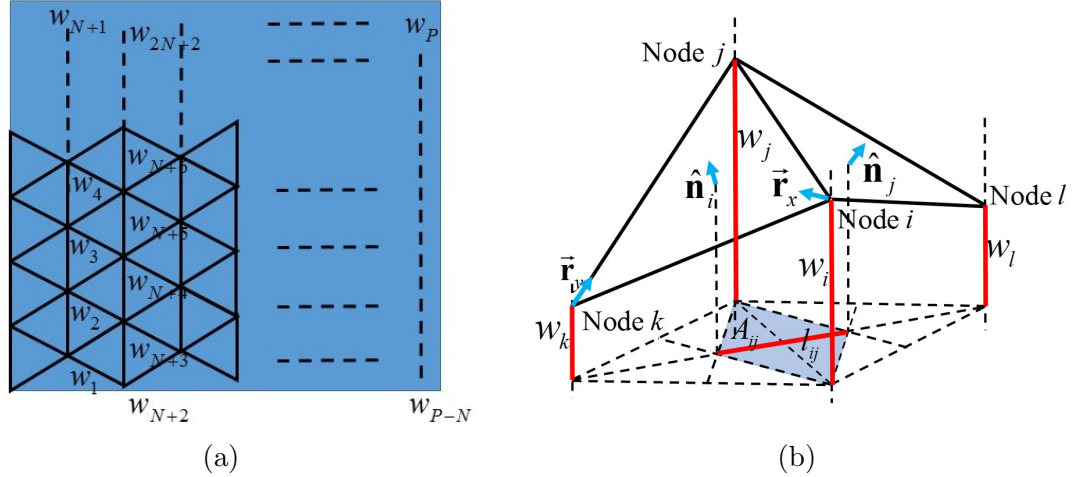
Figure 2.2: (a) Equilateral triangles discretization of a square plate. (b) Reference and deformed configuration of two adjacent elements. The reference configuration is drawn with dashed lines. Each triangular element deforms into a triangle in the deformed configuration.

shown in Figure 2.2b in which nodes i, j, k, l form two elements sharing one edge linked by nodes i, j. $w_{,x}$, $w_{,y}$, and $\hat{n}$ for the element formed by nodes i, j, k are given in terms of the three node displacements w_i, w_j, w_k as

$$
\begin{aligned}
w_{,x} &= \frac{2w_i - w_j - w_k}{\sqrt{3}l}, \ w_{,y} = \frac{w_j - w_k}{l}, \\
\vec{r}_x &= \frac{(0, 1, w_{,x})}{\sqrt{1 + w_{,x}^2}}, \quad \vec{r}_y = \frac{(0, 1, w_{,y})}{\sqrt{1 + w_{,y}^2}}, \\
\hat{n}_i &= \vec{r}_x \times \vec{r}_y = \frac{(-w_{,x}, -w_{,y}, 1)}{\sqrt{1 + w_{,x}^2 + w_{,y}^2 + w_{,x}^2 w_{,y}^2}}.
\end{aligned}
\tag{2.9}
$$

Similarly $w_{,x}$, $w_{,y}$, and $\hat{n}$ for the element formed by nodes i, j, l are given in terms of the three node displacements w_i, w_j, w_l. $w_{,x}^2$ and $w_{,y}^2$ are assumed small enough that the denominator in the expression for $\hat{n}_i$ can be expanded in a Taylor series. However, if we retain terms only upto quadratic order in $w(x, y)$ in the energy then $w_{,x}^2$ and $w_{,y}^2$ from the denominators do not contribute. Substituting the result into Eqn. (2.8) I get the energy expression as a quadratic function of the nodal displacements for the two elements shown in Figure 2.2b as

$$
E = \frac{4 K_b A_e}{3 l^4}(w_i + w_j - w_k - w_l)^2 + \frac{F A_e}{3 l^2}\left[(w_i - w_j)^2 + (w_j - w_k)^2 + (w_k - w_i)^2\right]. \tag{2.10}
$$

We can repeat this exercise for all the elements and get the energy as a quadratic function

of $\{w_t\}$, $t = 1, 2, ..., P$, where P is the number of nodes, viz., $E = \mathbf{w}\mathbf{M}\mathbf{w}^{\mathrm{T}}$, where the vector $\mathbf{w} = [w_1, w_2, ..., w_P]$. The matrix $\mathbf{M}$ is the stiffness matrix and it is a function of K_b, F, L, l. The probability of finding the membrane in any given configuration is proportional to $\exp(-E/k_B T)$, where E is the energy of this configuration, k_B is the Boltzmann constant and T is the absolute temperature. The partition function Z of the membrane is obtained by integration of $\exp(-E/k_B T)$ over all possible configurations. To carry out this integration efficiently, I first recognize that at zero temperature (absence of fluctuations) the lowest energy configuration of our membrane is flat, $w(x, y) = 0$ for all x, y. When $T > 0$ the membrane fluctuates around this flat configuration. Second, I recognize that configurations with large deviations from this flat shape are energetically costly and will make exponentially small contributions to the partition function. This allows us to change the limits of the integrals over dw_j, $j = 1, 2, ..., P$ to $\pm\infty$. Then, the integration over all configurations for the partition function becomes easy to carry out as given in Zhang & Crothers (2003), Su & Purohit (2010, 2011, 2012). The partition function of the membrane scales with square root of the determinant of matrix $\mathbf{M}$, or the square root of the product of all eigenvalues of $\mathbf{M}$ as

$$Z = \sqrt{\frac{(2\pi k_B T)^P}{\det \mathbf{M}}}. \tag{2.11}$$

2.3   Thermodynamics of the membrane

The Gibbs free energy $G(F, T)$ of the membrane is related to the partition function Z as $G = -k_B T \ln Z$. This quantity can also be computed using Monte Carlo and TDGL methods Agrawal & Radhakrishnan (2009) for a triangulated membrane whose energy was written as a quadratic form above with the stiffness matrix $\mathbf{M}$. The computational effort involved in calculating these free energies using Monte Carlo or TDGL simulation methods depends on the acceptable error tolerance. The smaller the error tolerance, the more Monte Carlo moves are required. In our method the error in computation of the free energy arises from the numerical computation of the determinant of $\mathbf{M}$. If the size of the matrix is not very large then the error in the computation of the determinant is limited only by machine accuracy. Of course, discretizing a membrane also leads to errors in computation of the thermodynamic properties. I quantify this error in the following. I also show a comparison of the free energy computed using our method to that obtained by the TDGL method in

18
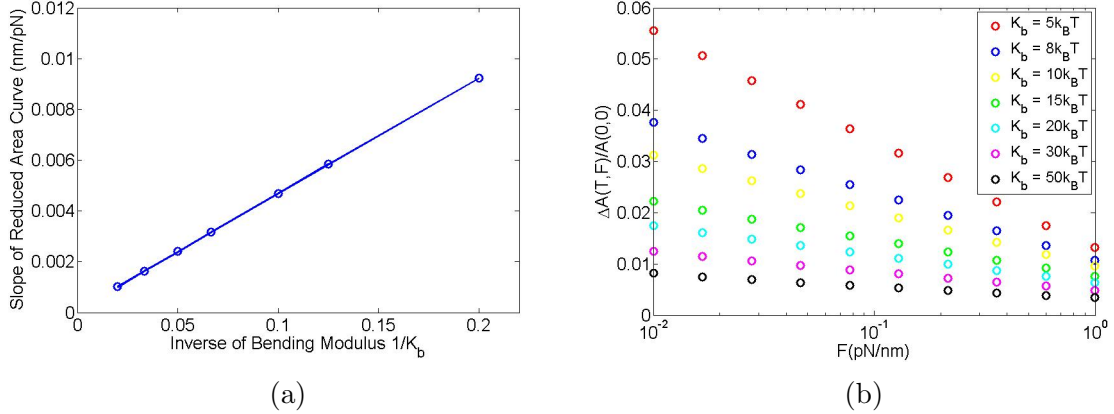
Figure 2.3: (a) Reduced area varies linearly as a function of $\log F$ for different values of bending modulus K_b. (b) Slopes of curves in (a) vary linearly with the inverse of bending modulus K_b.

Section 2.6.

We can compute the properties of the membrane by computing derivatives of the free energy. First, the reduction in projected area caused by thermal fluctuation is defined as $\Delta A = A(\infty, T) - A(F, T)$, where $A(\infty, T)$ is the membrane area at very large tension such that all the undulations are stretched out and it is flat. The area reduction is conjugate to the tension F in the free energy of the membrane, and can be computed as $\Delta A = -\partial G / \partial F$. Since all the terms related to the force F in the expression for the partition function Z are included in the matrix $\mathbf{M}$, I have

$$\Delta A = -\frac{k_B T}{2} \frac{\mathrm{d}}{\mathrm{d}F} \ln\left(\det \mathbf{M}\right). \tag{2.12}$$

Second, the entropy is given by

$$S = -\frac{\partial G}{\partial T} = \frac{k_B}{2} \left[P \ln(2\pi k_B T) - \det \mathbf{M} + 1 \right]. \tag{2.13}$$

We want to compare the results from these expressions with those expected from the Helfrich theory. In a typical membrane fluctuation problem in biology the size of the membrane is in microns, bending modulus of the membrane is around $10k_B T$ and the typical tension range is from $0.01\mathrm{pN/nm}$ to $1\mathrm{pN/nm}$. So, for our computation, I consider a square patch of membrane of side $L = 1\mu\mathrm{m}$. Let us first examine the dependence of the reduced area $\Delta A / A$ obtained from our computations on the bending modulus K_b. Here $A = L^2$ is

19

the reference area of the membrane at zero temperature. I compute the derivatives in Eqn. (2.12) for distinct values of membrane bending modulus and plot the results in Figure 2.3a. The slope of the curves (in the $\Delta A / A$ versus $\log F$ plot) varies linearly with the inverse of bending modulus $1/K_b$ as shown in Figure 2.3b. This is consistent with the analytic solution given in Helfrich (1975), Milner & Safran (1987), Boal & Boal (2012) and reproduced below:

$$\frac{\Delta A}{A} = \frac{k_B T}{8 \pi K_b} \ln \frac{\pi^2 / b^2 + F / K_b}{\pi^2 / A + F / K_b}, \tag{2.14}$$

where b is the radius of a lipid head group and is on the order of 1 nm. To compute the entropy of the membrane recall the Maxwell relation linking the projected area and the entropy:

$$\left(\frac{\partial S}{\partial F} \right)_T = - \left(\frac{\partial \Delta A}{\partial T} \right)_F. \tag{2.15}$$

The right hand side of the above equation can be computed from (2.14). Then, by integration I get

$$\begin{aligned}
S(F, T) &= \int - \left(\frac{\partial \Delta A}{\partial T} \right)_F \mathrm{d}F \\
&= \frac{A k_B}{8 \pi} \left(\frac{\pi^2}{A} + \frac{F}{K_b} \right) \ln \left(\frac{\pi^2}{A} + \frac{F}{K_b} \right) - \frac{A k_B}{8 \pi} \left(\frac{\pi^2}{b^2} + \frac{F}{K_b} \right) \ln \left(\frac{\pi^2}{b^2} + \frac{F}{K_b} \right) + S_0(T),
\end{aligned} \tag{2.16}$$

where $S_0(T)$ is some function of temperature T and independent of membrane tension F.

In order to compare the results of our discretized model with this equation I change N to see how small our elements should be in order for our curves to coincide with the analytic solution. I go as far as $N = 400$ due to limitations of computational power. Note that the side of one equilateral triangle element at $N = 400$ is about 2.5 nm since the side of our square membrane is 1 μm. This means that each element contains only about 10 lipids when $N = 400$. The results of our computation are plotted in Figure 2.4a and 2.4b, respectively for reduced area $\Delta A / A$ and entropy change ΔS. I see that our semi-analytic method approaches Eqns. (2.14) and (2.16) as N increases. I can define an error by computing the distance between the analytic solution and the curve from our numerical computation for both the reduced area and the entropy. The error at tension $F = 0.01$ pN/nm decreases linearly with the logarithm of the number of elements (i.e. it decreases slowly) as shown in Figure. 2.5.
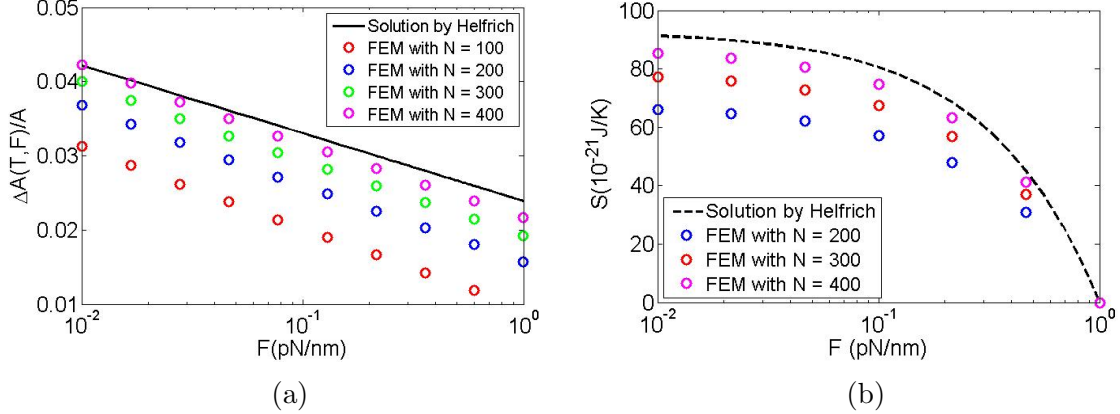
Figure 2.4: (a) Thermally reduced area computed with increasing number of elements with $K_b = 10k_BT$ at $T = 300$K. (b) Entropy change $\Delta S = S - S_0$ computed with increasing number of elements N. Notice that our numerical calculation based on (2.11) approaches the analytic solution of Helfrich as N increases.

2.4 Analysis of variance and effect of boundary conditions

One important result which follows from the calculation of the partition function is the co-variance matrix $\langle w_i w_j \rangle$ Zhang & Crothers (2003), Su & Purohit (2010, 2011, 2012), which can be calculated from the inverse of the stiffness matrix $\mathbf{M}$ as

$$\langle w_i w_j \rangle = \frac{k_B T}{[\mathbf{M}^{-1}]_{ij}}. \tag{2.17}$$

From this I can get the variance of the out-plane deflection $\langle w_i^2 \rangle$ as a function of reference position on our membrane. I have done this in Figure 2.6 for two different boundary conditions. Due to limitations computational power, I turn to a smaller 0.5μm $\times 0.5\mu$m membrane in order to keep the triangle element size $l = 2.5$ nm as in the previous computation of reduced area. In the first case one edge of the membrane is simply supported with the three other edges being free, while in the second case two opposite edges of the membrane are simply supported with the other two being free. The distance between the simply supported edges is allowed to change. In both cases a hydro-static tension F per unit length is applied on the edges. In the first case the fluctuation increases as I go nearer the free boundaries, while in the second the fluctuation is maximum near the center of the membrane. In both cases the height fluctuation is on the order of several nm for given

21
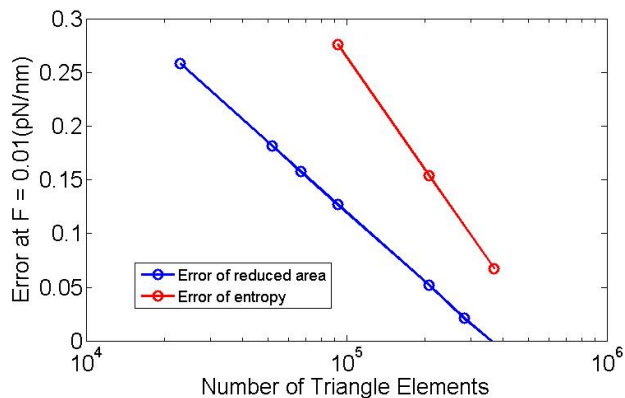
Figure 2.5: The error of our computational result, both for reduced area and entropy change, with respect to the Helfrich solution at $F = 0.01$pN/nm decreases linearly with the logarithm of the number of elements.
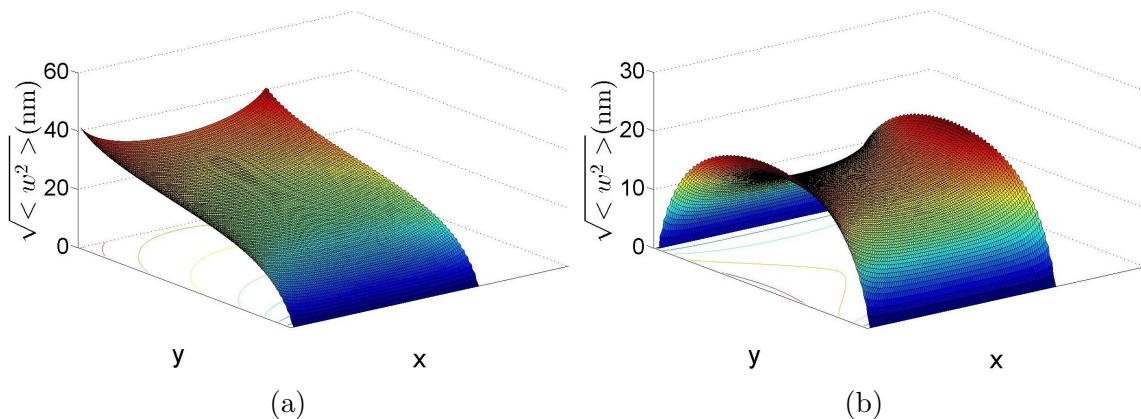
Figure 2.6: (a) Standard deviation in w of a one end hinged membrane with tension $F = 0.01$ pN/nm. (b) Standard deviation in w of a two end hinged membrane with tension $F = 0.01$ pN/nm. The magnitude of the fluctuation depends on the boundary conditions.

membrane properties and tension $F = 0.01$ pN/nm. Most studies of membrane fluctuation do not account for the boundary conditions as we have done here. This could have implications on the interpretations of experiments which extract membrane properties by measuring thermal fluctuations.

2.5 Persistence length

Fluctuating polymers are often characterized by their persistence length ξ_p Boal & Boal (2012). This concept has been extended also to membranes. Roughly speaking, the

persistence length is a length scale at which the thermal energy is comparable to the energy stored in elastic deformations. In other words, if the size of the elements is much larger than the persistence length the approximation of smooth deformations will be violated because shape fluctuations caused by thermal motion will obliterate the smoothness. Persistence lengths of lipid membranes are known to be much longer than the molecular scale Boal & Boal (2012). One arrives at this conclusion by defining the persistence length ξ_p through the decay in correlation of normal vectors of the membrane as

$$\langle \mathbf{n}(0) \cdot \mathbf{n}(\Delta \mathbf{r}) \rangle = \exp\left(-\frac{\Delta r}{\xi_p}\right), \tag{2.18}$$

where Δr is a distance coordinate. According to the derivation in Boal & Boal (2012), the correlation function can be reduced to

$$\langle \mathbf{n}(0) \cdot \mathbf{n}(\Delta \mathbf{r}) \rangle = 1 - \frac{k_B T}{2\pi} \int \frac{I_\theta(z)\, q \mathrm{d}q}{F + K_b q^2}, \tag{2.19}$$

where $z = q|\Delta \mathbf{r}|$ and

$$I_\theta(z) = 1 - \frac{\int_0^{2\pi} \mathrm{d}\theta \cos(z \cos\theta)}{2\pi} \tag{2.20}$$

is a Bessel function. At large z the second term on the right hand side of the above equation is very close to 0, so it is ignored in Eqn. (2.19). Hence, with q ranging approximately from $\pi/\Delta r$ to π/b, where b is the size of lipid head group, Eqn. (2.19) becomes:

$$\langle \mathbf{n}(0) \cdot \mathbf{n}(\Delta \mathbf{r}) \rangle \sim 1 - \frac{k_B T}{4\pi K_b} \ln\left(F + K_b q^2\right)\big|_{\pi/\Delta r}^{\pi/b} \sim 1 - \frac{k_B T}{4\pi K_b} \ln \frac{F + K_b \pi^2/b^2}{F + K_b \pi^2/\Delta r^2}. \tag{2.21}$$

If I set membrane tension F to zero, Eqn. (2.21) becomes the expression in Boal & Boal (2012):

$$\langle \mathbf{n}(0) \cdot \mathbf{n}(\Delta \mathbf{r}) \rangle \sim 1 - \frac{k_B T}{2\pi K_b} \ln \frac{\Delta r}{b}. \tag{2.22}$$

By comparing this expression with a linearized version of Eqn. (2.18) one concludes that the persistence length of a membrane is very long Boal & Boal (2012). On the other hand, according to the expression for the normal vector $\mathbf{n}$ given in Eqn. (2.9) the quantity $\langle \mathbf{n}(0) \cdot \mathbf{n}(\Delta \mathbf{r}) \rangle$ can be related to the covariance matrix given in Eqn. (2.17). Suppose I want to compute the correlation of normal vector between two equilateral triangle elements whose nodal displacements are denoted by w_a, w_b, w_c and w_d, w_e, w_f respectively according

23
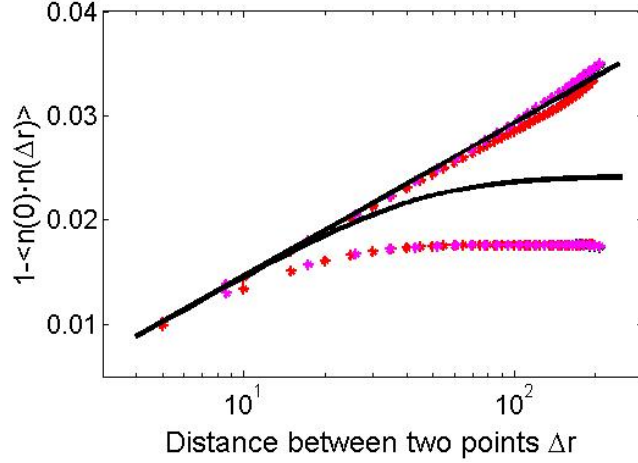
Figure 2.7: Change of correlation of normal vectors as functions of distance. I plot $1 - \langle \mathbf{n}(0) \cdot \mathbf{n}(\Delta \mathbf{r}) \rangle$ against the distance Δr. The straight black line is from Eqn. (2.21), and the curved black line is from Eqn. (2.22) for 0.1 pN/nm tension. Blue, red, yellow, magenta lines are obtained from our computations and represent four distinct directions from the center of the membrane.

to Eqn. (2.9), then

$$
\mathbf{n}(0) = \left(-\frac{2w_b - w_a - w_c}{\sqrt{3}l}, -\frac{w_c - w_a}{l}, 1 \right), \quad \mathbf{n}(\Delta \mathbf{r}) = \left(-\frac{2w_e - w_d - w_f}{\sqrt{3}l}, -\frac{w_f - w_d}{l}, 1 \right).
$$
(2.23)

From this I see that the average quantity $\langle \mathbf{n}(0) \cdot \mathbf{n}(\Delta \mathbf{r}) \rangle$ is a sum of several entries in

the covariance matrix $\langle w_i w_j \rangle$ of Eqn. (2.9). Hence, I am in a position to compare the

correlation of the normal vectors from our computations with Eqn. (2.22). This exercise is

performed in Figure 2.7. I choose the center of membrane as the origin where $\mathbf{r} = \mathbf{0}$ and

extend $\Delta \mathbf{r}$ towards four directions on the plane. The four different color points represent

computational results for the four directions. The result from our discretized model matches

the theoretical prediction Eqn. (2.22) very well in Figure 2.7 for $F = 0$. Our method

also captures the trend in the correlation expected from Eqn. (2.21) for finite tension

$F = 0.1$ pN/nm. The disagreement at large values of Δr is due to (a) approximations

in the derivation of Eqn. (2.21), (b) from the fact that the analytic expression does not

account for boundary conditions as I do in our computation, and (c) ours is a discretized

model. While this reinforces our computational method, it also shows that Eqn. (2.18) is

not how the correlations of the normal decay on a membrane.

24

2.6 Comparison to TDGL simulation
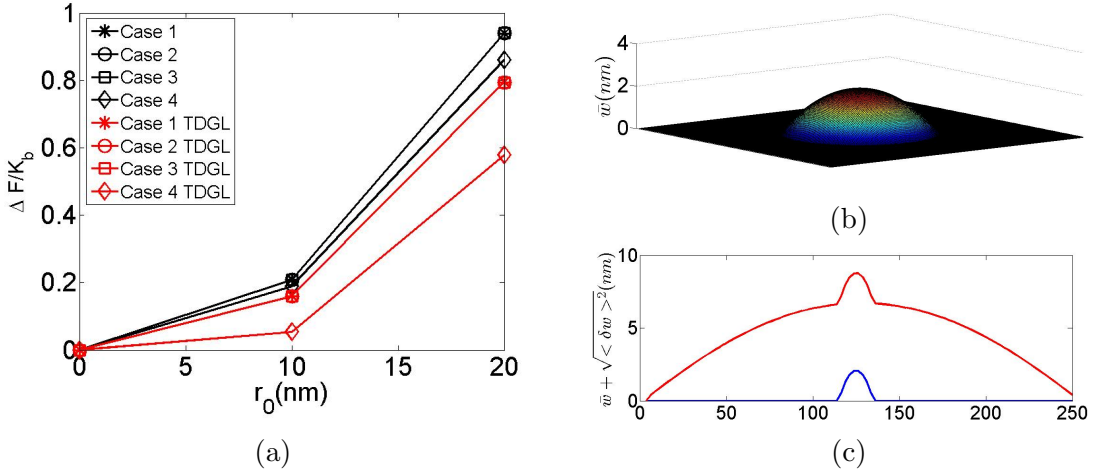
Figure 2.8: (a) Comparison of membrane free energy change as a function of r_0. Black markers are our result. Red marks are TGDL simulation data extracted from Figure 4 in Agrawal & Radhakrishnan (2009). (b) Three dimensional plot of equilibrium position $\bar{w}$ of a membrane with a region of non-zero spontaneous curvature $C_0 = 0.04$ nm^{-1}, $r_0 = 10$ nm, and zero-tension. I have just chosen the mid 40 nm×40 nm region to show for clarity. (c) Cross-sectional plot of a thermally fluctuating membrane with a region of non-zero spontaneous curvature in the middle of the square patch. Blue line is the equilibrium position. I have added the standard deviation $\sqrt{\langle \delta w^2 \rangle}$ to the equilibrium position and plotted it as the red line.

An advantage of our method is that I can compute membrane free energies with modest computational effort. Here I compare our calculations with a TDGL simulation presented in Agrawal & Radhakrishnan (2009). In their calculation, a square patch of membrane is considered with non-zero spontaneous curvature C_0 in a circular region of radius r_0 in the center of the square. Their membrane is discretized by a 50-by-50 grid, and membrane free energy and entropy are obtained as a function of r_0 for different membrane sizes, bending modulus and tension. I will show that our model can be modified to account for spontaneous curvature and correctly obtain these quantities. To this end I add C_0 into Eqn. (2.8) for the energy as follows:

$$E = \frac{K_b}{2} \sum_{(i,j)} A_{ij} \left(\left| \frac{\hat{n}_i - \hat{n}_j}{l_{ij}} \right| - C_0 \right)^2 + \frac{F}{2} \sum A_e \left(w_{,x}^2 + w_{,y}^2 \right). \tag{2.24}$$

Note that C_0 can be a function of position on the membrane. Now I follow the same

procedure as I did for reaching Eqn. (2.10) and find that the energy takes the following form:

$$E = \mathbf{w}\mathbf{M}\mathbf{w}^{\mathrm{T}} + \mathbf{w} \cdot \mathbf{b} + c, \tag{2.25}$$

where $\mathbf{b}$ is a vector that accounts for the non-zero spontaneous curvature associated with some node displacements w_i, and c is a constant. Now, I differentiate Eqn. (2.25) with respect to w_i, $i = 1, 2, ..., P$ and set it to zero to get the equilibrium position $\bar{w}$ of the nodes as:

$$\bar{\mathbf{w}} = -\frac{1}{2}\mathbf{M}^{-1}\mathbf{b}. \tag{2.26}$$

Let $\mathbf{w} = \bar{\mathbf{w}} + \delta\mathbf{w}$, where the new variable $\delta\mathbf{w}$ is a fluctuation around the equilibrium position. Therefore Eqn. (2.25) can be rewritten as:

$$E = (\bar{\mathbf{w}} + \delta\mathbf{w})\mathbf{M}(\bar{\mathbf{w}} + \delta\mathbf{w})^{\mathrm{T}} + (\bar{\mathbf{w}} + \delta\mathbf{w}) \cdot \mathbf{b} + c = \delta\mathbf{w}\mathbf{M}\delta\mathbf{w}^{\mathrm{T}} + \bar{c}, \tag{2.27}$$

where $\bar{c} = c + \frac{1}{2}\bar{\mathbf{w}} \cdot \mathbf{b}$ is independent of δw. Then, after factoring out $\bar{c}$ from the integration for the partition function, I get Zhang & Crothers (2003), Su & Purohit (2010, 2011, 2012):

$$Z = \exp\left(-\frac{\bar{c}}{k_B T}\right) \sqrt{\frac{(2\pi k_B T)^P}{\det \mathbf{M}}}. \tag{2.28}$$

To compare our computation with the TGDL simulation, I compute membrane free energy with exactly the same membrane properties and applied tension as in Agrawal & Radhakrishnan (2009). The side of the square patch is 250 nm. r_0 is varied between 0 and 20 nm, while C_0 is chosen to be 0.04 nm^{-1}. The membrane is simply supported on four sides, and I use $N = 300$. The CPU time for the computation of one curve in Figure 2.8a is less than 20 hours on a PC with a Intel(R) Core(TM) i7-3770 CPU @ 3.40 GHz processor. Our result agrees with free energies obtained from the TDGL simulation as shown in Figure 2.8a. I also show a contour plot of equilibrium position as computed using Eqn. (2.26) in Figure 2.8b for zero tension. Our analysis shows that the spontaneous curvature does not affect the stiffness matrix $\mathbf{M}$. Hence, the variance of the fluctuations given in Eqn. (2.17) is a function only of matrix $\mathbf{M}$ and is independent of the spontaneous curvature. The standard deviation of the fluctuations as a function of position can be seen in Figure 2.8c in which a cross-section of the membrane in equilibrium is depicted. Note also that spontaneous

26

curvature does not change the entropy expression given in Eqn. (2.13). Therefore, in our calculation, change of magnitude or location of non-zero spontaneous curvature does not affect the entropy. This is also the case for the TDGL simulation in which every curve for entropy change (Figure 6 in Agrawal & Radhakrishnan (2009) is flat and near zero compared to the curve for free energy change due to different sizes of the non-zero spontaneous curvature region.

2.7   Heterogeneous membrane

So far I have assumed that our membrane has the same bending modulus everywhere. I have reproduced some well known results on membrane fluctuations and have extended some other results, e.g. influence of boundary conditions on the magnitude of fluctuations. However, our computational method is capable of handling heterogeneous membranes in which the bending modulus and spontaneous curvature depend on position. This is the case for every cell membrane and can be produced in vesicles in which phase separation results in regions with different lipid compositions Baumgart et al. (2003). In order to demonstrate the capabilities of our method I will use it to extract some information from experimental data on the membranes of red blood cells infected with malarial parasites Park et al. (2008). These experiments show that the fluctuations of the membrane are significantly influenced by localized membrane stiffening caused by the parasite. To model this situation I choose a square patch of membrane of side 250 nm. The middle portion of this membrane of side 50 nm has a different bending modulus $K_{b2} = 100k_BT$, while elsewhere $K_{b1} = 10k_BT$. I compute the variance of the fluctuations in w that are typically measured in experiments. Our goal is to extract a membrane tension by comparing our results with the experiment. The membrane is simply supporte on four sides and I apply a constant force per unit length on all edges. The results from this heterogeneous membrane model are shown in Figure 2.9. To match the experiments I had to use a membrane tension as 0.3 pN/nm, which is less than the lytic tension of the membrane. In Figure 2.9a the computational result correctly estimates the magnitude of the fluctuations measured in Park et al. (2008). In this figure red represents large fluctuations and blue corresponds to small fluctuations. The overall profile in Figure 2.9b is different from a homogeneous membrane in section 2.4, where the fluctuation at the center point is larger than points
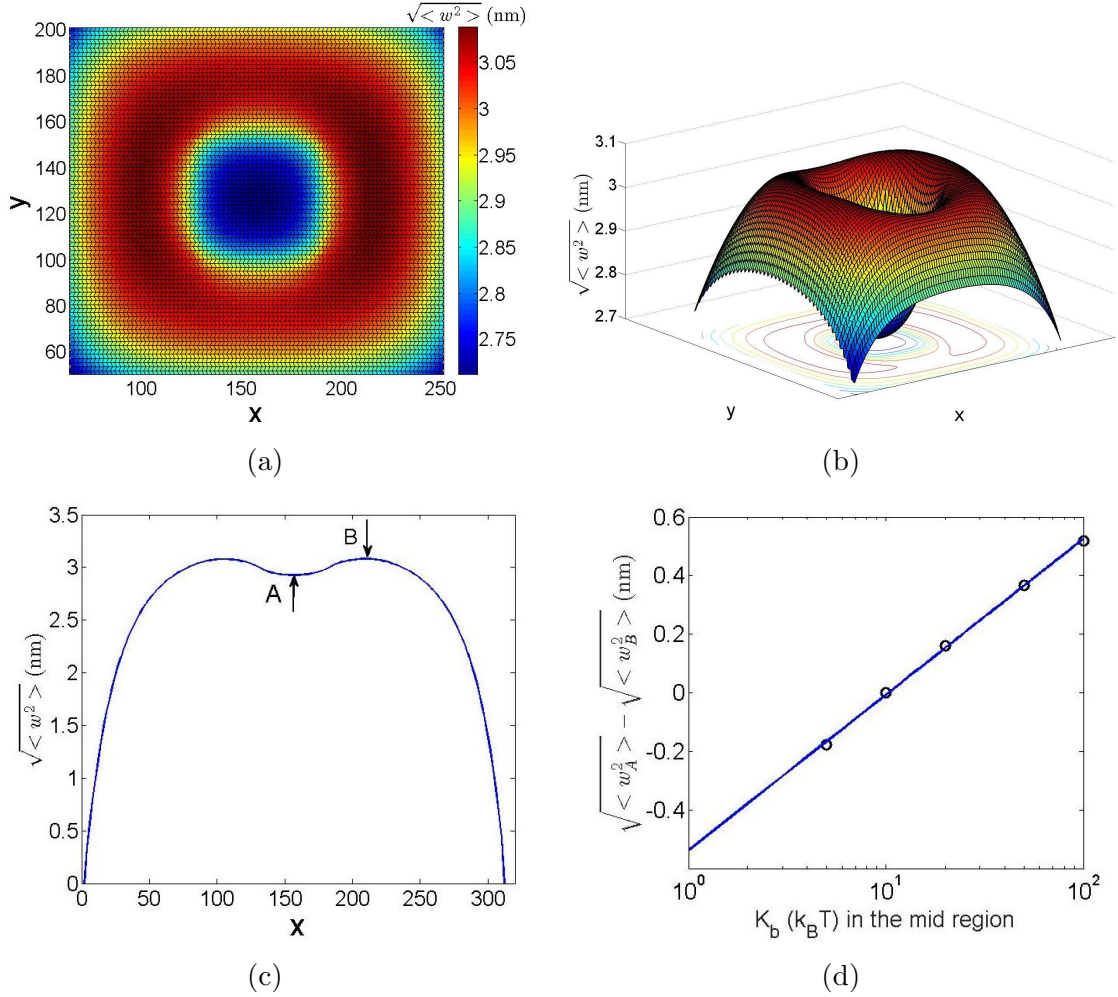
Figure 2.9: (a) Two dimensional contour plot of standard deviation in $w(x, y)$ of a heterogeneous membrane. (b) Three dimensional plot of standard deviation of the same heterogeneous membrane. (c) Cross-sectional profile of standard deviation. A and B are respectively the middle and margin of the concave region in the center. (d) Difference between the middle and the margin of the concave region versus membrane mid-region bending modulus. The bending modulus outside the mid-region of the membrane is $10k_BT$ at $T = 300$K. The tension $F = 0.3$pN/nm for these plots.

near the boundary. In this heterogeneous membrane, due to large bending modulus that suppresses thermal fluctuation, the variance in the middle region is smaller. To see this effect clearly, one cross-sectional profile of the membrane variance is shown in Figure 2.9c. I measure the difference between the middle and the margin of the concave region marked as A and B, respectively, and plot it as a function of membrane mid-region bending modulus as shown in Figure 2.9d. If the membrane tension is known then this kind of plot can be used to infer the difference in bending modulus between the stiffer and softer regions.

Chapter 3

Graphene fluctuations

In this Chapter the goal is to extend our semi-analytic method based on Gaussian integrals to solid membranes, or fluctuating elastic plates. The main difficulty in doing so is that the out-of-plane deflections of a solid membrane are coupled with the in-plane strains through the compatibility condition in von-Karman plate theory Audoly & Pomeau (2010). Earlier simulation work on triangulated surface models as well as analytic theory has shown that undulations with non-zero Gauss curvature are suppressed because of this constraint Nelson & Peliti (1987), Abraham & Nelson (1990), Fasolino et al. (2007), Le Doussal & Radzihovsky (1992), Abraham & Nelson (1990). In a similar vein, I show that a membrane explores fewer configurations if I enforce the compatibility constraint on our discretized plate through a penalty energy. The coupling between out-of-plane and in-plane displacement in solid membranes has also been analyzed in Fourier space using perturbation theory to get the anharmonic part of the spectrum Košmrlj & Nelson (2014), Paulose et al. (2012), Fasolino et al. (2007). To the best of our knowledge, none of these methods explore the effect of boundary conditions on the fluctuations. For example, analogous to filaments Purohit et al. (2008), Su & Purohit (2012), I expect that a plate clamped on all its edges will suffer smaller fluctuations than one that is simply supported on all its edges. Our method allows us to explore these possibilities and consider fluctuations in the presence of shear loads. Note that that the liquid membranes I studied before could not support shears. Also, our method can handle different membrane geometries. For example, in Liang & Purohit (2016a) I considered a square membrane with a circular patch in the middle that had a non-zero spontaneous curvature. Due to the non-zero spontaneous curvature this patch assumed

the shape of a spherical cap under zero loads. We analyzed the thermal fluctuations of this membrane and showed that our results were in agreement with earlier simulations using very different methods Agrawal & Radhakrishnan (2009). In these calculations I did not need to enforce the compatibility constraint since the membrane was liquid in-plane. To analyze the flcutuations of curved plates (or shells) using our method it will be necessary to account for the compatibility constraint in curvilinear coordinates. While this is beyond the scope of our paper, progress has been made in the study of thermal fluctuations of shells Paulose et al. (2012) by triangulating them in a similar fashion as I do here.

As an illustration of the capability of our methods I focus attention on the thermal fluctuations of graphene. The outstanding thermal, mechanical and electrical properties of graphene Bunch et al. (2007), Lee et al. (2008) have received a lot of attention in the past decade, but its thermal fluctuations have received relatively less attention Fasolino et al. (2007). It is appreciated, however, that ripples on graphene have some bearing on its physical properties Fasolino et al. (2007), Los et al. (2009), Zakharchenko et al. (2010), Garcia-Sanchez et al. (2008), He et al. (2011). One such effect is its negative thermal expansion coefficient which has been studied through experiment and simulation Yoon et al. (2011), Bao et al. (2009), Pan et al. (2012). Here I quantitatively explain the dependence of the thermal expansion coefficient on temperature using our semi-analytic method. I also make predictions for the dependence of thermal expansion coefficient on loading (hydrostatic and shear) and temperature.

3.1   von Karman energy

As Presented in previous chapter, Eqns. (2.1) and (2.3) together give the energy of a configuration of the plate which is determined by $\varepsilon_x(x,y)$, $\varepsilon_y(x,y)$, $\varepsilon_{xy}(x,y)$ and $w(x,y)$, subject to the compatibility constraint:

$$\varepsilon_{x,yy} + \varepsilon_{y,xx} - 2\varepsilon_{xy,xy} = w_{,xy}^2 - w_{,xx}w_{,yy}. \qquad (3.1)$$

It is instructive to make some estimates about the effect of fluctuations before I proceed further. From Eqn. (2.1) I see that $E_s \sim YA\varepsilon^2/2$ where ε represents in-plane strains and $E_b \sim K_bA\kappa^2/2$, where κ represents a curvature. Using the equipartition theorem of

statistical mechanics I can estimate the mean-square fluctuations in these quantities as $\langle \varepsilon^2 \rangle = \frac{k_B T}{YA}$ and $\langle \kappa^2 \rangle = \frac{k_B T}{K_b A}$. If h is the thickness of our plate then the ratio of mean-square fluctuations in the bending strain to in-plane strain is $\frac{\langle \varepsilon^2 \rangle}{\langle \kappa^2 \rangle h^2} = \frac{K_b}{Y h^2}$. For a graphene sheet $Y \approx 1$ TPa$\times 0.3$ nm, $K_b \approx 10^{-19}$ Nm and $h \approx 0.3$ nm Lee et al. (2008), so that $\frac{K_b}{Y h^2} \approx 10^{-3}$, and thus in-plane strain fluctuations can be neglected in comparison to out-of-plane bending fluctuations. Due to the very high in-plane stretching modulus I can also neglect the term $F(\varepsilon_x + \varepsilon_y)$ in Eqn. (2.3) above. In the end, I assume that the plate has constant in-plane strains (no fluctuation) due to hydrostatic tension F which contributes a constant term C to the expression for energy below:

$$
\begin{aligned}
E = E_b + E_f + C = \iint \mathrm{d}x\mathrm{d}y &\left[\frac{K_b}{2}(w_{,xx} + w_{,yy})^2 \right. \\
&\left. + K_G \left(w_{,xx}w_{,yy} - w_{,xy}^2 \right) + F \left(\frac{w_{,x}^2}{2} + \frac{w_{,y}^2}{2} \right) \right] + C.
\end{aligned}
\tag{3.2}
$$

We will use this energy expression to compute the fluctuations of our membrane, remembering that C will have no effect on the fluctuations. To do so, I must calculate the partition function.

3.2 Enforcing the compatibility constraint

In order to extend this technique to solid plates I must carry out the partition sum only over those configurations that satisfy the compatibility equation Eqn. (3.1). This equation constrains the displacements at every point on the plate. Now, the question is how do I enforce this constraint everywhere on the plate. Recall that I discretize our plate into equilateral triangle elements in the reference or undeformed configuration. When the plate is deformed the elements remain triangular and flat with straight edges. Hence, all the displacements u, v and w are linear functions of the reference coordinates and the compatibility equation is trivially satisfied inside every triangular element. However, at each node the strains vary discontinuously and the Gaussian curvature is non-zero. Hence, in order to enforce the compatibility constraint at each node I will penalize a violation of Eqn. (3.1) by a large energy cost. For convenience, I define a compatibility function:

$$
f_c = \varepsilon_{x,yy} + \varepsilon_{y,xx} - 2\varepsilon_{xy,xy} - w_{,xy}^2 + w_{,xx}w_{,yy}
\tag{3.3}
$$

31
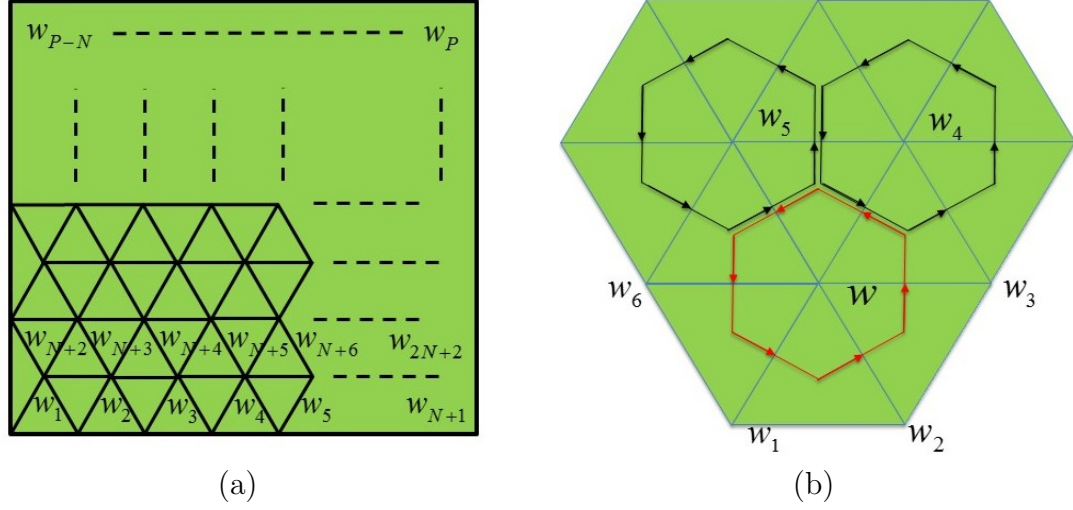
Figure 3.1: (a) Equilateral triangle discretization scheme of a square plate as in Liang & Purohit (2016a). (b) For computing the energy cost of violating the compatibility constraint Eqn. (3.1) I show in red the contour around a node whose out-of-plane displacement is w. Out-of-plane displacements of surrounding nodes are denoted by $w_1, w_2, w_3, w_4, w_5, w_6$. Two other integration contours around neighbouring nodes are shown in black.

The energy cost can be computed by multiplying $f_c(x, y)$ by a scalar and integrating over an area around each node (the Voronoi cell). The total energy can be written as:

$$\bar{E} = E + \iint \lambda f_c \mathrm{d}A = E + \sum_i \iint \lambda_i f_c^i \mathrm{d}A_i \tag{3.4}$$

where $\lambda(x, y)$ is a scalar with energy units, and A_i is the area within the red loop in Figure 3.1b. The summation runs over all nodes i. In order to take advantage of Eqn. (2.11), I take λ to be a constant λ_i within area A_i such that it could come out of each integral. Then I express $\iint f_c^i \mathrm{d}A_i$ as a quadratic expression in terms of the displacement vector $\mathbf{w}$ just as I have done for the plate energy E:

$$\bar{E} = \mathbf{w}\mathbf{M}\mathbf{w}^{\mathrm{T}} + \sum_i \lambda_i \mathbf{w_i}\mathbf{M_i^c}\mathbf{w_i}^{\mathrm{T}}. \tag{3.5}$$

Here $\mathbf{w_i} = [w, w_1, w_2, w_3, w_4, w_5, w_6]$ is a subset of $\mathbf{w}$ which consists of nodal displacement of node i and six adjacent nodes as shown in Figure 3.1b. $\mathbf{M_i^c}$ is a stiffness matrix of compatibility at node i, such that $\iint f_c^i \mathrm{d}A_i = \mathbf{w_i}\mathbf{M_i^c}\mathbf{w_i}^{\mathrm{T}}$. $\mathbf{M_i^c}$ will be computed in the following section. Note that I can verify the effect of imposing compatibility at node i by computing the average value of $\mathbf{w_i}\mathbf{M_i^c}\mathbf{w_i}^{\mathrm{T}}$. This is done by taking the partial derivative of

32

the Gibb's free energy with respect to λ_i as in Su & Purohit (2011, 2012):

$$\langle \mathbf{w_i M_i^c w_i}^{\mathrm{T}} \rangle = \frac{\partial G}{\partial \lambda_i}. \tag{3.6}$$
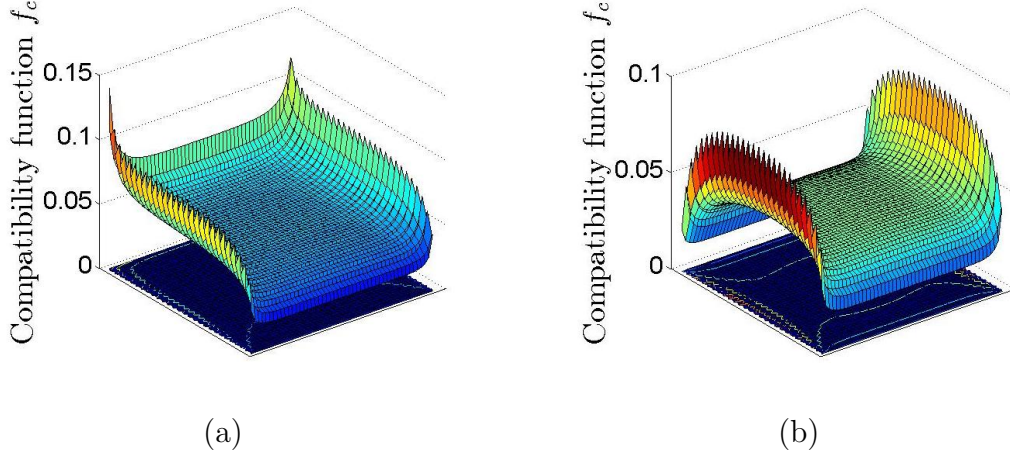
Figure 3.2: The upper surfaces show value of integral of compatibility equation around every node, with (a) one edge hinged and others free , and (b) two edges hinged others free, respectively, for a fluid membrane with zero penalty energy. The lower surfaces (on the order of 10^{-6}) show the same quantity for solid membranes with penalty energy scalar $\lambda = 10^9$ pNnm.

3.3 Compatibility equation in terms of nodal variables

A convenient way to calculate the integral of Gaussian curvature in RHS of Eqn. (3.1) at a node is given by Magid et al. (2007) as:

$$\iint C_G \mathrm{d}A = 2\pi - \sum \gamma_i, \tag{3.7}$$

where γ_i is the angle of the triangle element i sharing this node. Let us assume that our plate is flat initially. I will now compute the angle of one element in terms of arbitrary non-zero node displacements w, w_1, and w_2 as shown in Figure 3.1b. Suppose the original length of the side of each element is l. Then, the deformed length of the three sides are
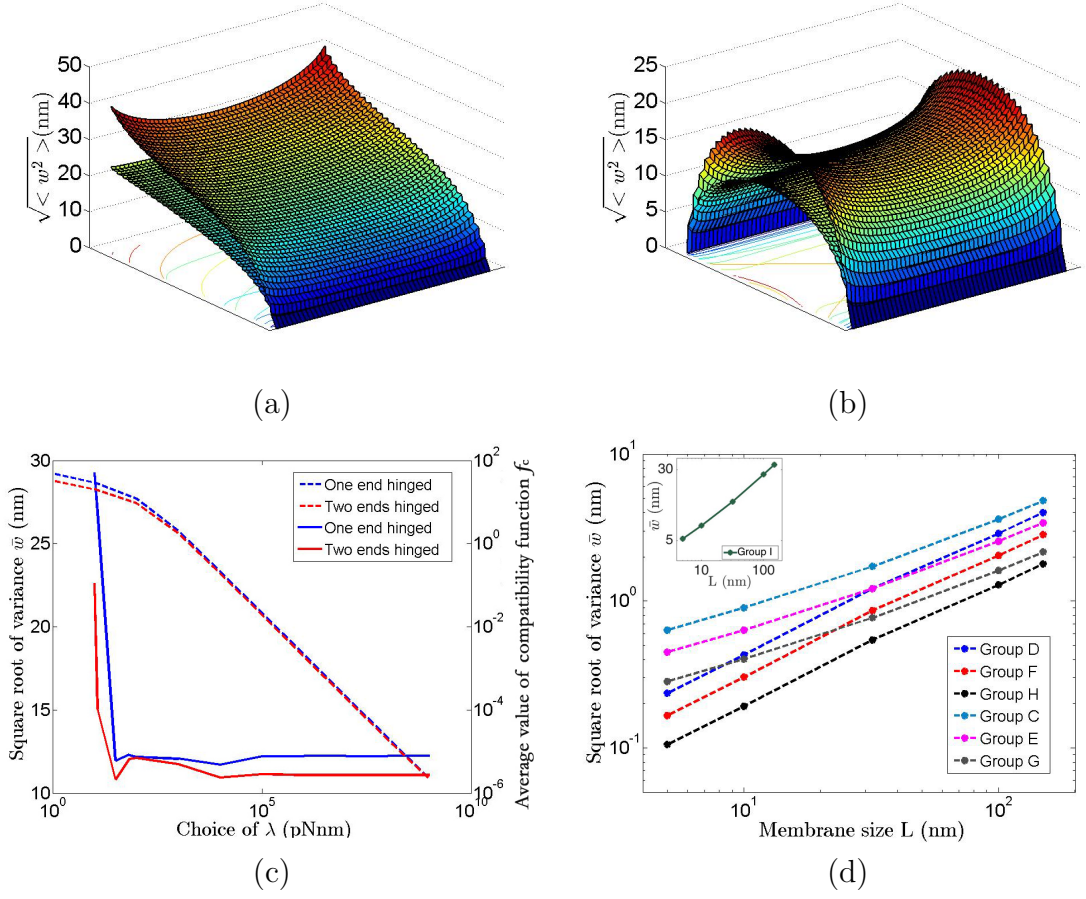
Figure 3.3: (a) and (b) Variance of fluctuating elastic plate with applied hydro-static tension F, with one edge hinged and others free, and two edges hinged others free, respectively. The upper surfaces in (a) and (b) show the fluctuation of a fluid membrane with the same mechanical properties and boundary conditions as our solid plates. (c) The solid lines associated with left axis show how the variance of the fluctuation becomes independent of the penalty energy parameter λ which enforces the compatibility constraint, and the dashed lines associated with right axis show how the average value of compatibility function f_c over all nodes approaches zero as λ becomes sufficiently large. (d) $\bar{w}$ of a fluctuating elastic plate as function of size with two different boundary conditions shown in (a) and (b). The parameters of the membrane are reported in Group C-I in Table 3.1. The inset corresponds to group I in Table 3.1.

related to w, w_1, and w_2 as:

$$
\begin{aligned}
a &= \sqrt{(w - w_1)^2 + l^2}, \\
b &= \sqrt{(w - w_2)^2 + l^2}, \\
c &= \sqrt{(w_1 - w_2)^2 + l^2}.
\end{aligned}
\tag{3.8}
$$

34

So, the deformed angle is given by

$$\gamma = \arccos \frac{a^2 + b^2 - c^2}{2ab}. \tag{3.9}$$

We plug in Eqn. (3.8) and then calculate the change of angle with respect to the original equilateral triangle. In order to carry out the integration for the partition function, I approximate this expression quadratically:

$$\gamma - \frac{\pi}{3} = \frac{2 \left(w_1 - w_2\right)^2 - \left(w - w_1\right)^2 - \left(w - w_2\right)^2}{2\sqrt{3}l^2}. \tag{3.10}$$

We apply this calculation to other triangle elements sharing the node with out-of-plane displacement w and get the integral of the Gaussian curvature at a node as:

$$\iint C_G \mathrm{d}A = \sum_{i=1}^{6} \left(\frac{\pi}{3} - \gamma_i\right)$$
$$= \frac{\sum_{i=1}^{6} \left(w - w_i\right)^2 - \sum_{i=1}^{6} \left(w_i - w_{i+1}\right)^2}{\sqrt{3}l^2}. \tag{3.11}$$

This takes care of the right hand side of the compatibility constraint Eqn. (3.1). The contribution to the elastic bending energy due to the Gaussian curvature can also be calculated using the above formula. Now I focus on the left side of Eqn. (3.1) which involves second derivatives of the in-plane strains. To evaluate the integral of this quantity over a Voronoi cell surrounding a node I choose the boundary of one such cell which is a closed integration contour as shown in Figure 3.1b. Then, from Stokes Theorem I get

$$I = \iint \left(\varepsilon_{x,yy} + \varepsilon_{y,xx} - 2\varepsilon_{xy,xy}\right) \mathrm{d}A$$
$$= \oint \left(\varepsilon_{xy,x} - \varepsilon_{x,y}\right) \mathrm{d}x + \oint \left(\varepsilon_{y,x} - \varepsilon_{xy,y}\right) \mathrm{d}y. \tag{3.12}$$

The terms $\varepsilon_{xy,x}$ and $\varepsilon_{xy,y}$ in the integrands will contribute zero because our integration contour is closed. Hence, I am left with

$$I = \oint \varepsilon_{y,x} \mathrm{d}y - \oint \varepsilon_{x,y} \mathrm{d}x. \tag{3.13}$$

35

Now I plug Eqns. (2.2) into the above integral, and similarly drop those terms in the integrands whose contribution will be zero due to the closed contour. Finally, I am left with

$$I = \oint \left[\frac{1}{2} \frac{\partial}{\partial x} \left(\frac{\partial w}{\partial y} \right)^2 \mathrm{d}y - \frac{1}{2} \frac{\partial}{\partial y} \left(\frac{\partial w}{\partial x} \right)^2 \mathrm{d}x \right]. \tag{3.14}$$

The expression above can be easily evaluated in terms of the nodal variables for each element. Thus, both sides of Eqn. (3.1), or the compatibility function f_c, could be evaluated upto quadratic order in the displacements $\mathbf{w_i}$ at the nodes, governed by matrix $\mathbf{M_i^c}$ in Eqn. (3.5). I will now choose all λ_i equal to a same value λ because there is no reason to penalize two nodes differently. Then, the energy expression

$$\bar{E} = \mathbf{w}\mathbf{M}\mathbf{w}^{\mathrm{T}} + \lambda \sum_i \mathbf{w_i}\mathbf{M_i^c}\mathbf{w_i}^{\mathrm{T}}. \tag{3.15}$$

We will now show that λ contributes to the fluctuation through the boundaries. Note that in Figure 3.1b, the integration contours around two adjacent nodes share one edge which is traversed in opposite directions. Therefore, if I choose λ to be the same for these two nodes, then the integration in Eqn. (3.14) along this edge will cancel due to opposite signs of the contribution from the two contours that share it. Similarly, if λ is chosen to be the same for all nodes, this cancellation will happen for all edges in the interior of the plate, and the entire energy penalty due to the compatibility constraint goes to the boundary of the plate. This is not surprising if one remembers the Gauss-Bonet theorem for the integral of the Gaussian curvature Chen & Rong (2010). Thus, the summation of the energy cost of violating the compatibility constraint at each node can be written as a quadratic form:

$$\sum_i \mathbf{w_i}\mathbf{M_i^c}\mathbf{w_i}^{\mathrm{T}} = \mathbf{w}\mathbf{M_c}\mathbf{w}^{\mathrm{T}}, \tag{3.16}$$

where the matrix $\mathbf{M_c}$ has non-zero entries only for the boundary nodes. Furthermore, I find that $\mathbf{M_c}$ is positive semi-definite irrespective of the boundary conditions, so that I only need to consider $\lambda > 0$ in Eqn. (3.15). Now, in order to enforce the compatibility constraint I choose λ sufficiently large so that the variance of out-of-plane deflections $w(x, y)$ is independent of λ. In reality, by doing so I have required that f_c is close to zero on average over the whole plate. In order to justify this weaker constraint, we will compute $\langle \iint f_c^i \mathrm{d}A_i \rangle$ over a Voronoi cell surrounding each node to make sure they are approaching zero as well.

Table 3.1: Parameters used in the computations of solid membranes.

Group	L or L_1(nm)	K_b(pNnm)	K_G(pNnm)	F(pNnm^{-1})	Boundary condition	N
A	1000	82	-53.3	0.001	One end hinged	50
B	1000	82	-53.3	0.001	Two ends hinged	50
C	5-150	41	-26.65	0	One end hinged	50
D	5-150	41	-26.65	0	Two ends hinged	50
E	5-150	82	-53.3	0	One end hinged	50
F	5-150	82	-53.3	0	Two ends hinged	50
G	5-150	205	-133.25	0	One end hinged	50
H	5-150	205	-133.25	0	Two ends hinged	50
I	5-150	3.28	-2.132	0	One end hinged	50
J	1000 $(= L_2)$	82	-53.3	0	Shear $S = 0.001$pNnm^{-1}	50
K	1000 $(= L_2)$	82	-53.3	0	Shear $S = 0.01$pNnm^{-1}	50
L	1000 $(L_2 = 500)$	28.7	-18.655	0	Shear $S = 0.01$pNnm^{-1}	50

This is exactly the quantity in Eqn. (3.6). We examine it at every node i for a solid membrane and a fluid membrane in Figure 3.2a for two different boundary conditions as given in section 2.4. Since this quantity is very small (on the order of 10^{-6}) at all nodes for the solid membrane I have ensured that the compatibility equation is satisfied everywhere. In contrast for a liquid membrane with the same mechanical properties and boundary conditions f_c is much larger as seen in Figure 3.2a. I also show (a) how the variance of the fluctuations of a solid membrane in Figure 3.3a and 3.3b becomes independent of λ as it becomes sufficiently large (see the solid lines associated with left axis), and (b) how the average value of f_c over all nodes approaches zero as λ becomes sufficiently large (see the dashed line associated with right axis). I see that $\lambda = 10^9$pNnm is a large enough value and use it in all our subsequent calculations of the variance. The stage is now set to examine the effect of boundary conditions on a fluctuating graphene sheet.

3.4 Analysis of variance and effect of boundary conditions

One important result which follows from the calculation of the partition function is the co-variance matrix $\langle w_i w_j \rangle$ Zhang & Crothers (2003), Su & Purohit (2010, 2011, 2012), which can be calculated from the inverse of the stiffness matrix $\mathbf{M}$ as

$$\langle w_i w_j \rangle = \frac{k_B T}{[\mathbf{M}^{-1}]_{ij}}. \tag{3.17}$$

From this I can get the variance of the out-plane deflection $\langle w_i^2 \rangle$ as a function of reference position on our membrane. We choose membrane size, bending moduli, tension, boundary condition and finite element discretization as given in Table 3.1. First, I examine the overall variance profile of the whole plate with two different boundary conditions – (a) one edge hinged, three edges free, (b) two opposite edges hinged, two edges free. The variance is plotted as function of node position in the reference configuration shown in Figure 3.3a and 3.3b. The results correspond to computation groups A and B in Table 3.1. In order to show the effect of the compatibility constraint, I plot the variance profile of a fluid membrane with the same K_b and K_G in each plot for comparison. Recall that since a fluid membrane has zero in-plane shear modulus I can choose $\varepsilon_{xy}(x,y)$ to satisfy the compatibility equation for a given out-of-plane deflection profile $w(x,y)$ and in-plane strain profile $\varepsilon_x(x,y)$, $\varepsilon_y(x,y)$. The compatibility constraint reduces the thermal fluctuations of solid membranes compared to solid membranes for the same boundary conditions.

Second, I examine the relation between variance and membrane size while fixing the mechanical properties. An earlier theoretical result gives that the average fluctuation $\bar{w}$ (square root of variance) scales with some power of membrane size L, or as L^δ. δ is proved to be 1 for a fluid membranes as in Nelson et al. (2004), Fasolino et al. (2007), and around $0.6 - 0.8$ as given in Nelson et al. (2004), Fasolino et al. (2007), Le Doussal & Radzihovsky (1992), Abraham & Nelson (1990) for solid membranes. We recover this power law scaling in our calculations as shown in Figure 3.3d. The parameters of our membrane are chosen from group C to H in Table. 3.1. However, I find that the power δ for a given solid membrane depends on the boundary conditions. When only one edge is hinged and the others are free $\delta = 0.8321$, when two opposite edges are hinged and two are free $\delta = 0.5968$. These powers are close to the range given in Nelson et al. (2004), Fasolino et al. (2007).

In the analysis given by Lipowsky & Girardet (1990), Boal & Boal (2012), an ideal membrane with non-zero in-plane shear resistance μ, but zero bending resistance K_b, has been shown to have an average thermal fluctuation $\bar{w} \propto L^{0.5}$ given by

$$\bar{w} = 0.62 L^{0.5} \left(\frac{k_B T}{Y} \right)^{0.25}. \tag{3.18}$$

The fluctuating plate model studied in our paper is neither this ideal membrane (with $K_b = 0$, $\mu \neq 0$), nor a fluid membrane (with $K_b \neq 0$, $\mu = 0$). Therefore, the resulting

power is between 0.5 and 1 and it depends on the applied boundary condition. In order to further verify our model, I give results from another calculation in the inset of Figure 3.3d using parameters from group I in Table 3.1. I cannot choose the bending modulus K_b and Gaussian curvature modulus K_G to be exactly zero since this results in a singular stiffness matrix $\mathbf{M}$. So, I choose K_b and K_G to be smaller than the thermal energy scale $1k_BT$. I find in Figure 3.3d inset that the power δ for this membrane is $\delta = 0.5542$, which is closer to the theory in Lipowsky & Girardet (1990), Boal & Boal (2012).

(a)   (b)   (c)
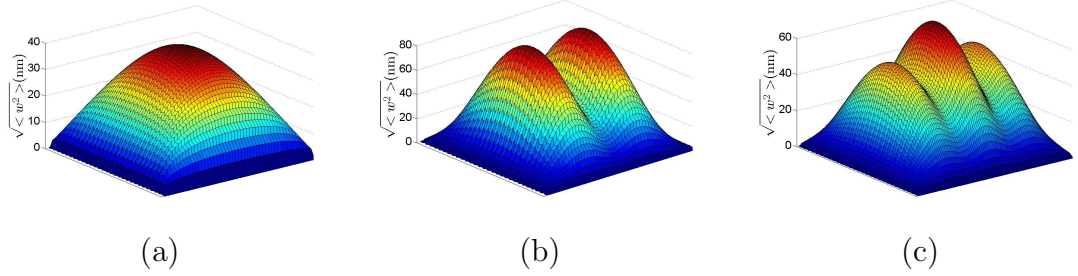
Figure 3.4: Distinct variance profiles of a sheet under shear loading as given in Group J, K, L of Table 3.1. (a) Mode $n = 1$, $m = 1$ has the largest amplitude. (b) Mode $n = 1$, $m = 2$ has the largest amplitude. (c) Mode $n = 1$, $m = 3$ has the largest amplitude.

3.5   Study of ripples under shear loading

An interesting possibility for us is to replace the hydro-static tension F with some other boundary condition, for example a shear loading S as in Min & Aluru (2011). Along one pair of opposite edges, I apply a tension of magnitude $+S$, while along the other pair of opposite edges, I apply a compression $-S$. This will result in shear loading on the plate. To account for this loading, Eqn. (2.3) is changed to:

$$\begin{aligned}
E_f &= -\iint S\left(u_{,x} - v_{,y}\right) \mathrm{d}x\mathrm{d}y \\
&= -\iint S\left(\varepsilon_x - \frac{w_{,x}^2}{2} - \varepsilon_y + \frac{w_{,y}^2}{2}\right) \mathrm{d}x\mathrm{d}y.
\end{aligned} \tag{3.19}$$

This results in a sign change in Eqn. (3.2) as:

$$
\begin{aligned}
E = \iint \mathrm{d}x\mathrm{d}y &\left[\frac{K_b}{2} (w_{,xx} + w_{,yy})^2 \right. \\
&\left. + K_G \left(w_{,xx}w_{,yy} - w_{,xy}^2 \right) + S \left(\frac{w_{,x}^2}{2} - \frac{w_{,y}^2}{2} \right) \right].
\end{aligned}
\tag{3.20}
$$

In Table 3.1, group J-L I give parameters for this type of problem. The resulting variance profiles for the out-of-plane deflection are given in Figure 3.4 for three different combinations of parameters. All three membranes are simply supported on the four edges. Each combination of properties results in a distinct variance profile. Next, I am going to explain the relation between the parameters and the variance profile obtained from our computation. Due to hinged boundary conditions on all edges the deflections $w(x,y)$ of our plate can be expressed as a double Fourier series Boal & Boal (2012):

$$
w(x, y) = \sum_{(m,n)} q_{mn} \sin\left(\frac{n\pi x}{L_1} \right) \sin\left(\frac{m\pi y}{L_2} \right),
\tag{3.21}
$$

where q_{mn} is the amplitude of the normal mode corresponding to m, n. Note that I assume our plate to be rectangular with sides L_1 in x direction and L_2 in y direction. When I plug the above expression into Eqn. (3.20) I get:

$$
E = \sum_{(m,n)} q_{mn}^2 \left[\frac{Kb\pi^4}{8L_1L_2} \left(n^2 + m^2 \right)^2 + \frac{S\pi^2}{8} \left(n^2 - m^2 \right) \right].
\tag{3.22}
$$

From the equipartition theorem of statistical mechanics Landau & Lifshitz (1986), each Fourier mode (m,n) should possess energy $k_B T/2$. Therefore, I can compute the amplitude of each mode as:

$$
\langle q_{mn}^2 \rangle = \frac{4k_B T L_1 L_2}{K_b \pi^4 \left(n^2 + m^2 \right)^2 + S L_1 L_2 \pi^2 \left(n^2 - m^2 \right)}.
\tag{3.23}
$$

Therefore, the mode (m,n) with maximum amplitude should be given by:

$$
n = 1; \qquad m = \left[\frac{\sqrt{1 + \frac{2SL_1L_2}{K_b\pi^2}} - 1}{2} \right],
\tag{3.24}
$$
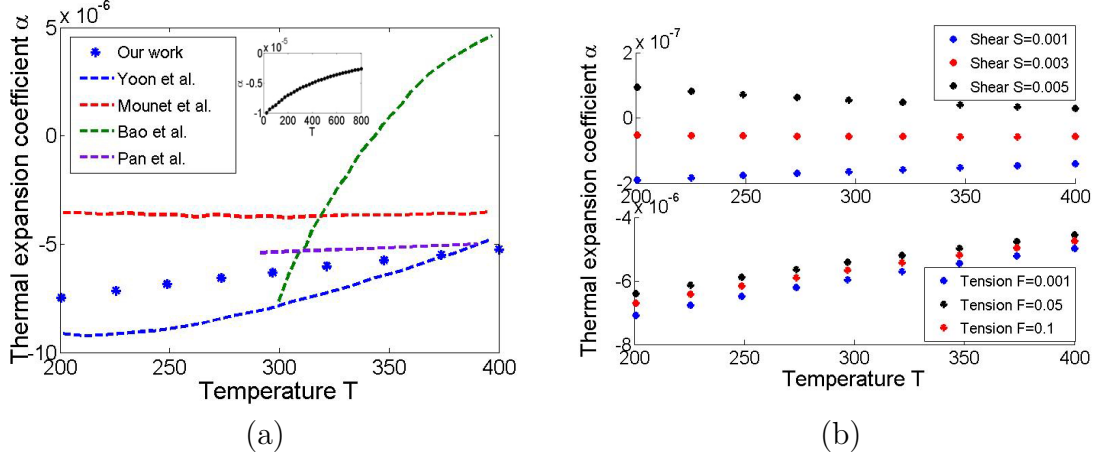
Figure 3.5: (a) Prediction of graphene layer thermal expansion coefficient. Dots are the result of our semi-analytic method; blue, green, and purple lines are experimental results respectively by Yoon et al. (2011), Bao et al. (2009), and Pan et al. (2012); red line is theoretical work by Mounet & Marzari (2005). The inset shows α as a function of T over a broader temperature range. (b) Prediction of graphene layer thermal expansion coefficient under distinct shear loading (upper panel), and hydro-static tension (lower panel), the unit in the legends is pNnm^{-1}.

where $[\cdot]$ gives the nearest positive integer. The mode shapes observed in Figure 3.4a-3.4c are consistent with the result of plugging parameters of Group J-L into Eqn. (3.24). The mode making the dominant contribution to the variance changes with the loading because solid membranes can support shear. In contrast, in fluid membranes the dominant contribution to the variance always comes from the lowest normal mode $n = 1, m = 1$ because they can only sustain hydro-static tension. It is trivial to extend these calculations to combined hydro-static and shear loading on the plate. It is evident from the above results that different loading and boundary conditions will result in different ripple profiles in fluctuating solid plates.

3.6 Quantitative analysis of the negative thermal expansion coefficient of graphene

We will use our model to analyze the negative thermal expansion coefficient of graphene which is around $-10^{-6}K^{-1}$. This remarkable feature of graphene has been measured and predicted in Fasolino et al. (2007), Yoon et al. (2011), Bao et al. (2009), Pan et al. (2012), Mounet & Marzari (2005). However, all these works were based either on experiment or

molecular simulation. Here I give a quantitative explanation for the negative thermal expansion coefficient using our fluctuating elastic plate model. The Gibbs free energy $G(F, T)$ of the whole plate is related to the partition function Z as $G = -k_B T \ln Z$. We can compute the properties of the plate by computing derivatives of the free energy. First, the reduction in projected area caused by thermal fluctuation is given by $\Delta A = A(\infty, T) - A(F, T)$, where $A(\infty, T)$ is the membrane area at very large tension such that all the undulations are stretched out and it is flat. The area reduction is conjugate to the tension F in the free energy of the membrane, and can be computed as $\Delta A = -\partial G / \partial F$. Since all the terms related to the force F in the expression for the partition function Z are included in the matrix $\mathbf{M}$, I have

$$\frac{\Delta A}{A} = -\frac{k_B T}{2A} \frac{\partial}{\partial F} \ln\left(\det \mathbf{M}\right), \tag{3.25}$$

where A is original area of the membrane at zero tension and zero temperature. The increase in out-of-plane bending deflections of the plate at higher temperatures reduce the projected area and result in a negative thermal expansion coefficient. The dependence of the bending modulus K_b on the temperature also contributes to the thermal expansion coefficient. This dependence has been studied in Fasolino et al. (2007) and I summarize it through the following fit:

$$K_b = 131.36 + 200 \cdot \tanh \frac{T}{1500}, \tag{3.26}$$

where the units of K_b and T are pNnm and K, respectively. I evaluate $\Delta A / A$ at $F = 0.001$ pN/nm of a 100 nm-by-100 nm graphene sheet, for various values of T. By differentiating Eqn. (3.25) with respect to temperature T I get the thermal expansion coefficient:

$$\alpha = -\frac{\partial^2}{\partial T \partial F}\left[\frac{k_B T}{2A} \ln \det \mathbf{M}\right]. \tag{3.27}$$

We plot our result in Figure 3.5a together with other simulation and experimental results. It is apparent that our method agrees quite well with earlier work. In particular, I find that the thermal expansion coefficient increases with increasing temperature as has been found in several experiments Yoon et al. (2011), Bao et al. (2009), Pan et al. (2012). Although experimental data for α is available over a range $200 - 400$K, I have shown in the inset of Figure 3.5a that $\alpha < 0$ over a much broader range upto 800K. I also must not lose sight of the fact that this figure assumes that the physics behind the negative α is bending

fluctuations, which may not be the right physics for a solid near 0 K. I also carefully examine the effect of distinct hydrostatic tension and shear loading on thermal expansion coefficient as given in Figure 3.5b. I see that hydrostatic tension does not affect the thermal expansion coefficient much. The shear loading, however, enormously affects it. Firstly, as the shear load increases, the slope with respect to temperature T changes from positive to negative. Secondly, at shear loading equal to 0.001 pNnm^{-1}, the thermal expansion coefficient becomes positive. Note also that the slope of the α vs. T curve is related to the heat capacity $C_F = -T\partial^2 G/\partial T^2$ at given tension F or shear loading S through

$$\frac{\partial \alpha}{\partial T} = -\frac{1}{A}\frac{\partial^3 G}{\partial F \partial T^2} = \frac{1}{AT}\frac{\partial C_F}{\partial F}. \tag{3.28}$$

In Figure 3.5b top panel I see that this slope changes sign at a certain value of S. The equation above shows that a measurement of the heat capacity as a function of S can be a good way of testing our predictions in addition to experiments of the type carried out in Yoon et al. (2011), Bao et al. (2009), Pan et al. (2012).

Chapter 4

Inclusions in membranes

If two similar proteins bind to a lipid bilayer separated by a distance r then the elastic deformation field around one of them can produce a repulsive force on the other one Golestanian et al. (1996). This force decays as $1/r^4$ as has been deduced from studies of proteins interacting through elastic deformations of a lipid bilayer Ruiz-Herrero & Hagan (2015), Kim et al. (1998), Yolcu et al. (2014), Müller & Deserno (2010), Schweitzer & Kozlov (2015), Yolcu et al. (2014), Ruiz-Herrero & Hagan (2015), Yuan et al. (2011), Huang et al. (2011). Lipid membranes also fluctuate due to Brownian motion. This results in an attractive entropic force between two similar proteins Ruiz-Herrero & Hagan (2015), Yolcu et al. (2014). The competition between attractive and repulsive forces can lead to self-assembly of proteins on a lipid bilayer membrane Dommersnes & Fournier (2002), Reynwar et al. (2007). This sort of self-assembly determines the shape of a cell membrane and plays a role in endo- and exo-cytosis by the formation of localized invaginations or buds. For example, bud formation happens when capsid proteins of viruses, like HIV and influenza, land on lipid membranes and self-assemble Ruiz-Herrero & Hagan (2015). Similarly, the protein endophilin clusters together on lipid membranes and causes the formation of cylindrical tubules, and thus, it plays a role in membrane trafficking events in a cell Farsad et al. (2001). The early stages of self-assembly of certain amyloid forming proteins (which cause Alzheimer's and Parkinson's diseases) also involves self-assembly of monomers on a lipid membrane Pannuzzo et al. (2013). Since self-assembly often involves much more than two proteins, the interactions between many proteins on a membrane have been studied and it has been learned that pair-wise expressions are not sufficient to describe these many
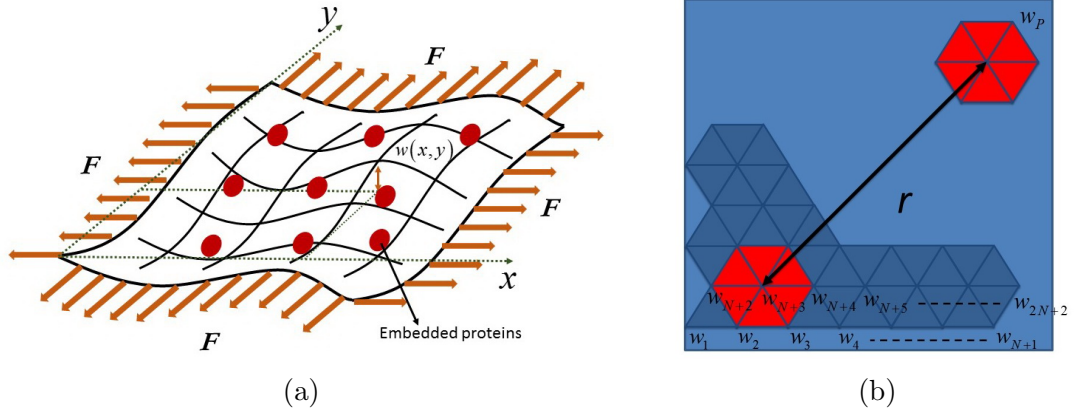
Figure 4.1: (a) Schematic figure of a fluctuating membrane with applied hydro-static tension F. The out-of-plane deflection of reference point (x, y) is $w(x, y)$. The red circles are embedded proteins, or inclusions. (b) Equilateral triangle element discretization scheme of a square membrane. The inclusions are represented by hexagons consisting of many triangle elements. I keep the element size fixed, so the number of triangle elements in an inclusion depends on the size of the inclusion.

body interactions Kim et al. (1998). However, analytic studies of these many body interactions account for membrane bending deformations only. The entropic component of the interactions has been studied recently using simulations and a sophisticated field theory Yolcu et al. (2014), Müller & Deserno (2010). The field theory relies on the idea that the height fluctuations of the membrane are small, so the bending energy can be written as a quadratic form. This leads to Gaussian path integrals that can be evaluated analytically, but not without difficulty Yolcu et al. (2014).

Our overarching goal in this Chapter is to study elastic and entropic forces between many inclusions on lipid membranes using computational methods based on Gaussian integrals. Although mechanical and thermodynamic properties of lipid membranes, including how inclusions (such as, proteins) effect the overall membrane behavior, have been quantitatively studied using experimental,theoretical and computational methods Evans & Rawicz (1990), Helfrich (1973), Weeks (1977), Helfrich (1975), Boal & Boal (2012), Milner & Safran (1987), Lindahl & Edholm (2000), Agrawal et al. (2016), it is not always possible to design an experiment for large scale problems involving membrane protein interactions, and also the sample scale is too large for molecular simulations. To overcome these difficulties, researchers have turned to continuum modeling and associated computational methods Kahraman et al. (2016) to study large scale (more than several microns) problems involving
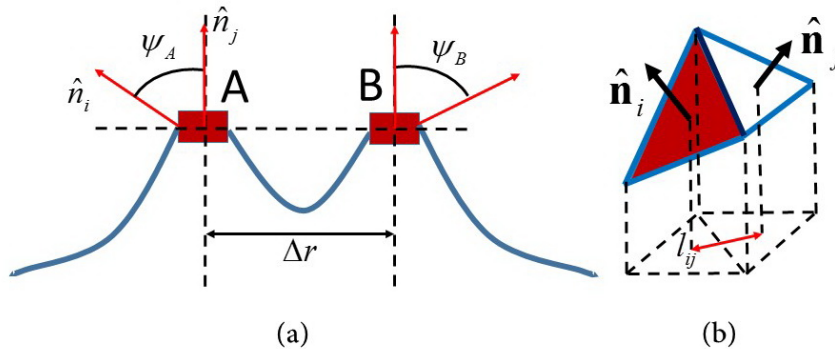
Figure 4.2: (a) The equilibrium shape of a membrane with two proteins embedded in it and separated by a distance Δr. The proteins are rigid cylinders which enforce contact angles ψ_A and ψ_B with respect to adjacent membrane. In section 4.2.1, I will fix these angles to a given value as an enforced boundary condition. (b) Unit normal vectors $\hat{n}_i$ and $\hat{n}_j$ of two elements sharing one protein-membrane boundary edge. l_{ij} is the reference length between the center of these two triangle elements. Red triangle is protein element.

protein interactions on membranes. Unlike molecular simulation (such as, Monte Carlo and Molecular Dynamics based studies Lindahl & Edholm (2000), Agrawal et al. (2016)) these continuum methods do not include Brownian fluctuations. Our technique described below can potentially be combined with continuum computational methods to account for entropic effects arising from Brownian fluctuations.

4.1 Theory

4.1.1 Protein-membrane interaction energy

A lipid bilayer membrane in a live cell has proteins embedded in it as shown in Figure 4.1a, whose size is a few nanometers. These proteins are much stiffer than lipid molecules and they have strong interactions with their surrounding lipids Kahraman (2015). The embedded proteins change the local shape of the membrane and affect both the elastic and entropic parts of the membrane free energy. I will now apply our semi-analytic method described above to the study the effect of membrane inclusions. I model each protein by assigning some of the triangle elements with much larger bending stiffness (10^3 pNnm for all computations in this paper) than the lipid membrane as shown in Figure 4.1b. Also, I fixed the displacement of all the protein nodes to be zero to compute the bending energy. Thus, I am assuming the proteins to be rigid disks in comparison to the membrane. An

46

advantage of assuming rigid inclusions is that I do not have to account for the energy due to Gauss curvature in our calculations Kim et al. (1998). One protein could contain 6, 24, or 54 equilateral triangle elements depending on its size. The protein-membrane interaction at the boundary of each protein (labeled A, B, $\cdots$) is modeled by uniform contact angles $\psi_A, \psi_B, \cdots$. Here ψ_A is the angle between the boundary triangle elements of protein A and the adjacent membrane triangle elements shown in Figure 4.2a. If we remember that the displacement of all nodes on the proteins is zero then the displacement of protein-adjacent membrane nodes is $w = \frac{\sqrt{3}}{2} l \sin \psi_A$. Since all our boundary conditions are specified node displacements we solve for the displacements of all other nodes comprising the membrane using standard techniques in the finite element method (see, for example, Bathe (2006)). Once the displacements of all nodes are known the elastic energy can be immediately computed. To compute the entropic contribution to the free energy we add a penalty energy E_p to Eqn. (2.10), very similar to earlier works Liang & Purohit (2016b), Zhang & Crothers (2003). Here the penalty energy is written as the sum:

$$E_p = \lambda \sum_C \left(\psi_A - \psi \right)^2, \tag{4.1}$$

where ψ is chosen to be 0.1 for every computations, and λ is a penalty energy coefficient, which is chosen to be large enough (e.g. $\lambda = 10^{12}$ in Liang & Purohit (2016b)) to ensure that the probability of configurations violating the boundary condition is extremely small in the partition sum for Z. The contour C is the boundary of all the proteins, thus I have tacitly assumed that all proteins have the same contact angle with the membrane. I can, of course, impose a different contact angle at every protein, but I do not do so here for simplicity. ψ_A could be expressed as the absolute value of the difference between unit normal vectors $\hat{n}_i, \hat{n}_j$ of the two elements sharing one boundary edge as in Figure 4.2b, or

$$\psi_A = |\hat{n}_i - \hat{n}_j|.^1 \tag{4.2}$$

Recall that $\hat{n}_i$ and $\hat{n}_j$ can be represented by quadratic expressions of node displacement variables $[w_1, w_2, ..., w_P]$. Therefore, I can write the penalty energy by an algebraic expres-

---

[1]This is by assuming ψ_A to be small such that $\cos \psi_A = 1 - \psi_A^2/2$. Therefore, $|\hat{n}_i - \hat{n}_j|^2 = 2 - 2\hat{n}_i \cdot \hat{n}_j = 2 - 2\cos \psi_A = \psi_A^2$.

sion

$$E_p = \mathbf{w}\mathbf{M_P}\mathbf{w}^{\mathrm{T}} + \mathbf{w} \cdot \mathbf{C_p} + C, \tag{4.3}$$

where $\mathbf{C_p}$ is a vector and C is a constant. Now, I perform the same exercise as in Liang & Purohit (2016a); I replace the stiffness matrix $\mathbf{M}$ in Eqn. (2.11) with a new matrix $\mathbf{M} + \mathbf{M_P}$ taking care of both membrane energy as well as penalty energy, and rewrite the energy expression as:

$$E + E_p = (\mathbf{w} - \bar{\mathbf{w}})(\mathbf{M} + \mathbf{M_P})(\mathbf{w} - \bar{\mathbf{w}})^{\mathrm{T}} + \bar{C}. \tag{4.4}$$

where the equilibrium position $\bar{\mathbf{w}}$ has been computed before and C is a constant taking care of the equilibrium position energy. Finally, I carry out the integral for the partition function:

$$Z = \exp\left(-\frac{\bar{C}}{k_B T}\right) \sqrt{\frac{(2\pi k_B T)^P}{\det(\mathbf{M} + \mathbf{M_P})}}. \tag{4.5}$$

The membrane free energy with inclusions is thus given by:

$$G = -k_B T \ln Z = \bar{C} + \frac{k_B T}{2} \ln \det(\mathbf{M} + \mathbf{M_P}) + G_0. \tag{4.6}$$

Here the first term takes care of the elastic contribution, which is independent of temperature, and the second term takes care of the entropic contribution, which increases linearly with temperature, and G_0 is a constant.

4.2 Results

4.2.1 Interaction of two inclusions

The first problem solved using our method is to compute the interactions between two proteins on a lipid bilayer as shown in Figure 4.1b. I can compute both the elastic and entropic parts of the free energy of this lipid membrane as a function of a protein separation distance r. I choose a membrane with side $L = 500$ nm and a discretization scheme with $N = 200$, resulting in an element size $l = 2.5$ nm because it resulted in excellent agreement between our computations and the analytic expressions for membrane entropy Liang & Purohit (2016a). The bending modulus is varied from $5k_B T$ to $20k_B T$ and membrane

48
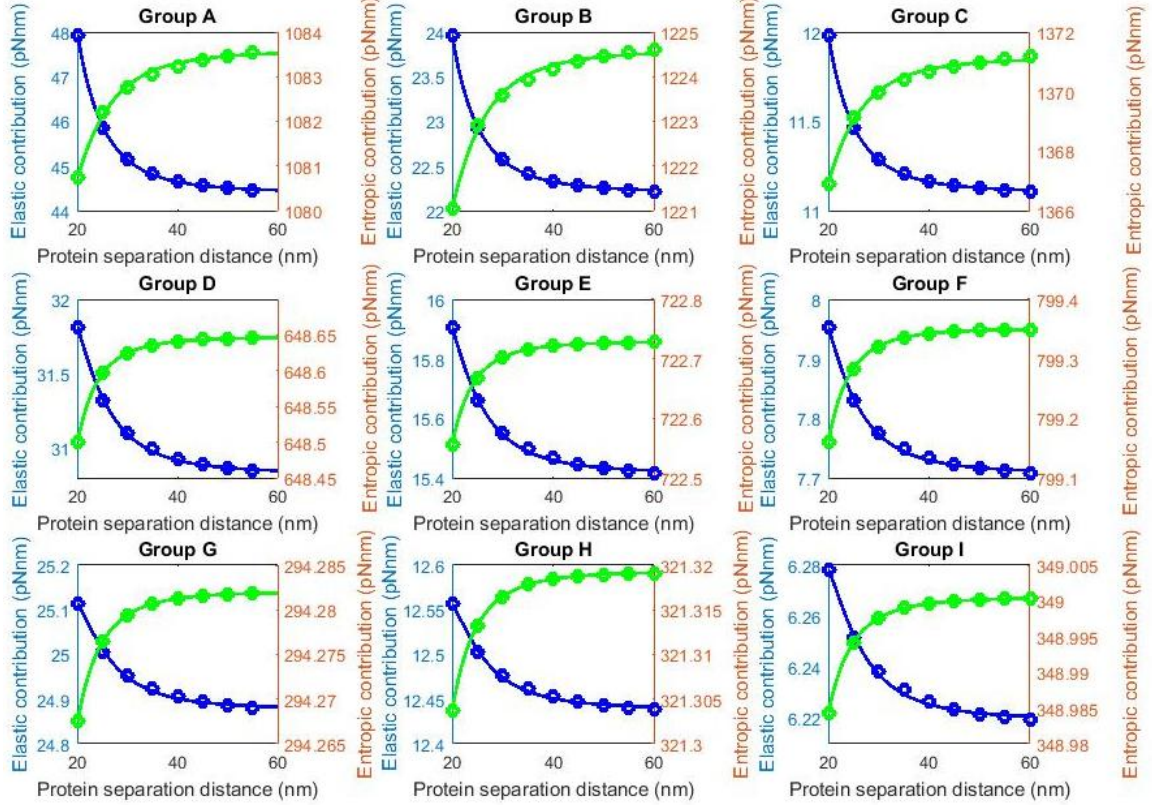
Figure 4.3: Results for computations with two inclusions on a membrane with properties summarized in Table 4.1. Circles are computation results and solid lines are theoretical fits using Eqn. (4.7). Blue and green data, associated with left and right y-axis respectively, correspond to elastic and entropic parts of the membrane free energy.

Table 4.1: Parameters used in the two protein computations.

Group	L(nm)	Element size(nm)	K_b (pNnm)	Protein size(nm)	tension F (pNnm^{-1})	a_{el} (pNnm^5)	a_{en} (pNnm^5)	c_{el} (pNnm^9)	b_{en} (pNnm^7)	r_{cr} (nm)
A	500	2.5	82	7.5	0	5.86×10^5	-8.72×10^5	-3.90×10^9	1.29×10^8	-
B	500	2.5	41	7.5	0	2.93×10^5	-9.41×10^5	-1.96×10^9	1.50×10^8	-
C	500	2.5	20.5	7.5	0	1.46×10^5	-9.97×10^5	-9.76×10^8	1.69×10^8	-
D	500	2.5	82	5	0	2.25×10^5	-1.40×10^4	-1.09×10^{10}	4.34×10^6	-
E	500	2.5	41	5	0	1.12×10^5	-1.69×10^4	-5.45×10^9	4.73×10^6	-
F	500	2.5	20.5	5	0	5.56×10^4	-1.87×10^4	-2.72×10^9	4.72×10^6	-
G	500	2.5	82	2.5	0	6.21×10^4	-1.97×10^3	-3.94×10^9	1.43×10^5	-
H	500	2.5	41	2.5	0	3.11×10^4	-2.13×10^3	-1.97×10^9	1.47×10^5	-
I	500	2.5	20.5	2.5	0	1.55×10^4	-2.23×10^3	-9.86×10^8	1.51×10^5	-
J	500	2.5	6.15	2.5	0	4.66×10^3	-2.31×10^3	-2.96×10^8	1.52×10^5	25
K	500	2.5	4.1	2.5	0	3.11×10^3	-2.33×10^3	-1.97×10^8	1.46×10^5	30
L	500	2.5	3.28	2.5	0	2.49×10^3	-2.33×10^3	-1.58×10^8	1.34×10^5	35
M	500	2.5	2.87	2.5	0	2.18×10^3	-2.28×10^3	-1.38×10^8	1.40×10^5	40
N	500	2.5	3.69	2.5	0.00001	2.80×10^3	-2.30×10^3	-1.77×10^8	1.62×10^5	35
O	500	2.5	3.69	2.5	0.0005	2.88×10^3	-2.34×10^3	-1.87×10^8	1.46×10^5	35
P	500	2.5	3.69	2.5	0.005	2.82×10^3	-1.93×10^3	-1.76×10^8	2.60×10^5	40

49
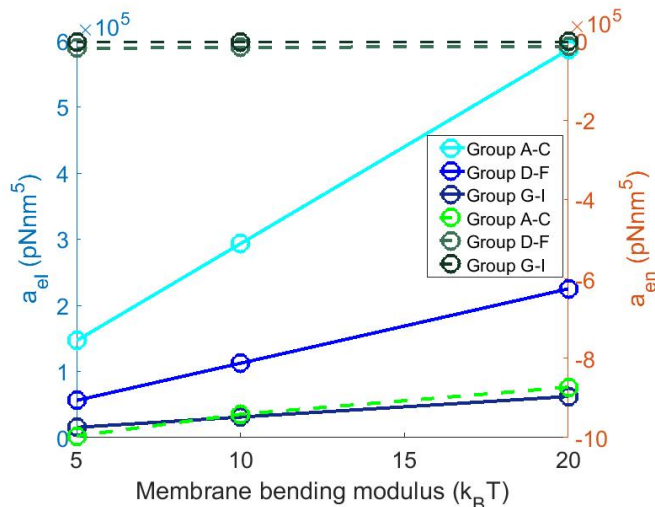
Figure 4.4: Dependence of fitting parameters a_{el} and a_{en} in Eqn. (4.7) on membrane bending modulus and protein size. The blue solid lines associated with the left y-axis are result for a_{el}, which increases roughly linearly with K_b. The green dash lines associated with the right y-axis are results for a_{en}, which are almost independent of K_b (a_{en} decreases very slowly with decreasing K_b).

tension is set to zero. I hinge all four sides of the membrane. The proteins contain 6, 24, or 54 equilateral triangle elements depending on their radius R. The results for various computation groups in Table 4.1 are shown in Figure 4.3. In each plot the distance r is on the x-axis, the elastic part of the free energy (blue curve and circles) is on the left y-axis and the entropic part of the free energy (green curve and circles) is on the right y-axis.

We see in all the computation groups that the entropic part of the free energy increases with protein separation distance and the elastic part decreases with protein separation distance. The dependence of both entropic and elastic parts of the free energy has been studied analytically in Yolcu et al. (2014) and references therein. It is known that the elastic and entropic parts of the free energy of a membrane with two identical rigid circular disks whose centers are a distance r apart take the form (to lowest order in $1/r$):

$$
\begin{aligned}
U_{el}(r) &= \frac{a_{el}}{r^4} + \frac{c_{el}}{r^8} + O(\frac{1}{r^{10}}), \\
U_{en}(r) &= \frac{a_{en}}{r^4} + \frac{b_{en}}{r^6} + \frac{c_{en}}{r^8} + O(\frac{1}{r^{10}}).
\end{aligned}
\tag{4.7}
$$

The subscript $_{el}$ and $_{en}$ indicate elastic and entropic parts, respectively. Note that the r^{-6} term in the elastic part of the free energy is zero because the two inclusions are identical Yolcu et al. (2014). I obtained a_{el}, a_{en}, b_{en}, etc., by fitting each computation group in

50
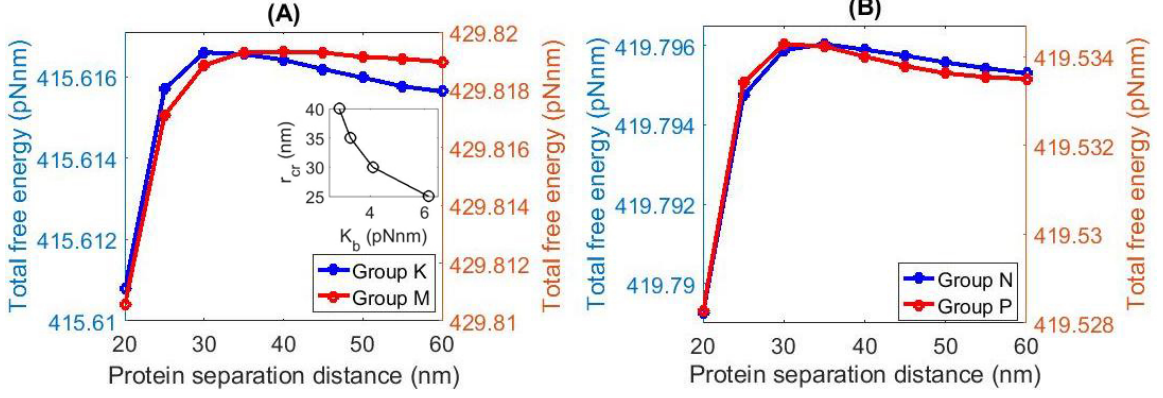
Figure 4.5: Total free energy profile of selected groups in Table 4.1. (A) The position of the maximum r_{cr} moved to the right as bending modulus increased. (B) The position of the maximum moved to the right as tension increased. The blues lines and red lines are associated with left and right y-axis respectively. The inset in (A) shows the position of the maximum, r_{cr}, as a function of K_b for zero tension as (see Group J-M in Table 4.1) as dots.

Table 4.1 using Eqn. (4.7) as shown by the solid lines in Figure 4.3. The fitting parameters are given in Table 4.1. The fitting parameter a_{el} should scale with $K_b\psi_A^2 R^4$, while fitting parameter a_{en} should scale with $k_B T R^4$ and be independent of K_b if the inclusions are circular discs of radius R as in Yolcu et al. (2014). In Figure 4.4 I see that our a_{el} increases roughly linearly with bending modulus K_b, and a_{en} remains almost unchanged as bending modulus increases from $5k_B T$ to $20k_B T$, which agrees with the analytic theory based on Gaussian integrals Yolcu et al. (2014). We see from Table 4.1 that a_{el}, a_{en} and b_{en} increase with protein size, as expected. I do not expect exact agreement of our computations with Yolcu et al. (2014) because (a) our inclusions are hexagonal in shape while those in Yolcu et al. (2014) are circular, (b) I use only the first few terms in the expansions provided in Yolcu et al. (2014) to fit our results, (c) our membrane is not infinite as in Yolcu et al. (2014) and has specific boundary conditions applied at its edges, and (d) the expansions in Yolcu et al. (2014) are valid, presumably, for $R/r << 1$, while for some of our computations $R/r < 1$.

4.2.2 Free energy maxima due to elastic entropic competition

Figure 4.3 shows that the elastic and entropic parts of the free energy have opposing trends as functions of r. This competition could result in a maximum in the total free

energy if the appropriate system parameters are chosen. To see this let's start with Eqn. (4.7):

$$U = U_{el} + U_{en} = \frac{a_{el} + a_{en}}{r^4} + \frac{b_{en}}{r^6} + \frac{c_{el} + c_{en}}{r^8} + O(\frac{1}{r^{10}}), \tag{4.8}$$

then, neglecting higher order terms I am able to compute the critical separation distance r_{cr} where the free energy U reaches a local maximum as:

$$r_{cr}^2 = \frac{-3b_{en} + \sqrt{9b_{en}^2 - 32\left(a_{el} + a_{en}\right)\left(c_{el} + c_{en}\right)}}{4\left(a_{el} + a_{en}\right)}. \tag{4.9}$$

For r_{cr} to be real, the right hand must be positive. If $a_{el} + a_{en} > 0$, then $c_{el} + c_{en} < 0$ will result in a maximum; if $a_{el} + a_{en} < 0$, then $b_{en} > \frac{4\sqrt{2}}{3}\left(a_{el} + a_{en}\right)\left(c_{el} + c_{en}\right)$ will result in a maximum. Now, from our fits, it is possible to find real values of r_{cr}. Generally, for most lipid bilayer membranes, the elastic contribution overwhelmingly dominates the entropic contribution and there is no maximum. However, for some special membranes with small bending rigidity, the entropic contribution can balance the elastic contribution and I can get a maximum. To test this idea, I chose lower bending moduli $K_b = 0.7 - 1.5k_BT$ (Group J-M in Table 4.1) and computed the free energy of our membrane with two inclusions of radius 2.5 nm at zero tension. Such low bending moduli are known to occur for surfactant membranes (see Rekvig et al. (2004) and references therein). In Figure 4.5(A) I plot the free energy $U(r)$ for two of these membranes and see a maximum in each case. The location of the maximum, r_{cr}, decreases with increasing K_b as I expect from Eqn. (4.9). Recall both from Yolcu et al. (2014) and our computation result in Table 4.1, that the coefficient a_{el} and c_{el} varies lienarly with K_b, while the coefficients a_{en}, b_{en}, and c_{en} are independent of K_b. Then, r_{cr} in Eqn. (4.9) should be related to K_b through

$$r_{cr} = \frac{\beta + \sqrt{\gamma - \mu K_b - \nu K_b^2}}{\alpha + K_b}, \tag{4.10}$$

where α, β, γ, μ, and ν are related to the protein size R and other system parameters. In our calculation, I cannot find the exact location of the maximum, r_{cr}, since I only choose the separation distances that are multiples of l, the element size. However, I am able to see the trend of r_{cr} increasing as the bending modulus of the membrane K_b decreases. I plot the result from our computation for the location of the maximum r_{cr} of Group J-M in Table 4.1 in an inset of Figure 4.5A. We see that the trend is consistent with prediction by
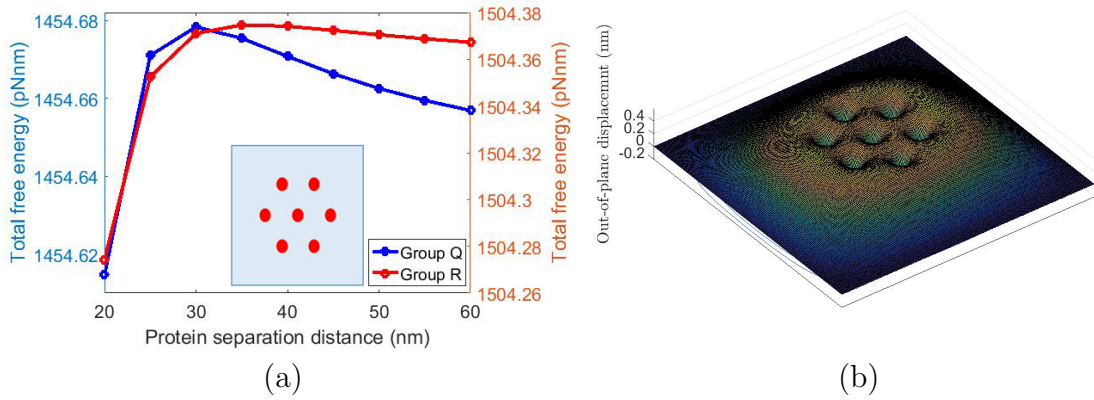
Figure 4.6: (a) Free energy profile of membrane inclusion system with parameters in Table 4.2. The blue line and green line are associated with left and right y-axis, respectively. (b) Out-of-plane deflection profile of a membrane with seven inclusions.

Eqn. (4.10).

4.2.3 Effect of tension on free energy maxima

While changing the bending modulus is one way of controlling the magnitude of elastic and entropic parts of the free energy, another way to do so is to change the hydrostatic tension. I have tried this for $K_b = 0.9k_BT$ by applying a tension $F = 1 \times 10^{-5}$ pN/nm to $F = 5 \times 10^{-3}$ pN/nm (Group N-P in Table 4.1). In Figure 4.5(B), I compare the computation result of total free energy of group N and P of same bending modulus K_b. The non-zero value of tension increases the elastic part of the free energy because the potential energy of the applied tension is added. It decreases the entropic contribution since tension stretches out the ripples of out-of-plane thermal fluctuation. The net result is that the location of the free energy maxima r_{cr} decreases with increasing F, and thus Figure 4.5A and B exhibit a similar result.

4.2.4 Protein cluster

Table 4.2: Parameters used in the protein cluster computations.

Group	L(nm)	Element size(nm)	K_b (pNnm)	Protein size(nm)	tension F (pNnm^{-1})	r_{cr} (nm)
Q	500	2.5	4.1	2.5	0	30
R	500	2.5	2.87	2.5	0	35
S	500	2.5	2.87	2.5	0.01	40

Having benchmarked our computations against analytic results I want to go beyond pair-wise interactions which are known not to apply to many-body interactions Kim et al. (1998). Our computational method is not restricted to just two inclusions; it can equally well be used to study interactions between many inclusions in a membrane. To illustrate the capability of our method I will assume that a cluster of seven inclusions forms a regular hexagon with one inclusion at each of the six vertices and one at the center as shown in the inset of Figure 4.6a. The side of the hexagon is r. Our choice of parameters for the membrane inclusion system is shown in Table 4.2. The out-of-plane deflection profile of a membrane protein system in group Q with a separation distance $r = 60$ nm is shown in Figure 4.6b. I compute the total free energy of the system as a function of r. I change both K_b and F in computation groups Q,R and S. For all groups I see a maximum in the free energy, as shown in Table 4.2 and plotted in Figure 4.6a. If $r < r_{cr}$ then these proteins will attract each other due to entropic interactions and r will decrease until a preferred separation is dictated by short range interactions. The value of r_{cr} can be modulated by changing the tension F. A more detailed analysis (including a parameter study) of such clusters of inclusions is left to future work, but the computations presented here suffice to illustrate the capabilities of our computational method.

Part II

Non-linear compression response of filament networks

Chapter 5

Compression of fibrin

Our goal in this chapter is to study the mechanical and structural responses of fibrin to compression by a combination of experiment and theory. In particular, from precise dynamic rheological and microscopic measurements I have developed a model for the compression behavior of fibrin networks based on the theory of foams and other cellular solids. First, the compression stress-strain curve was measured in experiment along with the loss and storage moduli at various strains with simultaneous three-dimensional visualization of the fibrin network during the deformation. In addition to the non-linear behavior of storage and loss moduli, I were able to reveal the non-uniformity of the compressive deformation with formation of a "compression front" or "phase boundary" along the axis of compressive strain (see Figure 1.3) Gaitanaros et al. (2012), Jang & Kyriakides (2009). Next, I described how the non-linear rheological behavior could be explained by viewing the fibrin network as a "cellular" solid that could exist in two phases – the low-strain phase in which the fibers are mostly straight, and a high-strain phase in which the fibers are mostly buckled. In displacement-controlled experiments such a solid has a stress plateau when there is a mixture of both phases. The fraction of each phase at equilibrium is determined by a lever rule Landau & Lifshitz (1986). However, the storage and loss moduli at various degrees of compression in our fibrin networks were obtained in the experiments by performing small oscillations around a certain strain. These oscillations changed the fractions of the two phases but they were not necessarily quasi-static. We treated these two phases using a continuum theory of phase transitions in which a kinetic equation relates the rate of change of the fraction of the phases to the stress Gibson & Ashby (1999). In this way I explained

the storage and loss moduli of the networks while accounting for the contributions of the moving phase boundary as well as the viscoelasticity of each phase.

In this chapter I first provide the details of the experimental procedures and present a description of the obtained data on controlled fibrin compression followed by a comprehensive theoretical analysis. After a short summary of the well-known results for cellular solids I show how this approach can be applied to fiber networks. I also describe the constitutive laws for fiber networks under large compression that have been studied using experiments and theory for several decades Van Wyk (1946), Toll (1998). I finally show how these results can be generalized and combined with a continuum theory for phase transitions to obtain the storage and loss moduli of networks under compression. The novelties of this work are (a) experimental visualization of a propagating phase boundary in compressed fibrin networks, (b) an explanation for the trends in storage and loss moduli of the compressed networks in terms of a theory of phase transitions, and (c) first application of foam theory to a bio-polymer network. Our analysis leads to some new experimentally testable predictions about the dependence of the mechanical properties of the clot on network parameters that have been summarized in the discussion section.

5.1 Compression-Induced Non-Uniformity of the Fibrin Network Structure

Visual examination of the fluorescent confocal images of the fibrin clots during compression revealed marked non-uniformity of the network structure. Here I define the XYZ-coordinate system as Z-axis along the vertical direction that is opposed to the applied compression. The XZ-plane sections of the fibrin networks clearly showed the appearance and progression of a gradient in the fluorescence intensity in the direction of compression with a more or less sharp boundary between the areas with different intensities (Figure 5.1). To precisely quantify the non-uniformity of the network density, I computationally reconstructed and analyzed the three dimensional images of a 150-μm-thick uncompressed fibrin clot and the same clot after 20% and 50% compression by segregating each image into 14 equal horizontal sublayers spanning the entire height of the network. The thickness of the red layers at various degrees of compression was different depending on the height of the

57
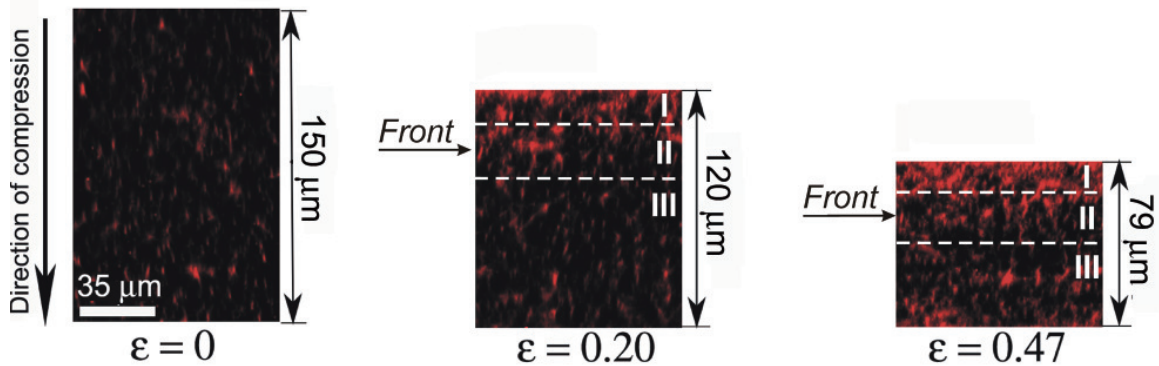
Figure 5.1: The "compression front" or "phase boundary" is formed in response to vertical deformation of a fibrin clot. To provide visual examination of the changing clot structure, the distribution of fluorescence intensity in the XZ plane is shown in the same fibrin clot, uncompressed (left), about 20% compressed (center), and about 50% compressed (right). As the degree of compression increases, the fluorescence intensity (reflecting the network density) displays a gradient along the direction of compression. Here the compressive strain ε is a degree of compression defined as $\varepsilon = |\Delta L/L_0|$, where $\Delta L = L - L_0$, and L_0 and L are the initial and reduced thickness dimensions of the uncompressed and compressed clots, respectively. The dashed lines outline the top (I), middle (II) and bottom (III) layers of the compressed clot, respectively. A horizontal arrow indicates the position of the compression front.

clot. I quantified the uniformity of network densification as the node density in each layer and plotted it against the distance from the bottom of the clot compressed from above (Figure 5.2). Our results showed that during vertical compression of a fibrin network a much higher degree of node densification was observed closer to the top of a clot, while the node and network density decreased towards the bottom. The top, middle and bottom layers of the compressed clots are indicated in Figure 5.1 and Figure 5.2. As the degree of compression increased from $\varepsilon = 0$ to $\varepsilon = 0.2$ and $\varepsilon = 0.47$, the node density of the upper network layers increased by a factor of 1.8 and 2.3, respectively. At the same degrees of compression ($\varepsilon = 0.2$ and $\varepsilon = 0.47$) the node density of the middle layers of the network increased by only 1.1 and 1.2, respectively. The density of the bottom portion of the network did not change at $\varepsilon = 0.2$, but increased by 1.2 for $\varepsilon = 0.47$ as is apparent from the diffuse region near the bottom of the clot in Figure 5.1 (right panel). However, this does not contradict the presence of a moving compression front from the top of the clot. Since the width of the front given by the parameter c in Eqn. (5.1) is about 30 μm and its center is located at $Z_0 = 42$ μm, the bottom portions of the network likely experience a non-zero strain that pushes them against the glass surface causing a moderate increase in fluorescence intensity.

58

To confirm the structural non-uniformities in fibrin clots produced by compressive loads, I also complemented the three-dimensional structural analysis of compressed fibrin networks with an experiment to follow the displacement of microscopic fluorescent beads embedded into the network in response to clot compression. 2-μm polystyrene fluorescent beads were tracked during the compressive deformation in a clot volume of $35.8 \times 35.8 \times 25.5 \mu$m in the bottom portion of the clot. The compression was applied in 25μm steps. After each step I waited 2 minutes before measuring the displacements of the beads. I found that the beads' position changed non-linearly in the Z-direction as a function of compressive strain (Figure 5.3), indicating the non-uniform compression of the network. In the case of spatially uniform compression, one would expect to observe a linear displacement of beads with compression irrespective of their initial position and the distance from the bottom of a clot. However, in our experiments the beads exhibited less than 20% relative displacements when the clot was exposed to compressive strains from $\varepsilon = 0$ to $\varepsilon = 0.6$, but revealed a rapid descent toward the bottom of the clot at $\varepsilon > 0.6$. To be more specific, when the compressive strain reached 0.6, the absolute distances changed by $2, 1.5$ and 0.6 μm for the beads initially located at $14.7, 11.1$ and 2.7 μm over the bottom, respectively. At a compressive strain of 0.7 the bead, which was the closest to the bottom of the clot, stopped moving because it had reached the surface. As the strain increased, other beads moved downwards until they also reached the bottom of the clot. The trajectory of all the beads turned downward at a similar compressive strain because they are all located within 15 μm of the bottom while compression is applied in 25 μm steps and the width of the front is about 30μm (see Figure 5.1 and Figure 5.2).The nonlinear response of bead displacement to network compression indicated that the deformation of the network occurred non-uniformly with the top layers being compressed earlier and stronger than the lower network portions. As a result, the beads did not undergo large displacements at low strains but their vertical position started to change drastically at about $\varepsilon > 0.6$ as the boundary between the relatively compact (upper) and loose (lower) portions of the network approached the bottom of the clot.

Thus, both the structural analysis and bead tracking provide evidence for the formation and propagation of a "compression front" inside the network as more dense upper layers overtake the less dense bottom portions of the fibrin clot during progressive compression.
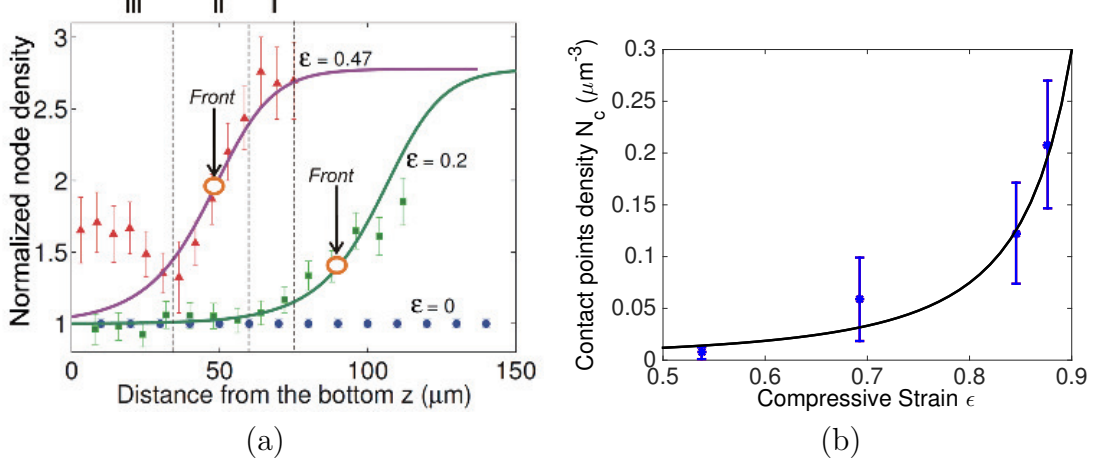
Figure 5.2: (a)The node density of the fibrin network as a function of height from the bottom of the sample based on three dimensional reconstruction of the network, uncompressed ($\varepsilon = 0$) and compressed to different degrees ($\varepsilon = 0.2$ and $\varepsilon = 0.47$). The node density was normalized with respect to the node density of the uncompressed clot. Note that the node density increases from bottom to top. The curve is flatter near the top and bottom of the sample and has a larger gradient near the middle. This suggests that the fibers are buckled near the top and straight near the bottom. The symbols represent experimental data (MSD, n=4) and I have modeled the regime of high gradient as a compression front or phase boundary. The lines represent fitting curves made using Eqns. (5.1) and (5.2) together with the experimental data with fitting parameters $a = b = 0.2$, $c = 30$ μm, and $Z_0 = 42$ μm for red curve, $Z_0 = 100$ μm for green curve respectively. Z_0 represents the center of the phase boundary in the reference configuration. The decrease of Z_0 shows that the front moves downwards in response to increased compression. The top (I), middle (II) and bottom (III) layers of the compressed clot ($\varepsilon = 0.47$) are separated by the vertical dashed lines that correspond to the layers shown in Figure 5.1. Large circles with vertical arrows indicate the position of the compression front. (b) Experimental data of node density under large compression is fitted by Eqn. (5.7). This justifies our use of Eqn. (5.8) for the densified network. I have used $l = 1.32$ μm, $d = 0.22$ μm, $\nu = 0.1$ μm^{-3}.

Such a front can be represented by a strain profile given as:

$$\varepsilon = a + b \tanh(\frac{Z - Z_0}{c}), \tag{5.1}$$

$$z(Z) = d + (1 - a)Z - bc \log\left(\cosh(\frac{Z - Z_0}{c})\right), \tag{5.2}$$

where Z is the original height of a material point in the unstressed (reference) configuration, Z_0 is the location of the center of the front in the unstressed configuration, and z is the deformed height that is measured in the experiment. I got Eqn. (5.2) by integrating
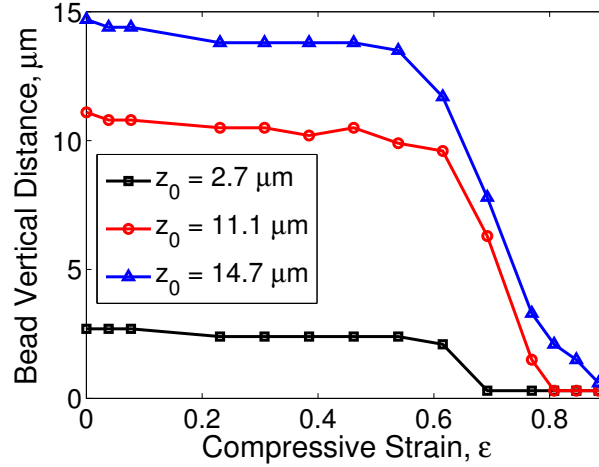
Figure 5.3: The absolute vertical distance from the bead to the bottom of the clot along the direction of network compression for various locations in the same clot compressed from $\varepsilon = 0 - 0.9$. The network is characterized by z - the bead distance from the bottom at a certain degree of compression and z_0 - the bead initial distance from the bottom of the network. $2\mu m$ polystyrene fluorescent beads were tracked during the compressive deformation in a clot volume of $35.8 \times 35.8 \times 25.5 \mu m$ in the bottom portion of the clot. Densification occurs at the bottom of the clot only at high compressive strain, likely coinciding with the arrival of the compression front at the bottom. Before the arrival of the compression front the density in the bottom of the clot remains almost independent of strain. This is what I expect in the plateau regime when the network consists of a mixture of two phases that accommodate the increasing compressive strain simply by advancing the compression front.

$dz/dZ = 1 - \varepsilon$ with boundary condition $z(0) = 0$, as in our experiments. Capital Z_0 cannot be measured in our experiment but using Eqn. (5.2) the change in Z_0 can be obtained from the experimentally measured changes in the location of the phase boundary as a function of z as explained below. The network density is proportional to $1/(1 - \varepsilon)$ as discussed in section 5.3. Thus, I can plot the network or node density as a function of z. Since the maximum values of the strain in Eqn. (5.1) are $a \pm b$, I expect that $2b$ should approximately equal the transformation strain or the difference in strains between the high-strain and low-strain phases at the plateau stress σ_0 a should be the strain at the center of the front, c should be a measure of the width of the front, and d is obtained by enforcing $z(0) = 0$ (see analysis in Appendix). Keeping this in mind I chose reasonable values of a, b and c to fit the experimental data. The data and the fits are shown in Figure 5.2. I found that $2b \approx 0.4$, as expected to be the transformation strain shown in Figure 5.2. Furthermore, Z_0 comes closer to the bottom of the sample when higher compression is applied, confirming that the "compression front" moves downward in response to the loading.

5.2 Non-linear Mechanical and Structural Response of Fibrin Networks to Compression

Structural alterations of fibrin network during compression underlie changes of shear viscoelasticity studied with rotational rheometry. The rheological measurements of fibrin clots with various initial shear storage and loss moduli were performed with two different compression steps (10 μm and 25 μm) and at different degrees of compression. The experimental results are shown in Figures 5.4 and 5.5 in combination with the theoretical curves. The normal stress, calculated as the force distributed over the area of the smaller rheometer plate was measured for each degree of compression, and presented as the plots of normal stress, σ, versus compressive strain, ε (Figure 5.4). The curves were almost linear at lower degrees of compression with a steep increase of the normal stress at higher degrees of compression ($\varepsilon > 0.5$). The evolution of the shear viscoelastic properties of fibrin networks in response to compressive deformation displayed a typical tri-phasic behavior (Figure 5.6). In the beginning of compression ($\varepsilon < 0.05$), the shear elastic modulus of a fibrin network was almost constant followed by a long relative plateau up to about $\varepsilon = 0.7 - 0.8$ compressive strain and finally dramatic increase at the highest compressive strains. The loss modulus followed the same trend (Figure 5.5b). If the current rheological measurements are correlated with the structural analysis of the network dynamics performed earlier in Kim et al. (2014), the results could be described as follows. First, a linear viscoelastic response to compression was observed, in which most fibers are straight. Then, a plateau regime follows, accompanied by an increasing number of buckled fibers while the stress remains nearly constant as strain increases. Finally, I see a regime in which network densification occurs with a stress-strain response that is markedly non-linear and dominated by bending of fibers after buckling and inter-fiber contact. In the next section we will quantify these observations using a model for foams. I emphasize that the experimental results reported here are substantially distinct from those reported earlier Kim et al. (2014) because in addition to the confirmed non-linear response, I were able to reveal the non-uniformity of the compressive deformation with formation of a "compression front" or "phase boundary" along the axis of compressive strain (see Figure 1.3a) Gaitanaros et al. (2012), Jang & Kyriakides (2009).

5.3   Short Review of Cellular Solids

A foam is a porous low density structure consisting of cells or fibers made of a viscoelastic material. In our case these fibers are made of fibrin. If E_s is Young's modulus of a single fibrin fiber, then the Young's modulus and shear modulus of the network or foam consisting of these fibers is given by Gibson & Ashby (1999):

$$E_1 = E_s \phi_0^2, \tag{5.3}$$

$$G_1 = \frac{3}{8} E_s \phi_0^2, \tag{5.4}$$

where the important non-dimensional quantity $\phi = \pi \nu d^2 l / 4$ is the volume fraction of fibrin in the network, ν, d, and l are respectively the number of fiber segments per unit volume, fiber diameter and fiber segment length between branch points. ϕ_0 is the initial fiber volume fraction before compression. These expressions are derived under the assumption of small strains so that the stress-strain relation of the foam can be approximated as linear. I will designate this phase of our fibrin network as the linear phase or the low-strain phase.

When this network is loaded in compression fibers will buckle Gibson & Ashby (1999) when a critical force is reached. From Euler's formula, the critical axial load that causes fiber buckling is

$$F_{cr} = \frac{n^2 \pi^2 E_s I}{l^2}, \tag{5.5}$$

where E_s, I and l are the Young's modulus, area moment of inertia, and the length of the fiber between branch points, respectively. The coefficient n is close to one and is determined by boundary conditions at the fiber ends. According to the analysis given in Gibson & Ashby (1999), n is taken to be 1 because the fiber lengh l varies over a range in random networks. I can use this expression for the critical load to estimate the stress σ_0 at which buckling of fibers begins in the network. According to Gibson & Ashby (1999), since, $\sigma_0 \propto F_{cr}/l^2 \propto E_s I / l^4$, I could write it as

$$\sigma_0 = c E_s \phi_0^2, \tag{5.6}$$

where the coefficient c is assumed to be 0.04 in Gibson & Ashby (1999). The strain corresponding to the critical stress in the low-strain phase is easily computed as $\varepsilon_1 = \sigma_0 / E_1$.

Another way to estimate ε_1 is to use Eqn. (5.5) – $\varepsilon_1 \approx F_{cr}/(AE_s)$ where A is fiber cross-sectional area. Both these methods give an estimate of ε_1 around 0.05 and σ_0 around 5 Pa for the parameters in the experiments shown in Figures 5.4 and 5.5. These ideas for estimating σ_0 can only be justified if the fibers in the network are not undulating due to thermal motion. The extent of thermal undulations depends on the persistence length of the fibers and their length between branch-points. The persistence length of fibrin varies over a wide range depending on the conditions (thrombin concentration, pH, calcium concentration, etc.,Ryan et al. (1999)) under which a clot is made Sharma et al. (2008), Jahnel et al. (2008). In fact, Piechocka et al. (2010) summarizes several reasons in addition to fibrin assembly conditions (such as, protein packing density, lateral binding between protofibrils. etc.) that result in the variation of fibrin persistence length. For our fibrin networks, which have been derived from plasma clots, the average diameter of the fibers is about 220nm Kim et al. (2016), which together with a Young's modulus $E = 5$MPa Collet et al. (2005) gives a persistence length EI/k_BT at room temperature about 1m. The length l between branch points is about $1-2\mu$m, on average. Thus, thermal fluctuations of the fibers are negligible, consistent with the assumption for foams.

When large compressive strain is applied to a fibrin network the total volume decreases considerably and the inter-fiber space is reduced. In this configuration a linear stress-strain relation is not applicable any more. The fibers are mostly buckled and forced to touch each other. I call this kind of configuration the "densified phase" or the high-strain phase. This sort of densified network has been studied by Toll Toll (1998) who showed that the number of contact points N_c per unit volume is an increasing function of fiber volume fraction ϕ and was given by

$$N_c = \frac{16}{\pi^2} \frac{f}{d^3} \phi^2, \tag{5.7}$$

where f is a scalar invariant of the fiber orientation distribution function and is equal to $\pi/4$ for three dimensional isotropic networks Toll (1998). Following Gibson & Ashby (1999), in the densified phase I assume the fiber volume fraction $\phi = \phi_0/(1-\varepsilon)$. In other words, all the volume change is due to the reduction in the thickness of the network in the direction of the compressive force with no change in the cross-sectional area. Our experiments indicate that this is a good approximation. I compared Eqn. (5.7) to the experimental data on contact point density N_c from Kim et al. (2014) and found that it indeed varied quadratically with

the fiber volume fraction ϕ as shown in Figure 5.2b. The stress-strain relation for such a network was proposed by van-Wyk Van Wyk (1946) and Toll Toll (1998) in the following form:

$$\sigma = kE_s \left(\phi^n - \phi_0^n \right), \tag{5.8}$$

where the coefficient k is determined by the material and loading conditions. It is found to be less than 1, as in Mezeix et al. (2009). The exponent n was analytically derived to be 3 from Eqn. (5.7) for three-dimensional random networks in Toll (1998). This has been confirmed by several experiments Mezeix et al. (2009), Choong et al. (2013), Bouaziz et al. (2013), Masse & Poquillon (2013). From Eqn. (5.8), I can compute the local tangent moduli of the network in the densified regime. The tangent modulus at any strain in the densified regime is directly proportional to the storage modulus in the rotational rheometer oscillation experiments. Following the linear theory for foams at small strains I assume that the ratio between this storage modulus and the local tangent modulus in the densified regime is 3/8 (see Eqns. (5.3) and (5.4)) and get the following expression for the shear modulus of the densified network at strain ε:.

$$G = \frac{9kE\phi_0^3}{8 \left(1 - \varepsilon \right)^4}. \tag{5.9}$$

Any contributions due to the Poisson effect in the densified regime are absorbed into the constant k that has been treated as a fitting parameter in the literature. This is also consistent with our experimentally motivated assumption above that vertical compression of the fibrin network does not change its cross-sectional area. For the plateau stress $\sigma = \sigma_0$, I find that the Young's and shear moduli are

$$E_2 = \frac{3kE\phi_0^3}{\left(1 - \varepsilon_2 \right)^4}, \tag{5.10}$$

$$G_2 = \frac{9kE\phi_0^3}{8 \left(1 - \varepsilon_2 \right)^4}, \tag{5.11}$$

where ε_2 is the strain at which $\sigma_0 = kE_s \left(\phi^3 - \phi_0^3 \right)$.

We will use a linearized version of the stress-strain relations (in the neighborhood of $\sigma = \sigma_0$) in our subsequent analysis. These are summarized for the low- and high-strain

phases as follows.

$$\varepsilon\left(\sigma\right) = \begin{cases} \sigma/E_1 & \sigma \le \sigma_0 \, (\varepsilon < \varepsilon_1) \\ \sigma/E_2 + \varepsilon_T & \sigma \ge \sigma_0 \, (\varepsilon > \varepsilon_2) \end{cases} \qquad (5.12)$$

where σ_0 is the critical stress for buckling, as discussed previously. At this stress the straight and densified phases co-exist. E_1, E_2 are Young's moduli in the straight and densified phases respectively from Eqns (5.3) and (5.10). ε_T is the transformation strain which can be estimated by constructing the tangent to the stress-strain curve at $\varepsilon = \varepsilon_2$ and reading off the intercept on the ε axis. If I assume that the process of loading is quasi-static so that the sample stays in equilibrium during the compression process, then the compressive strain ε in the plateau corresponding to the stress σ_0 is obtained simply by changing the fraction of fibers buckled. If I denote the fraction of fibrin in the high strain phase as $s \in [0, 1]$, then total strain can be estimated from the insight that the sample consists of two 'springs' in series consisting of the straight and densified network respectively as observed in Figure 5.2.

$$\varepsilon = (1 - s)\frac{\sigma}{E_1} + s\left(\frac{\sigma}{E_2} + \varepsilon_T\right). \qquad (5.13)$$

This completes the description of the stress-strain curve for a fibrin network under compression. As an example I have plotted this stress-strain curve for a fibrin network with network parameters experimentally measured in Kim et al. (2014) in Figure 1.3b. I have used values of the fiber Young's modulus $E_s = 5$ MPa Brown et al. (2009), Purohit et al. (2011), Collet et al. (2005). The stresses in Figure 1.3b are of the same magnitude as the measured storage moduli in Figure 5.5. However, the stress strain curve in Figure 5.4 does not have an initial linear regime for small strains even though it seems to have a flat plateau regime for intermediate strains and a regime with steeply increasing stress for high strains. Furthermore, the shear moduli measured in Figure 5.5 are at least three orders of magnitude lower than those seen in the normal stress data plotted in Figure 5.4. This indicates that Figure 5.4 is not a true reflection of the stress strain response of the network; rather it is the result of water squeezing out of the network in response to compression. To understand why this is the case I must account for the strain-rate dependence of the mechanical response of these fibrin gels.

5.4 Strain Rate Dependence

The fibrin networks that have been tested in our experiments really are gels that contain a large amount of water. As the gel is compressed, water is squeezed out. However, as it is sheared, water is not squeezed out because the total volume does not change. Hence, it is expected that the measured normal stresses in compression will depend on the applied strain rates. This effect is well-known as poro-viscoelasticity in foams and other cellular solids Gibson & Ashby (1999). An analytic relation for the stress as a function of the applied strain rate is given as Gibson & Ashby (1999)

$$\sigma = \frac{C\mu\dot{\varepsilon}}{1-\varepsilon}\left(\frac{D}{l}\right)^2, \tag{5.14}$$

where μ is dynamic viscosity of the fluid, ε and $\dot{\varepsilon}$ are the compressive strain and its rate, D is horizontal dimension of the foam sample, and l is the cell edge-length of the foam. The coefficient C is about unity. As shown in Figure 5.4, the measured normal stress during compression can be captured by Eqn. (5.14) with the parameters $\mu = 0.001$ Pa·s (for water), $D = 22$ mm (known from our experimental set-up) and l as the only fitting parameter for each experiment. The strain rate for each experiment is different because the height of the samples varies while the rate of compression (30μ m/s, see section 2.3) remains fixed for each experiment. The fitted values of l appear in Table 5.1. They are within the range of variation of fiber lengths between branch points seen in experiments Kim et al. (2014). I see that most of the normal stress measured in the experiments is due to the expulsion of water from the fibrin gel. Hence, the storage and loss moduli measured in our rheometer experiments and shown in Figure 5.5 cannot be extracted from the stress-strain curves shown in Figure 5.4.

From Eqn (5.14), I can approximate the viscosity of the gel for small strains (infinitesimal values of ε) as

$$\eta \propto \mu\left(\frac{D}{l}\right)^2 \tag{5.15}$$

However, the viscous losses due to this term cannot be measured in the rotational rheometer experiments because the derivation of this expression assumes that the volume of the network is changing while the oscillatory experiments are performed in shear which involves no change in volume. Therefore, the loss modulus in the low strain phase should only come

Table 5.1: Fitting parameters for each experiment of fibrin.

Individual group	Sample height(mm)	strain rate(s^{-1})	Fiber length(μm)
Black circle	550	0.055	0.5
Magenta triangle	650	0.046	0.3
Black diamond	650	0.046	0.27
Blue circle	750	0.04	0.5
Green diamond	650	0.046	0.4
Red square	750	0.04	0.3

Individual group	ϕ_0	k	ε_{20}	M (Pa^{-1}s^{-1})	$w\tau_{on}(10^{-18}$J $\cdot$ s)
Black circle	0.0045	0.025	0.82	0.004	2
Magenta triangle	0.0045	0.0025	0.8	0.005	1.2
Black diamond	0.0035	0.0025	0.85	0.008	1.7
Blue circle	0.0035	0.333	0.7	0.008	4
Green diamond	0.004	0.333	0.6	0.008	6.5
Red square			Densification not observerd		

from the liquid viscosity itself. For water, this is merely $\mu = 0.001$ Pa·s, which is much smaller than the value obtained from (5.15). Therefore, I treat the fibrin network in the low strain phase as a purely elastic solid with constant modulus.

Another important network property that is related to the strain rate is the inter-fiber friction. This is particularly important in the densified phase in which a large number of contacts are created between fibers. Fibers sliding against each other while in contact will cause dissipation in the network. In order to estimate the viscosity associated with this process I appeal to an elegant calculation in Howard et al. (2001). This book gives an explanation for the molecular basis of "viscosity" due to the forming and breaking of bonds as molecules slide past each other. The expression is:

$$\eta = wN_c\tau_{on}, \tag{5.16}$$

where w is the inter-molecular bond energy and τ_{on} the average life-time of a bond. An expression for N_c as a function of fibrin volume fraction is already given in Eqn. (5.7). However, w and τ_{on} are difficult to determine for fibrin fibers. Some work along this direction has been done for estimating the viscous losses in microtubule networks Yang et al. (2013), but here I treat the product $w\tau_{on}$ as a fitting parameter. In summary, I model the densified network at $\sigma = \sigma_0$ (for small strains) as a Kelvin-Voigt solid Fung (1965) in

which the stress-strain relation is given as:

$$\sigma = E_2(\varepsilon - \varepsilon_T) + \eta\dot{\varepsilon}, \tag{5.17}$$

where the parameters E_2 and η are taken from Eqns (5.10) and (5.16). In the rotational rheometer experiments the loss modulus is related to this viscosity as:

$$G'' = \eta\omega, \tag{5.18}$$

where ω is frequency of oscillation. The loss modulus for both the low- and high-strain phases can be determined using this formula if I use $\eta = \mu = 0.001\text{Pa·s}$ (of water) for the low-strain phase and Eqn.(5.16) for the high-strain phase. In order to estimate the loss modulus in the plateau regime of the stress-strain curve I need to account for the rate at which the fractions of the two phases evolve. This is explained in the next section.

5.5   Phase Boundary Mobility

In the oscillation experiments, the fraction of each phase depends on both applied strain and strain rate. As shown in Figure 1.3a, the phase boundary is expected to oscillate as the applied loading oscillates. I treat this process in a one-dimensional model as follows. After pre-compressing the sample, I assume that the oscillation is also in the axial direction. This is different from the experiments in which an oscillating shear strain is applied on the pre-compressed networks. However, since the oscillating shear strains applied in the experiments are small, I can assume that they will give storage and loss moduli that are proportional to those obtained in our calculations.

During the oscillation process the sample may not be in equilibrium and thus the stress may not be σ_0. There will be oscillation in stress, phase fractions, as well as strain. I assume that the fraction s is determined by the kinetics of transformation as in Abeyaratne & Knowles (2006). This means that the rate of change of each fraction is given as a function of stress σ. To simplify the problem I consider the particular kinetic equation Raj & Purohit (2011):

$$\dot{s} = \Phi(\sigma) = M(\sigma - \sigma_0), \tag{5.19}$$
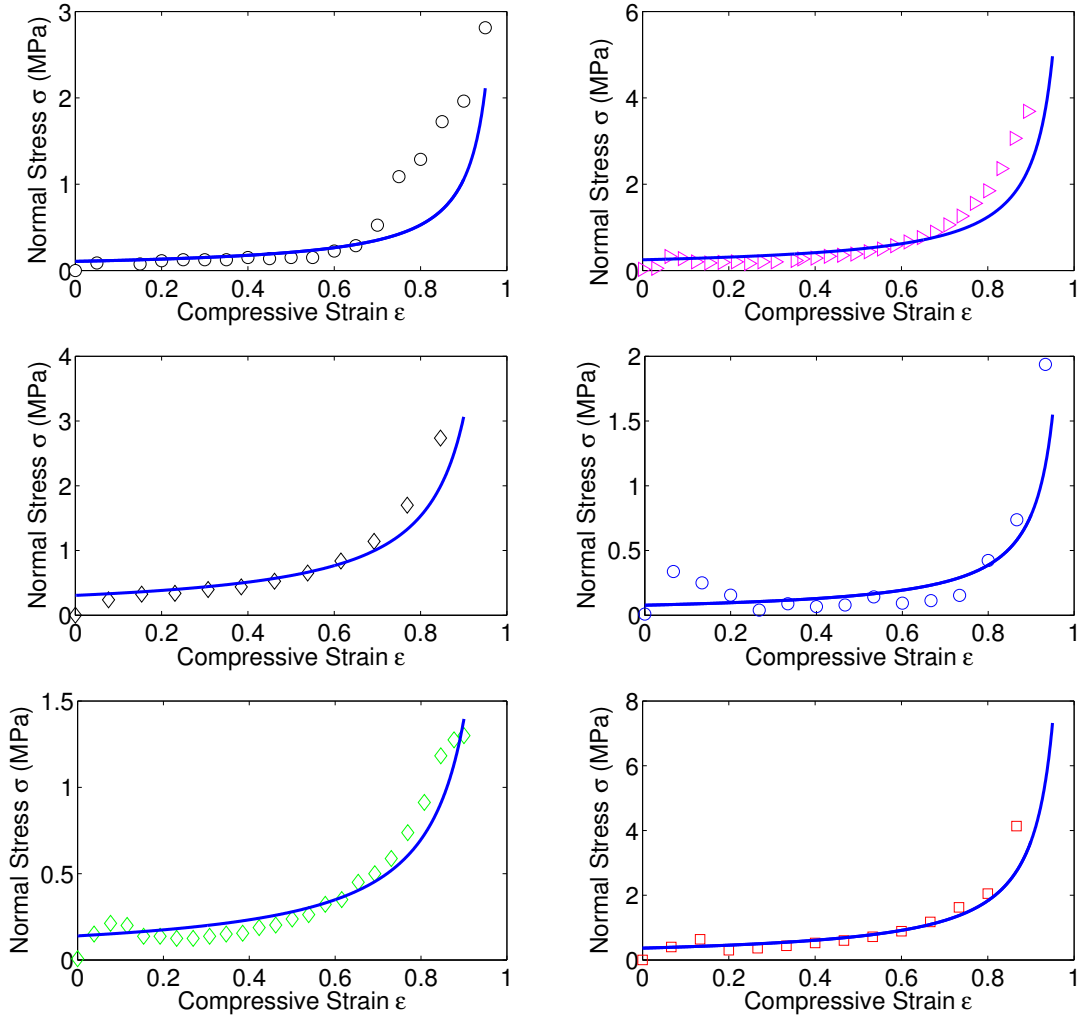
Figure 5.4: Fitting of the experimental data of normal stress according to Eqn. (5.14). Different symbols and colors are experimental data corresponding to different clot samples of varying height as shown in Table 5.1. Since the rate at which they are compressed is 30μm/s for all samples the strain rate for each of them is different. Lines show model fits with parameters as given in Table 5.1. Most of the normal stress measured in the compression experiments on our fibrin gels is due to the escape of water in response to compression. For this reason I cannot extract the storage and loss modulus of the networks from these stress-strain curves.

or,

$$s - s_0 = \int_0^t M(\sigma - \sigma_0)\mathrm{d}t = M\int_0^t (\sigma - \sigma_0)\mathrm{d}t, \tag{5.20}$$

where M is a time-independent mobility parameter determined by the network that could be regarded as a fitting parameter in our theory and s_0 is the fraction of high strain phase before oscillation is applied. In the experiment I apply a harmonic oscillating strain to the
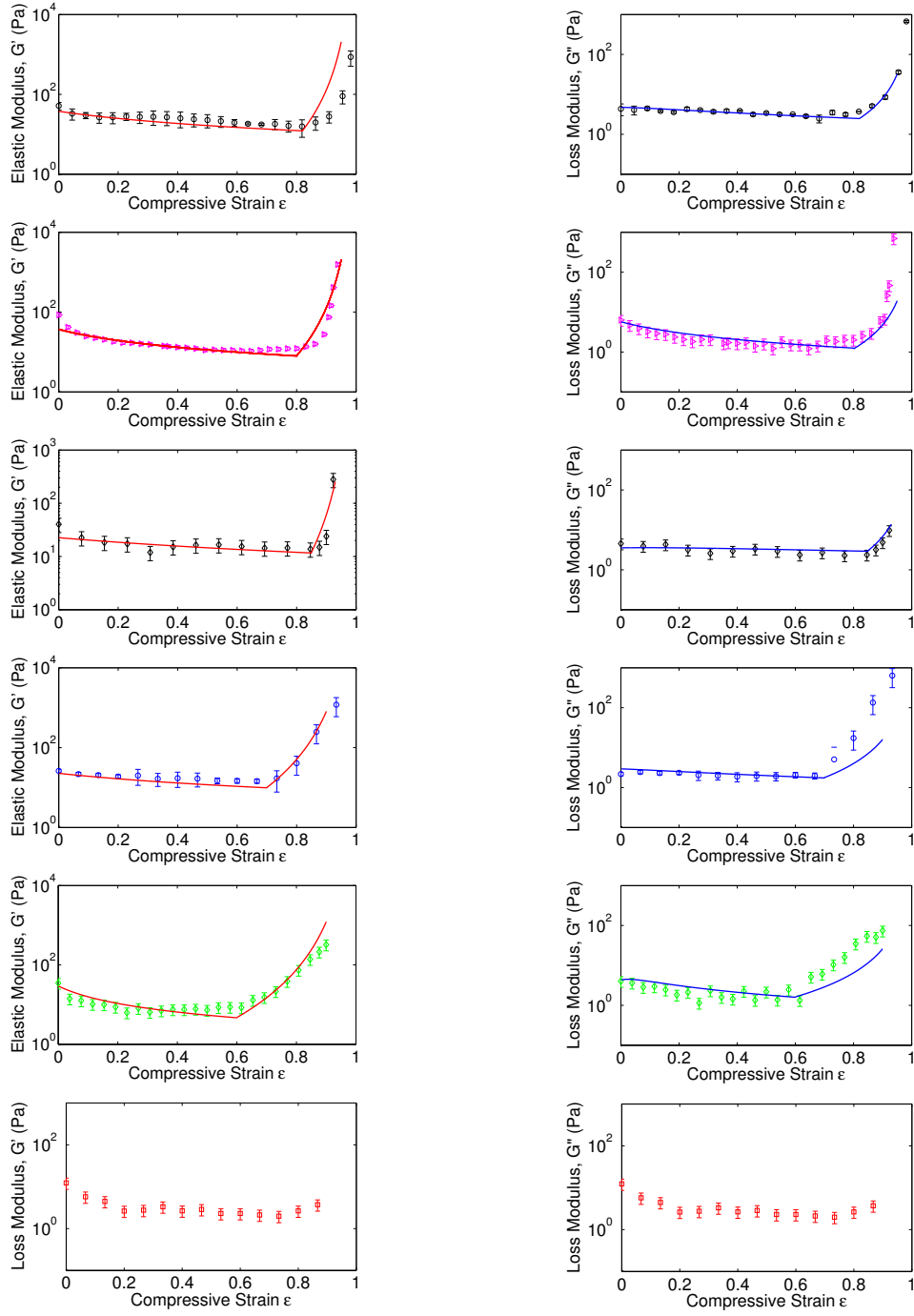
Figure 5.5: Fitting of the storage moduli and loss moduli according to Eqns. (5.4), (5.9), (5.32), (5.16), (5.18), and (5.32). I have used fitting parameters for each individual experimental group as given in Table 5.1. Note that there is no densification regime in the last group. One possible reason could be the failure or damage of the network under large compression. However, the data for strains smaller than 0.8 in the last group are consistent with the other data sets.
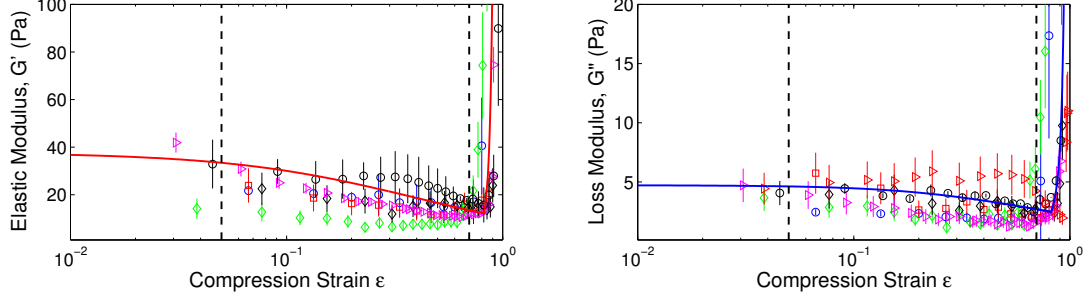
Figure 5.6: Experimental data of storage moduli and loss moduli versus logarithm of strain, showing three different regimes of fibrin network mechanics as indicated schematically in Figure 1.3. In the linear regime($0 < \varepsilon < 0.05$), the moduli are constant; in the phase transition regime($0.05 < \varepsilon < 0.7$), they are decreasing due to progressive fiber buckling; in the desification regime ($0.7 < \varepsilon < 1$), they are steeply increasing due to bending of the buckled fibers and increased inter-fiber contact. The theoretical curves passing through the experimental data are plotted using Eqns. (5.4), (5.9), (5.32), (5.16), (5.18), and (5.32) with $\phi_0 = 0.0045$, $k = 0.025$, $\varepsilon_{20} = 0.7$, $M = 0.004\text{Pa}^{-1}\text{s}^{-1}$, $\omega\tau_{on} = 2 \times 10^{-18}\text{J} \cdot \text{s}$.

pre-compressed network as:

$$\varepsilon = \varepsilon_0 + a \sin \omega t, \tag{5.21}$$

where ε_0 is an initial strain in the plateau regime of phase transition before oscillation is applied. Taking account of the strain rate dependence I rewrite Eqn. (5.13) as:

$$\varepsilon = (1-s)\varepsilon_1 + s\varepsilon_2,$$
$$\sigma = E_1\varepsilon_1 = E_2(\varepsilon_2 - \varepsilon_T) + \eta\dot{\varepsilon}_2. \tag{5.22}$$

Now, recall that the expression for equilibrium stress σ_0 and strain ε_0 are given by:

$$\varepsilon_0 = (1-s_0)\varepsilon_{10} + s_0\varepsilon_{20},$$
$$\sigma_0 = E_1\varepsilon_{10} = E_2(\varepsilon_{20} - \varepsilon_T). \tag{5.23}$$

where the subscript 0 denotes the quantity in initial compression equilibrium before oscillation. Subtracting Eqns. (5.23) from (5.22) I get:

$$a \sin \omega t = (1-s_0)x + s_0 y + (s - s_0)(\varepsilon_2 - \varepsilon_1), \tag{5.24}$$

$$\sigma - \sigma_0 = E_1 x = E_2 y + \eta\dot{y}, \tag{5.25}$$

where $x = \varepsilon_1 - \varepsilon_{10}$ and $y = \varepsilon_2 - \varepsilon_{20}$ are the small oscillating components of strain in each

72

phase. Since the oscillation in strain is small, I make an approximation in Eqn. (5.24) by replacing $\varepsilon_2 - \varepsilon_1$ with $\varepsilon_{20} - \varepsilon_{10}$. Then, plugging Eqn. (5.20) and (5.25) in (5.24) I get:

$$
\begin{aligned}
a \sin \omega t = (1 - s_0) \frac{E_2 y + \eta \dot{y}}{E_1} + s_0 y \\
+ M(\varepsilon_{20} - \varepsilon_{10}) \int_0^t (E_2 y + \eta \dot{y}) \mathrm{d}t.
\end{aligned}
\tag{5.26}
$$

Carrying out the integral of $\dot{y}$ and rearranging terms, I find that

$$
a \sin \omega t = Ay + B\dot{y} + C \int_0^t y \mathrm{d}t,
\tag{5.27}
$$

where the three dimensionless quantities A, B, and C are given by:

$$
\begin{aligned}
A &= (1 - s_0) \frac{E_2}{E_1} + s_0 + M\eta(\varepsilon_{20} - \varepsilon_{10}), \\
B &= (1 - s_0) \frac{\eta}{E_1}, \\
C &= ME_2(\varepsilon_{20} - \varepsilon_{10}).
\end{aligned}
\tag{5.28}
$$

Let us assume that this equation has the solution:

$$
y = U \sin \omega t + V \cos \omega t,
\tag{5.29}
$$

where U and V are at present unknown. Plugging this into Eqn. (5.27) and solving for the two coefficients U and V gives:

$$
\begin{aligned}
U &= a \frac{A}{A^2 + (B\omega - C/\omega)^2}, \\
V &= -a \frac{B\omega - C/\omega}{A^2 + (B\omega - C/\omega)^2}.
\end{aligned}
\tag{5.30}
$$

Plugging this back into Eqn. (5.22) I get the expression for stress as:

$$
\begin{aligned}
\sigma &= \sigma_0 + E_2 y + \eta \dot{y} \\
&= \sigma_0 + a(E_2 U - \eta V \omega) \sin \omega t + a(E_2 V + \eta U \omega) \cos \omega t.
\end{aligned}
\tag{5.31}
$$

Therefore, the storage and loss modulus in the plateau regime (i.e. $\sigma = \sigma_0$) are respectively

$$
\begin{aligned}
G' &= E_2 U - \eta V \omega = \frac{E_2 A + \eta B \omega^2 - \eta C}{A^2 + (B\omega - C/\omega)^2}, \\
G'' &= E_2 V + \eta U \omega = \frac{-E_2 (B\omega - C/\omega) + \eta A \omega}{A^2 + (B\omega - C/\omega)^2}.
\end{aligned}
\tag{5.32}
$$

In order to confirm that the above framework predicts the correct storage and loss moduli, I compared quantitatively our theory with the experimental data. The input parameters of the network in the above computations were taken from the experiments shown in Figure 5.5. Combining Eqns. (5.4), (5.9) and (5.32) together, I obtain the theoretical curve in each individual experiment in Figure 5.5. I take the value of branch point density and fiber density exactly as measured in experiment as 0.04 μm^{-3} and 0.1 μm^{-3} respectively. The other fitting parameters for each experiment are reported in Table 5.1. The trends in storage and loss moduli are captured quite well with this model. Note that the experimentally measured average fiber length and average fiber diameter are 1.32 μm and 220 nm respectively Kim et al. (2014), which result in a fiber volume fraction of $\phi_0 = \pi \nu d^2 l / 4 = 0.005$. The ϕ_0 values obtained by our fits are slightly below this value but well within the range of variation of ϕ_0 in the experiments Kim et al. (2014). Also note that the value of constant k in the densifed phase varies inversely with the strain ε_{20} where the phase transition finished. I have not yet been able to rationalize this.

We will now connect our results for the variation in moduli to Figure 1.3 which schematically shows three distinct regimes in the stress-strain curve. To this end I have replotted all the data for storage and loss moduli in Figure 5.6 against the logarithm of the strain ε. The red and blue curves in the upper and lower panels are fits to the average of all the storage and loss moduli, respectively. The strains ε_1 and ε_2 have been indicated by dashed lines to demarcate the three regimes. In the initial linear regime, $\varepsilon < \varepsilon_1$, the moduli G' and G'' are constant. In the plateau regime, $\varepsilon_1 \leq \varepsilon \leq \varepsilon_2$ the network accommodates more strain by changing the fractions of the straight and densified phases of the networks through the motion of the phase boundary. G' decreases with increasing strain in the plateau regime because the slope of the stress-strain curve of the densified phase at $\varepsilon = \varepsilon_2$ is smaller than the slope for the straight phase at $\varepsilon = \varepsilon_1$. For $\varepsilon > \varepsilon_2$ densification occurs and both moduli increase steeply.

74

Chapter 6

Compression of PPP, PRP and whole blood clots

Most studies of clot mechanics and all studies of compression of clots have been carried out using clots made only of fibrin Kim et al. (2016). However, the fibrin network is only a part of the blood clots formed *in vivo* at sites of vascular injuries to prevent blood loss. These clots also contain varying amounts of platelets, red blood cells (RBCs), other cells and plasma proteins. Furthermore, such blood clots formed in a vessel are subject to external and internal mechanical forces. Internal mechanical forces are generated in the vasculature by blood flow, created by cardiac contraction producing the hydrostatic force of the blood within the vessel. There is also internal mechanical deformation generated by platelets pulling on fibrin in clot contraction (retraction). External forces are created as a result of vessel wall contraction, cardiac muscle and striated muscles adjacent to the blood vessels, especially in veins of the lower limbs. Thus, there are multiple forces acting on blood clots, including shear, tensile, and compressive forces.

There are only a few studies of the effects of platelets on clot mechanical properties, although they affect fibrin structure Gersh et al. (2009). It is likely that platelets pulling on fibrin induce the fibers to go beyond the low strain linear viscoelastic limit and exhibit strain stiffening Burstein & Lewi (1952), Shah & Janmey (1997). Since much thrombin is generated on the platelet surface, many fibrin fibers originate from platelets or platelet aggregates, affecting the overall structure of the clots Collet et al. (2005).

Similarly, not much is known about the effects of RBCs on clot mechanical properties.

Although they have long been viewed as passive participants in clotting, there is increasing evidence that they play a more active role Gersh et al. (2009). For example, in clot contraction, RBCs are compressed to form a tightly packed array of polyhedral cells, which forms a very tight seal that is largely impermeable Cines et al. (2014). Thus, it is very important to understand how these various components of the clot, the fibrin network, RBCs and platelets, interact with each other in response to deformation. This knowledge can be important for understanding how blood clots and thrombi respond to mechanical forces *in vivo*. In addition, fibrin is increasingly being used as a biomaterial, including with composite materials and various cells, so its responses to compression are also important in this context.

Here, I investigate the mechanical response of human whole blood clots, platelet-rich plasma (PRP) clots, and platelet-poor plasma (PPP) clots, to cycles of compression and decompression, and correlate the effects with structural changes in all the components (see also Franck et al. (2007), Maskarinec et al. (2009)). These mechanical responses show unique characteristics that were unexpected, but can be interpreted in terms of a continuum phase transition model. In addition, I also investigate the viscoelastic properties of the clots and how they change with compression/decompression and a structural basis of these properties.

6.1 Materials and Methods

6.1.1 Materials

Whole blood from healthy volunteers was collected according to an IRB protocol at the University of Pennsylvania with informed consent. The blood was collected into 12 mM sodium citrate (final concentration) as an anticoagulant, and then centrifuged at 130 g for 15 min to obtain PRP, which was again centrifuged at $10,000$ g for 15 min to obtain PPP. Clots were made by adding $CaCl_2$ (25 mM final concentration) and 1 U/mL (final concentration) human α-thrombin (American Diagnostica Inc. Stamford, CT USA). Clots of 600 μm thick were formed at 37 °C directly between the rheometer plates (ARG2; TA Instruments, New Castle, DE) for all whole blood, PRP and PPP clots.
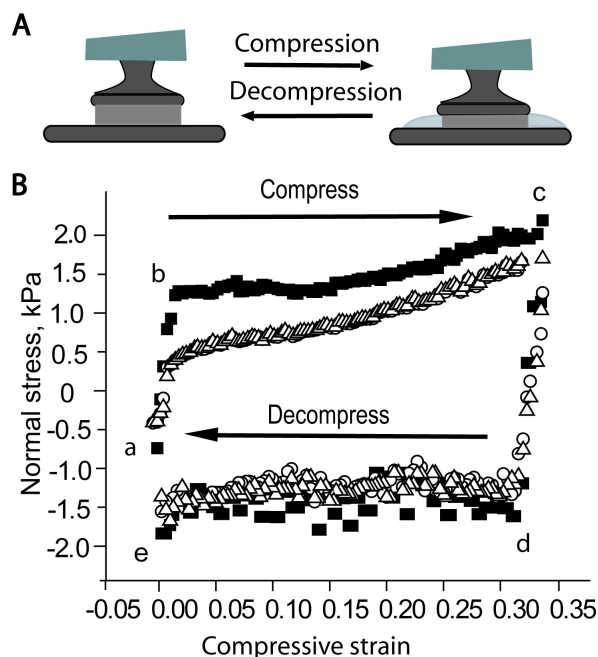
Figure 6.1: Experimental set-up to obtain rheological data for compression and decompression of clots and typical stress-strain curves for compression-decompression cycling. (A) Schematic illustration of compression and decompression of a clot formed between the rheometer plates. The dark gray shapes represent the top and bottom plates of the rheometer, while the light gray shape represents the clot and the serum expelled from the clot. The clot was compressed as the upper rheometer plate moved down, squeezing serum out of the clot. When the maximum compressive strain was achieved, the upper plate was moved back up to its original position at the same rate to forcefully decompress the clot. The serum was pulled back into the clot. Three cycles of compression and decompression were performed on the same clot. (B) An example of stress-strain curves obtained by measuring the normal stress during compression and decompression cycles, as shown in (A). The symbols of squares, triangles and circles represent the first, second, and third cycle, respectively. (a) Starting point with no compression; (b) first inflection point in the compression of the clot; (c) point at which clot is fully compressed and the start of decompression; (d) first inflection point in the decompression of clot; (e) second inflection point in the decompression cycle. (a) end point of decompression cycle. Compressive stresses and strains are assumed to have a positive sign (opposite of convention in which tensile stresses and strains are positive). Note that during the decompressive part of the cycle (c,d,e) tensile forces must be applied to return the clot to its original thickness.

6.1.2 Experimental methods

Compression experiments

Clots were compressed continuously at the rates of 10 or 100 μm/s, as the upper rheometer plate moved down to exert an axial force on the upper surface of the clot. When the maximum compressive strain was achieved, the upper plate was moved back to its original

position at the same rate to forcefully decompress the clot. Three cycles of compression and decompression were performed on the same clot. The clots were compressed and decompressed vertically up to 2/3 or 1/2 of their initial thickness, i.e., compression of 1.5X or 2X. The compressive strain (degree of compression) was defined as the absolute fractional change in fibrin clot thickness $\varepsilon = |\Delta h/h_0|$, where $\Delta h = h - h_0$, and h_0 and h are the thickness dimensions of the uncompressed and compressed clots, respectively. During compression and decompression, the normal stress was measured and stress-strain curves were plotted for further analysis. Also, changes of viscoelastic properties of clots during compression and decompression were measured at various points of the compression-decompression cycles with constant oscillatory strain of 3.3% at a frequency of 1.5 Hz to produce a linear shear stress response to imposed shear strain. The elastic response in shear of the clot was characterized by the shear storage modulus, G', representing the stored energy and defined as $G' = (\sigma_0/\gamma_0)\cos(\delta)$. The viscous response was measured by the shear loss modulus, G'', calculated as the out-of-phase part of the stress as $G'' = (\sigma_0/\gamma_0)\sin(\delta)$, corresponding to the energy dissipated as heat. Here, σ_0 is the amplitude of the oscillatory stress, γ_0 is the amplitude of the oscillatory strain, and δ is the phase difference between the stress and strain sinusoids.

Scanning electron microscopy

Clots (whole blood, PRP and PPP) that were used in rheometry experiments were fixed in 2% glutaraldehyde in 0.1 M cacodylate buffer, pH 7.4, dehydrated with ethanol, dried with 50% and finally with 100% hexamethyldisilazane (Acros Organics, Fair Lawn, NJ), and sputter-coated with gold-palladium as described in Vorjohann et al. (2010). The samples were examined and images saved in an FEI Quanta 250FEG scanning electron microscope (FEI, Hillsboro, OR).

Confocal microscopy

Clots were formed as described above for rheometry measurements, except that 0.06 mg/ml Alexa 488 labeled fibrinogen (Invitrogen, Carlsbad, CA, USA) was added to the clots plasma before clot formation. For whole blood clots, 25% of RBCs within each clot were stained with DiD (Molecular Probes by Life Technologies, Eugene, OR, USA) far red fluorescent dye which was incorporated into the RBC membrane. To stain RBC, whole

blood was centrifuged at 160 g, supernatant (plasma) was aspirated, 25% of volume RBC were taken from a tube and stained with DiD. After staining was completed, stained and unstained RBC were mixed and added back to plasma .

Clots were formed in a customized chamber built between two coverslips separated by plastic putty, which maintains compression of the clot within the chamber when it is compressed between the rheometer plates. The chambers were transferred to the stage of the microscope and images were collected using a Zeiss LSM 710 confocal microscope (Zeiss, Oberkochen, Germany) with a 63-X oil immersion 1.4 NA Plan Apo objective lens. Passively decompressed clots were also imaged by removing the putty and allowing the clots to relax. 3D reconstructions of z-sections were computed by using Volocity software (Perkin-Elmer Co, Waltham, MA USA).

6.1.3   Theoretical methods

Compression of PPP and PRP clots

It has been demonstrated earlier that fibrin can be viewed as a foam with fluid in its pores because of its low density isotropic network structure Kim et al. (2016). As described in Figure 6.2 and Section 6.2.7, observation of network structure reveals a transition from a rarefied phase to a densified phase under compression. In Kim et al. (2016) I had demonstrated that the transition proceeds by the propagation of an interface through the sample that separates the rarefied and densified phases. In the rarefied phase, fibrin fibers are mostly straight and the whole network has a linear response under compression with a Young's modulus E_L that depends on the network density and fiber mechanical properties as described in Gibson & Ashby (1999), Onck et al. (2005), Huisman et al. (2007). Thus, the stress-strain response in the rarefied phase is given by:

$$\varepsilon = \Gamma_L\left(\sigma\right) = \frac{\sigma}{E_L}, \tag{6.1}$$

where E_L is related to the Young's modulus of a single fiber E_s as in Gibson & Ashby (1999):

$$E_L = E_s \phi_0^2, \tag{6.2}$$
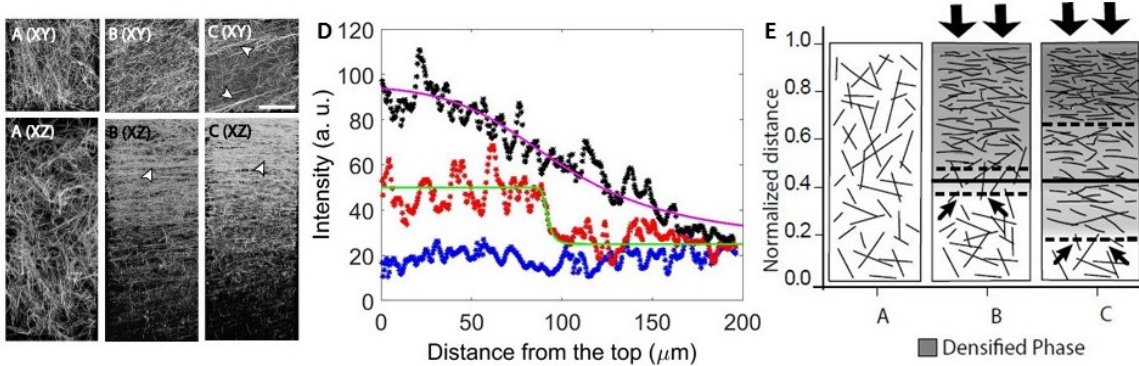
Figure 6.2: Three-dimensional reconstructions of the fibrin network under compression with different rates of compression and graph of the fluorescence intensity and schematic illustration of the changes in structure with distance under compression. (A-C) Three dimensional reconstructions (71 μm X 71 μm X 196 μm) of 392 optical sections of confocal images of plasma clots before and after compression, with different rates of compression. Both XY and XZ projections are shown for each set of images. (A) Before compression. (B) Clot compressed 2X at 10 μm/sec. (C) Clot compressed 2X at 100 μm/sec. Arrowheads point to aligned fibers. Magnification bar = 25 μm. (D) Distribution of fluorescence intensity in the Z direction averaged in the X direction over (392) of images in the XZ plane. Blue line is control of uncompressed clot; red and black lines correspond to a PPP clot compressed 2X at 10 μm/s, and 100 μm/s, respectively. Green and purple curves are fits from Eqn. (6.21) and (6.22). (E) A schematic presentation of images of the XZ planes based on 3D reconstruction of images and fluorescence intensity profiles of plasma clots with and without compression. A(XZ), clot without compression. B(XZ), compressed clot with rate of compression 10μm/sec. C(XZ), compressed clot with rate of compression 100 μm/sec. Large arrows indicate the direction of compression; small arrows show the boundary between densified and rarefied phases. Gray color indicates the densified phase, while no shading indicates the rarefied phase. The densified phase can be identified by increased fluorescence intensity in the confocal images, reflecting the increase of network density, along the direction of compression. It was defined as the distance from the top of images toward the bottom at the point where the intensity profile changed to the control level, and that distance was normalized by the maximum distance, since the same number of stacks were taken for all conditions and the same degree of compression was used for the two different rates of compression, 10μm/sec and 100μm/sec. The phase boundary is sharp at low compression rate and diffuse at high compression rate.

where ϕ_0 is the fibrin network volume fraction. In our notation $\sigma > 0$ for compressive stresses and $\varepsilon > 0$ for compressive strains. In the densified phase, fibers are bent and buckled with many contact points. The number of contact points N_c per unit volume in a dense isotropic network has been studied by Toll Toll (1998), and shown to be a function of fiber volume fraction ϕ as:

$$N_c = \frac{4}{\pi d^3}\phi^2, \tag{6.3}$$

80

where d is the diameter of fiber. A good approximation of the increase of volume fraction ϕ with compression of the clot is the form $\phi = \phi_0/(1 - \varepsilon)$ from our previous work Kim et al. (2016), where ε is the uniaxial compressive strain. Here I assume that the cross-sectional area change of the fibrin network during compression is small, and thus could be ignored. The stress-strain relation for this sort of dense network was proposed by van-Wyk Van Wyk (1946) and Toll Toll (1998) in the following form:

$$\sigma = kE_s \left(\phi^3 - \phi_0^3 \right), \tag{6.4}$$

where the coefficient k is determined by the material and loading conditions. It is found to be around 0.1 in Kim et al. (2016) for a fibrin network. Furthermore, fibrin fibers making contact and adhering to each other cause a reduction in the free energy of the network. I treat each formed contact point as a bond which releases free energy U_{bond}, resulting in a total energy per unit deformed volume which is given by

$$E = N_c U_{bond} + \int \sigma \varepsilon \mathrm{d}\varepsilon. \tag{6.5}$$

Plugging the expression of N_c from Eqn. (6.3) and for σ from Eqn. (6.4) into the above equation, and then differentiating this total energy, I get a new stress-strain law in the densified phase as:

$$\sigma = kE_s \left(\phi^3 - \phi_0^3 \right) - \frac{2C\phi_0^2 U_{bond}}{(1 - \varepsilon)^3} = \frac{K - \Delta G}{(1 - \varepsilon)^3} - K, \tag{6.6}$$

where $K = kE_s\phi_0^3$ is a constant with units of stress, and $\Delta G = 2CU_{bond}\phi_0^2$ is a normalized bonding energy density. From the measurements on densified fibrin networks in Kim et al. (2014, 2016), I estimate K to be around 10 kPa, but ΔG must be extracted from fitting to experiment. By inverting the above stress-strain relation for the densified phase I get

$$\varepsilon = \Gamma_H \left(\sigma \right) = 1 - \sqrt[3]{\frac{K - \Delta G}{\sigma + K}}. \tag{6.7}$$

Effect of platelets

Some clots examined in this paper contain platelets. These are cells that after activation attach to fibrin fibers in a clot and exert forces that are responsible for clot contraction.

Since thrombin is generated on the platelet surface and as a result of the forces exerted by platelets, the fibrin network can be locally dense around platelet aggregates Collet et al. (2002). Away from this locally dense region, the fibers are in tension and in the rarefied phase. The locally dense regions caused by platelets are uniformly distributed all over a clot. Since the platelets themselves are small (2-3 μm) I assume that their contribution to the overall mechanical response can be taken into account through a single variable – the pre-tension in the network denoted by σ_{pre}. Thus, the stress σ in the fibrin network is non-zero even at zero applied strain as is apparent in the initial part of the experimental stress-strain curve for the PRP and whole blood clots studied in this paper. Pre-tension in a clot can also be caused by other phenomena; for example, polymerization of the fibrin network between two parallel plates can result in some pre-stress, as seen in the PPP clots. I do not account for this separately, instead, the pre-stress due to all agents is represented by a single variable σ_{pre}. Thus, the stress-strain relation for the rarefied phase becomes

$$\Gamma_L(\sigma) = \frac{\sigma - \sigma_{pre}}{E_L}, \tag{6.8}$$

where E_L is a Young's modulus. In our experiments the pre-stress typically is tensile, $\sigma_{pre} < 0$. Also, platelet-poor plasma clots have lower pre-stress than platelet-rich plasma clots.

Phase transition theory

Next, I introduce the phase transition theory to model how a fibrin network responds when it is compressed and decompressed. In the loading process, as the stress σ increases from zero, the network starts in the rarefied phase. The transition to the densified phase nucleates at a critical stress $\sigma_{LH} < \sigma_M$, where σ_M is the maximum stress at which the rarefied phase can exist. Similarly, in the unloading process, the transition to the rarefied phase nucleates at critical stress $\sigma_{HL} > \sigma_m$, where σ_m is the minimum stress at which the densified phase can exist and $\sigma_{HL} < \sigma_{LH}$. Therefore, in the region between σ_{HL} and σ_{LH}, the two phases can co-exist at a stress σ. I define the strain difference between the two phases as a transformation strain:

$$\gamma_T(\sigma) = \Gamma_H(\sigma) - \Gamma_L(\sigma) = 1 - \sqrt[3]{\frac{K - \Delta G}{\sigma + K}} - \frac{\sigma - \sigma_{pre}}{E}, \qquad \sigma_m \leq \sigma \leq \sigma_M. \tag{6.9}$$

82

During the loading and unloading process, I assume that the fibrin network undergoes a phase change under quasi-static conditions, so that the stress in any part of the network is the same. Let $0 \leq z \leq h$ be the reference coordinate along the direction of loading, and $w(z, t)$ be the local displacement. The bottom at $z = 0$ is fixed, hence $w(0, t) = 0$ for all t. At the top the displacement is given as $w(h, t) = \delta(t)$. Suppose for $\sigma_{HL} \leq \sigma \leq \sigma_{LH}$, there is a separation at $z = s(t)$ between two parts of our continuum representing the network such that for $z < s(t)$ the network is in the rarefied phase and for $z > s(t)$ the network is in the densified phase. Therefore, the displacement at the top is given by:

$$w(h, t) = \delta(t) = \Gamma_L[\sigma(t)] s(t) + \Gamma_H[\sigma(t)][h - s(t)]. \tag{6.10}$$

In the above, I have denoted the position of the phase boundary by $s(t)$. In order to describe the motion of this phase boundary $s(t)$ as it goes from the top to bottom of the sample, I introduce a kinetic law Abeyaratne & Knowles (2006):

$$\dot{s} = \Phi(f) = \begin{cases} M_{LH}(f - f_{LH}), & \text{if } f > f_{LH}, \\ 0, & \text{if } f_{HL} \leq f \leq f_{LH}, \\ M_{HL}(f - f_{HL}), & \text{if } f < f_{HL}, \end{cases} \tag{6.11}$$

where Φ is a material property Abeyaratne & Knowles (2006), and:

$$f(\sigma) = \int_{\sigma_0}^{\sigma} \gamma_T(\sigma')\, d\sigma', \tag{6.12}$$

is the driving force on the phase boundary Abeyaratne & Knowles (2006). f is assumed here to be a unique function of stress, and σ_0 is a Maxwell stress, at which the Helmholtz free energy density of the two phases is equal. The parameters $M_{LH} > 0$ and $M_{HL} > 0$ in Eqn. (6.11) are mobilities that could be fitted to the experimental data and are not necessarily equal. $\Phi(f)$ must satisfy the dissipation inequality which requires that $f\dot{s} \geq 0$. Also, f_{LH} and f_{HL} correspond, respectively, to stresses σ_{LH} and σ_{HL} which may be determined using Eqn. (6.12). In order to complete the formulation of the problem, I need a nucleation criterion. This has already been mentioned above. For loading, when the specimen is being compressed, the densified phase nucleates in the rarefied phase at stress σ_{LH} where σ_{LH} can be assumed to be where driving force f is just greater than f_{LH} so that the phase

boundary makes its appearance and immediately begins to move. Similarly, for unloading, the rarefied phase nucleates in the densified phase at stress σ_{HL} where driving force f is just smaller than f_{HL}. Differentiating Eqn. (6.10) and eliminating $\dot{s}(t)$ using Eqn. (6.11) I get:

$$\left[\Gamma_L(\sigma)\Gamma_H'(\sigma) - \Gamma_L'(\sigma)\Gamma_H(\sigma) - \gamma_T'(\sigma)\frac{\delta}{h}\right]\dot{\sigma} + \gamma_T(\sigma)\frac{\dot{\delta}}{h} = \frac{\gamma_T^2}{h}\Phi(\sigma). \tag{6.13}$$

This governing equation gives the response of the network undergoing phase-transition during loading and unloading. The motion of the phase boundary during loading and unloading could be different due to the difference in the mobilities M_{LH}, M_{HL} and nucleation values f_{LH}, f_{HL}.

Effect of liquid pumping

One important feature of compressing and decompressing a fibrin network is that it contains liquid that is pumped out and then back into the network (Supplemental video). The pumping introduces a rate-dependence into the mechanical response of the network through the well-known mechanism of poro-viscoelasticity. An analytic formula for the compressive stress for a poro-viscoelastic foam under compression is given in Gibson & Ashby (1999) as:

$$\sigma_{li} = \frac{C_w\mu\dot{\varepsilon}}{1-\varepsilon}\left(\frac{D}{l}\right)^2, \tag{6.14}$$

where μ is the dynamic viscosity of the liquid, ε and $\dot{\varepsilon}$ are the compressive strain and its rate, D is horizontal dimension of the foam sample, and l is the cell edge-length of the foam. The coefficient C_w is about unity. The expression above assumes that ε is uniform through the sample, hence I will take $\varepsilon = w(h,t)/h$ where $w(h,t)$ is given by Eqn. (6.10). This formula gives a non-linear rate-dependent stress, which must be added to the stress due to the deformation of the fibrin fibers. If I imagine this strain-rate dependent stress as one due to a dashpot, then the dashpot is in parallel with a spring-dashpot arrangement characterizing the response of the fiber network (plus platelets). The total stress, σ_{tot}, in the network is then

$$\sigma_{tot}(\varepsilon, \dot{\varepsilon}) = \sigma(\varepsilon, \dot{\varepsilon}) + \sigma_{li}(\varepsilon, \dot{\varepsilon}). \tag{6.15}$$

84

Model for oscillatory shear of clots under compression

We measured the storage and loss modulus of all clots as a function of compressive strain during loading and unloading. In this section I will show how the dependence of the storage and loss modulus of PPP clots on compressive strain can be captured using our phase transition theory. Recall that compression causes the clot to be divided into two compartments – the upper compartment is the densified phase which has a shear modulus G_d (for small shear strains) and shear viscosity η_d for small shear rates, and the lower compartment is the rarefied phase with shear modulus G_r. In reality, the rarefied phase might have a small shear viscosity, but I assume it to be zero here to keep the fitting parameters to a minimum. The physics behind dissipation in the densified phase is fiber contact point friction as given in Kim et al. (2016), and possibly the viscous dissipation due to platelets and RBC. A viscosity parameter that captures the energy dissipation due to friction at the contact points is given as:

$$\eta = U_{bond}\tau_{on}N_c, \tag{6.16}$$

where τ_{on} is the average life-time of a bond. η will remain as a fitting parameter. Recent experiments by Kurniawan et al. (2016) shed some light on the strength of these contacts, but I could not estimate U_{bond} or τ_{on} from their results. The height of the upper compartment is z_d and that of the lower compartment is z_r. These heights will change with the compressive strain applied and they can be computed using our phase transition model. The overall response of clots under small shear strains can be viewed as a combination of springs and dashpot in series as shown in the inset of Figure 6.9a. In the experiment we apply a rotation θ_d to the top plate and measure the torque on it to extract a storage and loss modulus G' and G'', respectively, as a function of compressive strain. Our goal is to determine the values G_d, η_d and G_r that capture the trends in G' and G'' as a function of strain. To this end, first I note that the shear stress τ is

$$\tau(r) = G_r\gamma_r = \frac{rG_r\theta_r}{z_r\left(\varepsilon\right)}, \tag{6.17}$$

where θ_r is the rotation angle at the sharp phase boundary, z_r is the height of rarefied phase (Figure 6.9a) and r is radial coordinate on the plate. The densified phase has a viscoelastic

stress-strain relation as:

$$\tau(r) = G_d \gamma_d + \eta \dot{\gamma}_d = \frac{r G_d \left(\theta_d - \theta_r\right)}{z_d\left(\varepsilon\right)} + \frac{r\eta \left(\dot{\theta}_d - \dot{\theta}_r\right)}{z_d\left(\varepsilon\right)}, \tag{6.18}$$

where θ_d is the rotation angle of the top plate, and $z_d(\varepsilon)$ is the height of densified phase (Figure 6.9a). Combining Eqn. (6.17) and (6.18) I have:

$$\left(G_r z_d / z_r + G_d\right)\theta_r + \eta\dot{\theta}_r = G_d \theta_d + \eta\dot{\theta}_d. \tag{6.19}$$

In the experiment suppose the prescribed rotational angle of the top plate θ_d is given as $\theta_d = A\sin\omega t$. This will result in a shear stress also in harmonic form as $\tau = AG'\sin\omega t + AG''\cos\omega t$, and from Eqn. (6.17), I know the rotational angle of the interface $\theta_r = \left(G'\sin\omega t + G''\cos\omega t\right) z_r / G_r$. Then, plugging the expression of θ_r and θ_d into Eqn. (6.19), I solve for the modulus G' and G'' as:

$$\begin{aligned}
G' &= G_r \frac{\left(G_r z_d / z_r + G_d\right) G_d + \eta^2 \omega^2}{\left(G_r z_d / z_r + G_d\right)^2 + \eta^2 \omega^2}, \\
G'' &= \frac{G_r^2 \eta\omega z_d / z_r}{\left(G_r z_d / z_r + G_d\right)^2 + \eta^2 \omega^2}.
\end{aligned} \tag{6.20}$$

6.2   Results

Rheometry with cycling of compression and decompression was used to study the mechanical and structural responses of various kinds of blood clots to compressive strain. In other words, clots were formed between the rheometer plates, and then the upper plate was lowered to compress the clot. After a certain extent of compression was achieved, the upper plate was raised back to its initial point, which I call decompression. During the compression, when the upper plate moved down, serum, and serum with some RBCs in the case of whole blood clots, was squeezed out of the clots. When the upper plate was moved back up to its original position, the serum and serum with RBCs were pulled back into the clot (Supplemental video). During each cycle, which consists of two parts – compression and decompression – normal stress as a function of strain was measured and stress-strain curves were plotted. Figure 6.1 is an example of a typical plot of normal stress, σ, as a function of compressive strain ε for three successive cycles. The compression part of the cycle is designated as points a, b and c, while the decompression part of the cycle is designated as

points c, d and e. Resistance of clots to compression results in a compressive stress (with a positive sign, opposite of convention), while during decompression there is a tensile stress (with a negative sign), indicating that a tensile force must be applied to return the clot to its initial thickness.

6.2.1 Stress-strain response of blood clots during compression-decompression cycles

Our experiments demonstrated that the stress-strain curves depended on the type of clot structure and composition, including the presence of platelets and RBCs, as well as the degree and rate of compression and decompression. All three types of blood clots, made from PPP, PRP, and whole blood, were subjected to 1.5X and 2X compression of their initial thickness at two different rates, 10 μm/sec and 100 μm/sec.

6.2.2 PPP clots

Compression of PPP clots to $\varepsilon = 0.33$ resulted in an average normal stress of 1.48 kPa (Figure 6.1B(b-c)), while compression to $\varepsilon = 0.5$ gave a normal stress of 2.02 kPa. Unloading peaks during the decompression part of the cycle gave a normal stress of -1.61 kPa for $\varepsilon = 0.33$ (Figure 6.1B(d-e)) and -1.72 kPa for $\varepsilon = 0.5$ (Table 6.2). Increasing the rate of compression by 10 times resulted in increased stress values for all regions of the stress-strain curves. For example, at the same degree of compression $\varepsilon = 0.33$, the normal stress increased 6.9-fold for the loading peak and 4.7-fold for the unloading peaks. Increasing the strain up to $\varepsilon = 0.5$ resulted in an increase in the normal stress of 11.7-fold for loading and 9.8-fold for unloading peaks.

6.2.3 PRP clots

A PRP clot has stiffer clot structure compared to a PPP clot, so the original G' of the PRP clots was higher than that of the PPP clots (Supplemental Table 1). For the same strains, this results in higher stress in the compression experiments on PRP clots. At a compression rate of 10 μm/sec, PRP clots on average yielded higher normal stresses 2.03 kPa for the loading peaks, 3.77 kPa and for the unloading peaks, -1.84 kPa, -2.53 kPa for

$\varepsilon = 0.33$ and $\varepsilon = 0.5$, respectively (Table 6.2). Increasing the rate of compression by 10 times resulted in increased normal stress for all parameters (Table 6.2).

6.2.4 Whole blood clots

Whole blood clots differ from PPP and PRP clots because they contain RBCs that are incorporated into the fibrin-platelet network of the clots. RBCs represent about 40% of total volume in these clots. At a low rate of compression-decompression (10 μm/sec), whole blood clots yielded higher average stress values for loading and unloading peaks for both strains, compared to PPP and PRP clots. Loading peaks were 8.76 kPa and 20.89 kPa and unloading peaks were -5.10 kPa and -9.45 kPa for compressive strains of $\varepsilon = 0.33$ and $\varepsilon = 0.5$, respectively. Interestingly, for low compressive strain $\varepsilon = 0.33$, increasing the rate of compression-decompression by 10 times resulted in increasing the average stress value for loading and unloading peaks, to 16.53 kPa and -9.03 kPa, respectively. However, for a compressive strain of $\varepsilon = 0.5$, instead of increasing the normal stress, it decreased for both loading and unloading peaks (Table 6.2). There was an especially dramatic decrease for the unloading peak of -9 kPa for $\varepsilon = 0.33$, versus 0.9 kPa for $\varepsilon = 0.5$ compressive strains. Thus, at a low rate of compression-decompression (10 μm/sec), whole blood clots yielded higher average stress values for all parameters of stress-strain curves. However there is a dramatic decrease for loading and unloading peaks as well as for hysteresis area at higher rate of compression 100 μm/sec. These results may be attributed to dramatic structural changes, which are mostly irreversible (Section 6.2.7).

For all clots, the compressive stress increased with increasing compressive strain. In particular, for the low rate of compression of 10 μm/sec, increasing the compressive strain from $\varepsilon = 0.33$ to $\varepsilon = 0.5$ resulted in increasing the normal stress 1.4-fold for PPP clots, 1.9-fold for PRP clots and 2.4-fold for whole blood clots (Table 6.2). In addition, at strains up to $\varepsilon = 0.5$, PPP and PRP clots had a piecewise linear response to stress (Figure 6.5). However, for whole blood clots, increasing the compressive strain from 0.33 to 0.5 resulted in a more rapid upturn in normal stress and onset of a nonlinear response (Figure 6.7) compared to PPP and PRP clots. Increasing the rate of compression-decompression by 10 times resulted in increasing the average stress values for loading and unloading peaks for PPP and PRP clots compared to those at a low rate of compression-decompression. However, whole blood

clots respond in a different manner, such that increasing the compressive strain to 0.5 resulted in decreased loading and unloading peaks compared to those for PPP and PRP clots. The behavior is also due to irreversible changes in clot structure (Section 6.2.7).

6.2.5 Hysteresis in compression-decompression

The amount of hysteresis, as defined by the area within the compression-decompression curves, decreased with each cycle for all clots. There was an especially great decrease after the first cycle. Thus, during the compression-decompression cycling, clots dissipated energy and never returned to their original (structural) state. The hysteresis area depended on clot structure. The hysteresis area for PRP clots was higher than that for PPP clots, and it increased with increasing compressive strain for both rates. Also, the hysteresis area of whole blood clots at the low rate of compression of 10 μm/sec increased with increasing compressive strain and was greater than those for PPP and PRP clots, 5.52 versus 1.2 and 2.02 (Table 6.2) , respectively. However, increasing the rate of compression-decompression by 10 times had a dramatic effect on the hysteresis area of whole blood clots. The hysteresis area of whole blood clots at low compressive strain of 0.34 was about the same as that for PPP clots and decreased dramatically with increasing strain up to 0.5. Thus, our results indicate that the network of all clots apparently adjusted to the mechanical loading. The viscoelastic response (Section 6.2.6) and hysteresis behavior of compressed and uncompressed clots suggests that there are changes in clot structure, depending on the degree and rate of compression. Identification of these changes will help to determine the structural basis of the responses of clots to compression and decompression.

6.2.6 Shear storage and loss moduli as a function of strain

Shear storage (G') and loss (G'') moduli were measured as a function of strain during repeated compressive-decompressive loads for three cycles. When the maximum compressive strain was achieved, clots were decompressed to their original thickness at the same rate. Before and after each compression-decompression cycle, a small shear oscillation was imposed to measure the clot viscoelastic properties. Repeated compression-decompression cycles of blood clots revealed similar trends. During the compressive part of the cycles, G' and G'' moduli decreased, as the serum and serum with RBCs were squeezed out of

clots (Supplemental video). In the decompression part of the cycle, when clots returned to their original thickness, serum and serum with RBCs went back into the clots (Supplemental video). As shown in Supplemental Figure 3, PRP clots were found to be more rigid with a higher elastic modulus than PPP clots, and they became stiffer after cycling. For example, at the rate of 10 μm/sec and $\varepsilon = 0.33$, the final stiffness of the PRP clots was 1.4-fold higher than that for PPP clots. Increasing the compressive strain to 0.5 resulted in decreasing the difference between PPP and PRP clots to 1.1-fold. However, increasing the rate of compression-decompression by 10 times resulted in increasing the difference in final stiffness between PRP and PPP clots. At the low compressive strain of 0.33, the PRP clots were 1.2-fold stiffer than PPP clots. That difference increased to 1.6-fold by increasing the compressive strain to 0.5. In addition, the strain-stiffening of PPP and PRP clots progressively increased with cycling. For example, PPP clots ended up 4.2-fold stiffer on average after cycling of compression-decompression regimes.

Whole blood clot structure is different in comparison to PPP and PRP clots in that red- and white-blood cells are incorporated into these clots. Surprisingly, for whole blood clots, the stiffness decreased, instead increasing after the first cycle as happened for PPP and PRP clots. Although the stiffness was slightly increasing with each cycle, the stiffness never exceeded the original value. For example, the final stiffness of whole blood clots with a compressive strain 0.33 and 0.5 decreased by 2-fold and 1.6-fold after the first cycle at the lower rate of compression-decompression, but the stiffness decreased by 2.2-fold and 4-fold respectively, with an increase of the rate of compression-decompression by 10 times.

6.2.7 Structural changes in blood clots during compression-decompression cycling

We used confocal and scanning electron microscopy to determine how PPP, PRP and whole blood clots responded to cycling of compression-decompression loads, and to see what the structural bases for these mechanical behaviors are. At first, I studied PPP clots at the same degree of compression under two different rates of compression, 10 μm/sec and 100 μm/sec. At the maximum extent of compression, about 400 optical sections were collected for each clot using a confocal microscope. In response to compression, the fibrin network became divided into two regions with distinctive structural characteristics, a densified re-
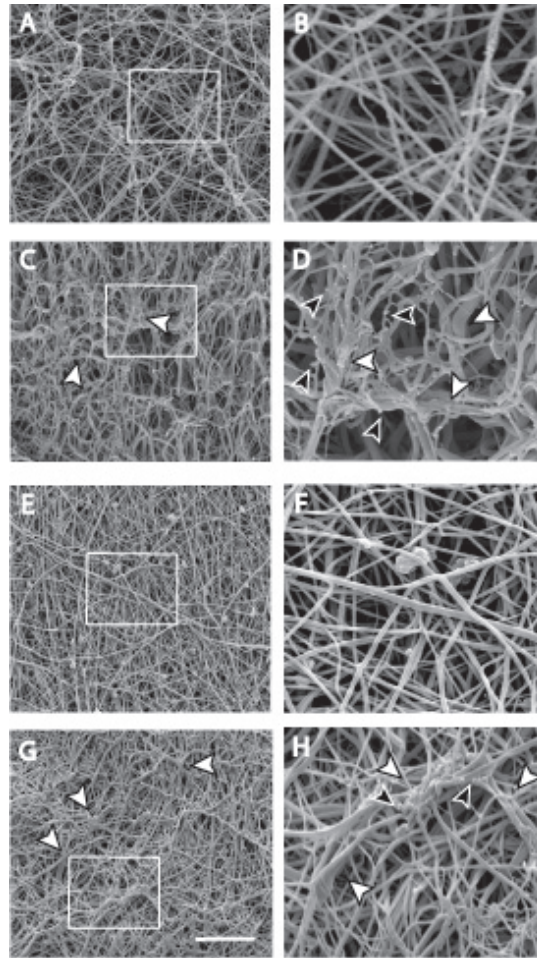
Figure 6.3: Changes in the structure of PPP and PRP clots after the first cycle of compression-decompression as observed by scanning electron microscopy. The clots were compressed 2X at a rate of 10 μm/sec and decompressed at the same rate. (A) PPP clot before compression. (B) Zoomed area from panel (A); (C) PPP clot after first cycle of compression-decompression. (D) Zoomed area from panel (C). (E) PRP clot before compression. (F) Zoomed area from panel (E). (G) PRP clot after first cycle of compression; (H) Zoomed area from panel (G). White arrowheads point to fibrin bundles; black arrowheads point to broken ends of fibers. Magnification bar = 10 μm.

gion adjacent to the top plate of the rheometer, where the compression was applied and a rarefied region below with a much lower fiber density (Figure 6.2A-C). Those changes depend on the rate of compression, such that the size of the densified region is larger and denser at the high rate of compression. To quantify the densified region, three-dimensional reconstructions of optical sections were carried out. The intensity profile was measured for all XY planes along the Z axis and plotted as a function of distance from the top of the clot, where compression started (Figure 6.2D). The densified area was identified by changes

of fluorescence intensity along the direction of compression. I found that a high rate of compression resulted in a denser network, which is reflected by the almost 2-fold higher maximum intensity than at a low rate of compression. In addition, increasing the rate of compression resulted in propagation of higher intensities (due to densification) deeper into the clot along the direction of compression. The boundary between the densified and rarefied region was sharper at the low rate of compression (Figure 6.2D). In terms of network structure, densification means buckling, bending, criss-crossing and bundling of fibers, as well as alignment of fibers in the plane perpendicular to the stress Kim et al. (2016). Those structural changes happened during the compressive part of the stress strain cycle (Figure 6.1(a-c)). During the linear elastic response from the beginning of compression to the first inflection point (Figure 6.1(b)), mostly bending and rotation of fibers occurred. During the next portion of the curve (Figure 6.1(b-c)), as compression proceeds, the distance between fibers was decreasing, which resulted in buckling, criss-crossing, bundling and reorientation of fibers in the network, such that they became aligned perpendicular to the direction of the compression (Figure 6.2A-C). As a result of those structural changes, the stiffness of the network decreased (Section 6.2.6). Some structural changes that occurred during compression were reversible while others were irreversible. The first part of the decompression curve was a non-linear elastic response that happens when the compressive strain changed less than 0.05, up to the first inflection point during decompression (Figure 6.1(b)). At this point, most of the reversible changes, such as bending and rotation, which happened during the linear response of compression, returned to their original form during decompression. As strain continued to decrease, the stress decreased due to network rearrangement via dissociation of fiber-fiber junctions that arose from contacts during compression. These rearrangements resulted in energy dissipation, and the second cycle of compression started with a clot with some structures still modified.

To determine how the network changed in detail after the first cycle of compression-decompression, scanning electron microscopy was performed. It is very clear that after the first compression-decompression cycle, the network of PPP clots was rearranged (SEM Figure 6.3A-D). After the first cycle, the thickness of fibers increased for the clots as a result of both criss-crossing and bundling of fibers during compression. However, not all fibers stuck to each other either in criss-crossing structures or in bundles, and were dissociated after decompression was completed. In addition, many fibers ends were observed for PPP clots,

probably as a result of fiber breakage. Those changes in clot structure were responsible for the increasing stiffness of the clot with each cycle. The next sets of experiments were carried out with PRP clots. I found that PRP clots responded on compression-decompression cycles generally in a similar manner as PPP clots. Originally, PRP clots have a denser fibrin network compared to PPP clots, which means shorter distances between fibers and smaller pore size. Due to those differences, more bundling and criss-crossing were observed in PRP clots (SEM Figure 6.3E-H) than in PPP clots. Those structural differences resulted in higher stiffness after the first compression-decompression cycle (Section 6.1.3). There were similarities and differences in the responses of whole blood clots on compression-decompression cycling, as compared to PPP and PRP clots. The same densified and rarefied regions were observed in the fibrin network. The differences are likely due to clot composition, since a major component of whole blood clots are RBCs that make up about 40% of the clot volume. As I observed during compression-decompression cycling, RBCs move out during compression and move back into the clots during decompression (Supplemental video). When I measured the hematocrit of the blood, and hence the hematocrit of the clot before compression, and the hematocrit of the serum and RBCs expelled from the clot at the point when compression was completed but decompression had not yet started, surprisingly the hematocrit was the same, meaning that the RBCs were expelled from the clot in the same proportion as the serum. Furthermore, all the RBCs that were forced out of the clot during compression returned during decompression. To follow the structural changes of whole blood clots during compression and decompression, clots were examined by confocal microscopy. I found that RBCs, while initially randomly distributed throughout the clot, were rearranged non-randomly during the compressive part of the cycle. They were pushed down in the direction of compression into the rarefied phase, as well as being forced out with the liquid. As a result of this redistribution, more RBCs were observed in the bottom of the clot in the rarefied region and on the periphery of clot near the edges of the rheometer plates, while there were few RBCs in the densified region, which was mostly fibrin network (Figure 6.8C).

Interestingly, the shape of RBCs in the compressed clot changed as a result of compression, such that no biconcave cells were observed in the compressed clot. In addition, many fibrin fibers in the densified zone were oriented perpendicular to the direction of compression, as observed for PPP and PRP clots. When the restraints keeping the clots compressed

were removed and the clots were allowed to relax for an hour before being imaged in the confocal microscope, I observed that some liquid with RBCs moved back into the clot. This passive decompression corresponds to the linear response up to the first inflection point (Figure 6.1(c-d)). Interestingly, after passive decompression, most RBCs were polyhedrocytes (Figure 6.8E, F). To see in detail the structural changes in whole blood clots after the first compression-decompression cycle, those clots were examined by scanning electron microscopy, with observations consistent with those from confocal microscopy. Some irreversible changes occurred, e.g. the fibrin network was rearranged with thicker fibers and smaller pore sizes than before compression (Supplemental Figure 2B, D, F). Furthermore, most of the RBCs present after the first compression-decompression cycle were polyhedral in shape (Supplemental Figure 2B). Also, on the periphery of the clot at the edges of the rheometer plates, RBCs were a more prominent component, as a result of the compression-decompression cycle.

6.2.8 Location of phase boundary

The fluorescence intensity of fibrin as a function of depth (measured from the top) through the deformed samples is plotted in Figure 6.2D. The blue dots represent an uncompressed sample, red dots represent a sample compressed to half its original height at a rate of 10 μm/s, and the black dots represent a sample compressed to half its original height at a rate of 100 μm/s. I see clearly that the fluorescence intensity is larger near the top of the compressed samples. I have observed this sort of segregation in earlier work Kim et al. (2016) in which a locally densified region of the fibrin network under compression is separated from a rarefied region by a (diffuse) front. I assume that the fluorescence intensity is proportional to the local network density which scales as $1/(1-\varepsilon)$ where $\varepsilon(Z) = \mathrm{d}z/\mathrm{d}Z - 1$ is the compressive strain. If the strain profile $\varepsilon(Z)$ is given by a hyperbolic tangent function (see Kim et al. (2016) for why I choose this functional form),

$$\varepsilon = a + b \tanh \frac{Z - Z_0}{c}, \tag{6.21}$$

94

with a, b, c and Z_0 constants, then the deformed position z (measured in experiment) of a plane located at reference position Z in the unstressed sample is

$$z(Z) = d + (1 - a)Z - bc \log \left(\cosh \frac{Z - Z_0}{c} \right), \tag{6.22}$$

where Z_0 is the location of the center of the front in the unstressed configuration. d is chosen such that $z(0) = 0$ (at the bottom of the clot which is the static rheometer plate), and a, b, c are obtained by fitting the experimentally measured fluorescence intensity (which is proportional to the fiber density) in Figure 6.2D. For the low strain rate (10 μm/s), $a = 0.4, b = 0.2, c = 10$ μm gives the green curve. For the high strain rate (100 μm/s), $a = 0.52, b = 0.27, c = 180$ μm gives the purple curve. Both curves give the center of the interface at $Z_0 = 460$ μm, while the total height of the undeformed sample is $h = 600$ μm. Thus, the phase boundary moves the same distance through the sample irrespective of the strain rate because it has been compressed by exactly the same amount in both cases. However, a smaller c value for the low strain rate experiment indicates a sharp front separating the rarefied and densified phases, whereas a larger c value for high strain rate indicates a wide and diffuse front. The value of a for the two strain rates is also different, which results in much higher strains (more densification) behind the phase boundary for the high strain rates. In contrast to our experimental results, the model of Kim et al. (2016) does not capture the strain-rate dependence of the phase boundary width. In the model of Kim et al. (2016) the width of the phase boundary depends on a capillarity (or interfacial energy) parameter λ and on the stress-strain curve of the fibrin network, but not on the viscosity parameter ν which multiplies the strain-rate. Hence, our experiments suggest that a more sophisticated model in which ν is not constant, but depends on the pore-size in the fibrin network (as in Eqn. (6.14)) is likely needed to capture strain-rate dependence of the phase-boundary width.

6.2.9 Application of phase transition model to PPP and PRP clots

The stress-strain curves of PPP and PRP clots under compression can be computed using these ideas as shown in Figure 6.4. The fitting parameters are given in Table 6.1. I
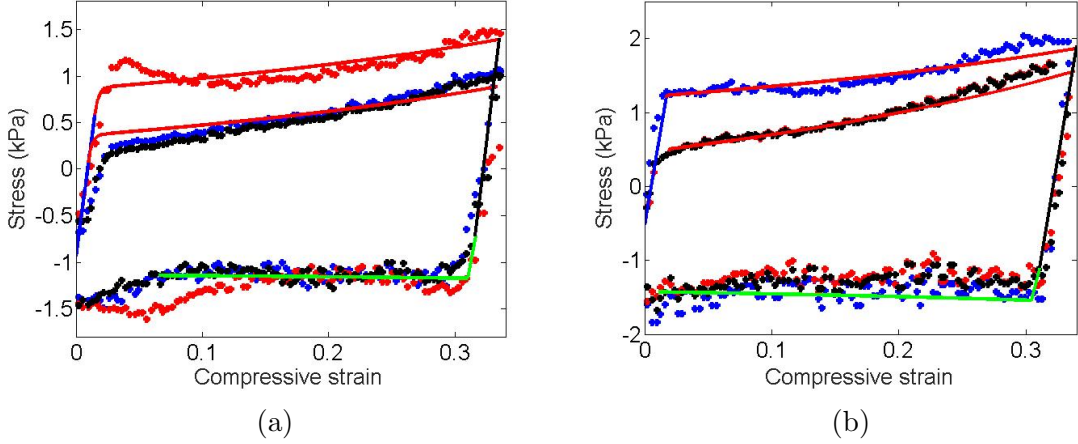
Figure 6.4: (a) Fitting of stress-strain cruves of PPP clots low strain rate, small compression degree. (b) Fitting of stress-strain curves of PRP clots low strain rate, small compression degree. Each clot is compressed and decompressed in three cycles; red dots (first cycle), blue dots (second cycle), black dots (third cycle). Note that the first cycle gives a different stress-strain curve than the other cycles. Most fitting parameters are the same for each cycle, and I can use them to predict the corresponding cycles in the low strain rate high compression degree experiments and the high strain rate experiments. The solid lines are obtained by fitting our theory to the data; blue line (loading rarefied phase), red line (upper plateau), black line (unloading densified + rarefied phase), green line (lower plateau).

use the following procedure to fit the curves. First, I fit the low strain linear response using Eqn. (6.8) and obtain σ_{pre} and E_L. Next, I consider the initial steep part of the unloading curve (which does not include the lower plateau) and remember that this curve is given by

$$\varepsilon = x_1 \Gamma_L(\sigma) + (1 - x_1)\Gamma_H(\sigma), \tag{6.23}$$

where x_1 is a fixed fraction of the rarefied phase with $0 < x_1 < 1$ and $\Gamma_H(\sigma)$ is given by Eqn. (6.7). Since $\Gamma_L(\sigma)$ is already known the fitting parameters are x_1, K and ΔG. With $\Gamma_L(\sigma)$ and $\Gamma_H(\sigma)$ known, I now want to fit the plateau region of the stress strain curves using the differential equation Eqn. (6.13). For the upper plateau, the fitting parameters are M_{LH}, σ_{LH}, and for the lower plateau the fitting parameters are M_{HL} and σ_{HL}. I perform our fits for the low strain rate small compression degree experiments on both PPP and PRP clots. Each of these plots contain data from three compression-decompression cycles on the clots. The first cycle gives a different response from the subsequent cycles, which is captured in our model through a difference in σ_{LH} during loading, and σ_{HL} during unloading. Typically, for both PPP and PRP clots σ_{LH} becomes smaller from the first cycle to the second. This

96

Table 6.1: Fitting parameters for low strain rate compression experiments.

Group	PPP clot	PRP clot	Whole blood clot
σ_{pre} (kPa)	-2.2	-2.2	-3.2
E_L (kPa)	10	10	15
K (kPa)	10.25	10.25	10.25
ΔG (kPa)	10	10	10
σ_{LH} (kPa) in 1st cycle	1.5	2.1	4.7
σ_{LH} (kPa) in 2nd cycle	1.4	1.3	1.7
σ_{LH} (kPa) in 3rd cycle	1.6	1.3	1.7
σ_{HL} (kPa) in 1st cycle	-0.5	-0.7	-0.5
σ_{HL} (kPa) in 2nd cycle	-0.6	-0.7	1
σ_{HL} (kPa) in 3rd cycle	-0.4	-0.7	1
M_{lh} (kPa^{-1}s^{-1})	0.06	0.06	0.06
M_{hl} (kPa^{-1}s^{-1})	0.04	0.04	0.04
C_w	1	1	1
C_{neo}	0	0	9

suggests that there is rearrangement in the clot structure at network and fiber levels (Figure 6.3C, D, G, H), perhaps due to adhesion of fibers, which makes the buckling stress for fibers smaller after the first cycle. The theoretical curves match the experimental data very well for both PPP (Figure 6.4a) and PRP clots (Figure 6.4b) for each cycle.

6.2.10 Predictive capability of our model

We have used the parameters extracted from these fits to predict the (a) low strain-rate high compression degree experiments for PPP clots (Figure 6.5a) and PRP clots (Figure 6.5b), and high strain-rate experiments (Figure 6.6) on both types of clots. In Table 6.2 I compare model and experiment on five different metrics – loading peak stress, unloading peak stress, loading average stress, unloading average stress and hysteresis area (enclosed by the loading/unloading stress-strain curve) – and show that our model does well on all the metrics.

It is important to point out that while experiments and theoretical predictions agree very well in Figure 6.5 in all parts of the stress-strain curve (low strain phase, upper plateau, high strain phase, lower plateau), this is not true of Figure 6.6 which are from the high strain rate experiments on the PPP and PRP clot samples. In the latter I capture the general features (such as, hysteresis, peak stresses, etc.) quite well, but the overall shape of the experimental and theoretical curves differ markedly, particularly in the unloading plateau.
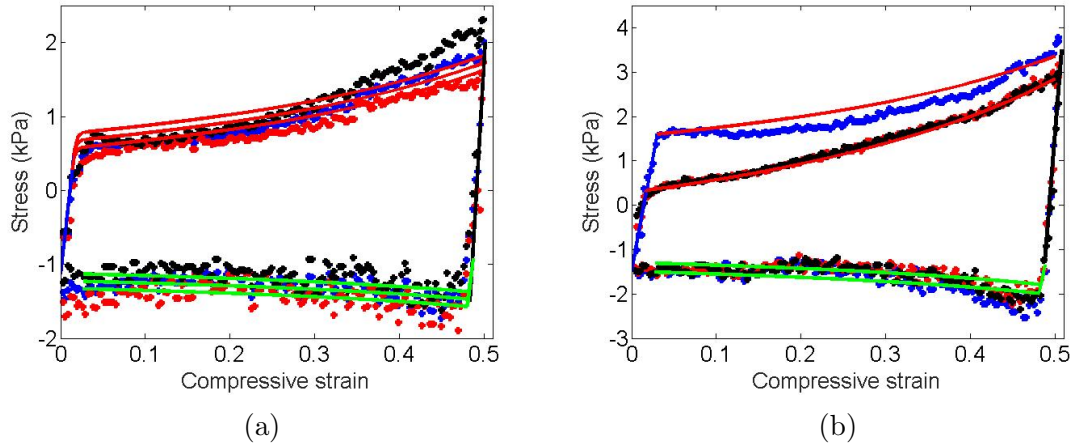
Figure 6.5: (a) Theoretical prediction (solid lines) for PPP clots low strain rate large compression degree matches experiment (dots). (b) Theoretical prediction (solid lines) for PRP clots low strain rate large compression degree matches experiment (dots). The coloring scheme for the lines and dots is the same (Figure 6.4).

The reasons for this are not completely clear to us, but we suspect that the more diffuse phase boundary seen for the higher strain rate experiments in Figure 6.2D is the reason for the disagreement. Recall that our phase transition theory assumes a sharp phase boundary separating the rarefied and densified phases to get the upper and lower plateaus. Evidently, this is a good assumption for the low strain rate experiments, but not for the high strain rate ones (Figure 6.2D). Since strain rate dependence in our model arises from liquid pumping and phase boundary kinetics I expect that a model accounting for strain-rate dependence of the phase boundary width will also lead to a kinetic law different from Eqn. (6.11) that might help capture the trends in Figure 6.6. A larger data set of the high strain-rate experiments for PPP, PRP, and whole blood clots for various compression degrees and multiple cycles is shown in the supplement. The form of the stress-strain curves, the area of the hysteresis loops, etc., are similar to those shown in Figure 6.6. Table 6.2 includes comparisons of the stress-strain curves in the supplement with our theoretical predictions for the five metrics.

6.2.11   Effect of RBCs on mechanical response

While PPP and PRP clots could be modeled quite well by introducing a pre-tension (due to platelets) into constitutive laws for foams, I need to account for RBCs in order to
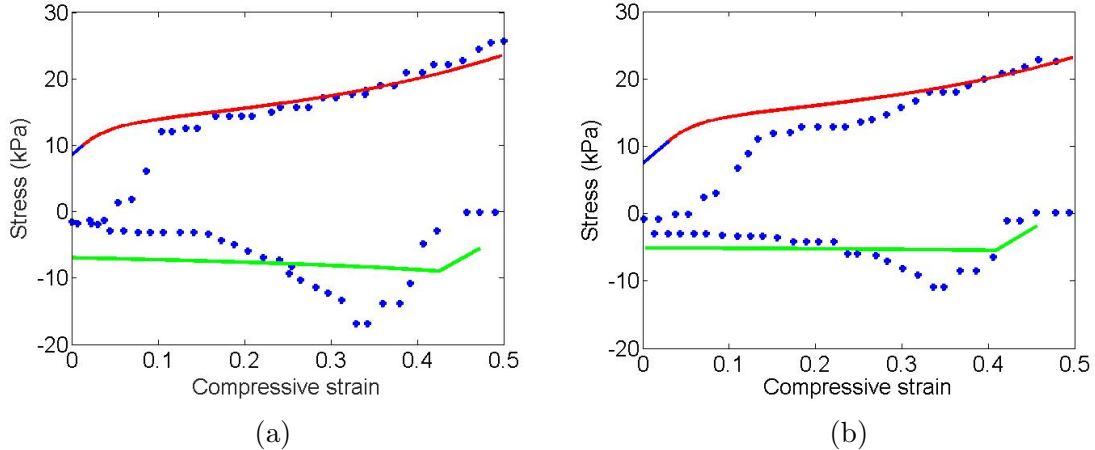
Figure 6.6: (a) Theoretical prediction (solid lines) for PPP clots high strain rate experiments (dots). (b) Theoretical prediction (solid lines) for PRP clots high strain rate experiments (dots). Although the general features (upper plateau, average stress during loading, hysteresis area) of the experimental curves are captured by the theoretical prediction, the agreement is not as good as for the low strain rate experiments. The reason for the disagreement could be that the theory assumes a sharp phase boundary, while fluorescence imaging in Figure 1.2 reveals a diffuse phase boundary for the high strain rate experiments.

model the compression of whole blood clots. The large deformation response of RBCs under tension and compression has been analyzed using continuum constitutive models as in Dao et al. (2003), Lim et al. (2004), in which a non-linearly elastic neo-Hookean model given in Simo & Pister (1984) and based on the classic experiments of Evans and Hochmuth Evans & Hochmuth (1976), Hochmuth et al. (1979) is shown to predict the response quite well. In our notation (in which $\varepsilon > 0, \sigma > 0$ for compression) this model of an RBC in uniaxial tension/compression boils down to Ogden (1997):

$$\sigma_{neo} = 2C_{neo}\frac{3\varepsilon - 3\varepsilon^2 + \varepsilon^3}{1 - \varepsilon} = 2C_{neo}\left(3\varepsilon + \frac{\varepsilon^3}{1 - \varepsilon}\right), \qquad (6.24)$$

where C_{neo} is a material constant, that could be fitted to experiment. In our experiments I find that the RBC flow out with the liquid from the rarefied phase of the clot when it is compressed, but they are sucked back into the network when it is decompressed. Thus, the stress due to liquid pumping will now have another contribution that depends on the fraction of the RBCs present in the densified phase. We model this in a simple way by

Table 6.2: Comparison of metrics for the stress-strain curves obtained from experiment and theory.

Group	Loading peak	Unloading peak	Loading average	Unloading average	Hysteresis area
PPP clot 1.5X 10	1.48 ± 0.19	-1.61 ± 0.22	1.09 ± 0.13	-1.28 ± 0.17	0.65 ± 0.09
Theory	1.40	-1.17	1.10	-1.15	0.71
PPP clot 1.5X 100	10.25 ± 0.85	-7.5 ± 1.01	8.33 ± 0.69	-5.88 ± 0.82	3.43 ± 0.93
Theory	9.97	-6.08	8.22	-5.80	4.18
PPP clot 2X 10	2.02 ± 0.28	-1.72 ± 0.11	1.03 ± 0.14	-1.3 ± 0.13	1.10 ± 0.12
Theory	1.82	-1.46	1.08	-1.32	1.05
PPP clot 2X 100	25.71 ± 1.95	-16.89 ± 1.80	18.68 ± 0.6	-6.58 ± 0.57	9.04 ± 0.90
Theory	23.44	-8.88	16.9	-7.68	10.76
PRP clot 1.5X 10	2.03 ± 0.14	-1.84 ± 0.23	1.49 ± 0.16	-1.43 ± 0.26	0.97 ± 0.19
Theory	1.79	-1.64	1.50	-1.47	0.94
PRP clot 1.5X 100	16.92 ± 1.59	-14 ± 1.6	14.82 ± 1.41	10.8 ± 1.5	5.3 ± 0.49
Theory	17.31	-7.53	12.37	-7.1	5.88
PRP clot 2X 10	3.77 ± 0.45	-2.53 ± 0.29	2.14 ± 0.23	-1.66 ± 0.21	2.02 ± 0.27
Theory	3.05	-2.55	1.80	-1.50	1.58
PRP clot 2X 100	22.8 ± 2.95	-10.09 ± 1.77	16.5 ± 2.14	-4.63 ± 0.87	6.90 ± 0.35
Theory	23.14	-8.48	17.33	-7.10	6.58
Whole blood clot 1.5X 10	8.76 ± 0.96	-5.10 ± 0.12	5.1 ± 0.74	-2.61 ± 0.79	2.21 ± 0.45
Theory	9.14	-5.23	5.00	-2.51	2.24
Whole blood clot 1.5X 100	16.53 ± 1.82	-9.03 ± 1.23	11.9 ± 1.17	-5.79 ± 0.82	3.95 ± 0.38
Theory	15.78	-8.73	11.17	-6.25	4.01
Whole blood clot 2X 10	20.89 ± 1.4	-9.45 ± 2.25	8.26 ± 0.94	-3.14 ± 0.93	5.52 ± 1.01
Theory	19.10	-10.79	8.17	-4.17	5.78
Whole blood clot 2X 100	19.43 ± 1.01	-0.92 ± 0.12	15.47 ± 1.32	-0.56 ± 0.15	5.50 ± 0.63
Theory	30.2	-14.73	18.37	-8.24	8.97

All stresses are in units of MPa
Number before X indicates compression degree
Number after X indicates compression rate in μm/s

changing the expression for the stress due to liquid pumping:

$$\sigma_{li} = \frac{C_w \mu \dot{\varepsilon}}{1 - \varepsilon}\left(\frac{D}{l}\right)^2 + 2(1 - x(t))C_{neo}\left(3\varepsilon + \frac{\varepsilon^3}{1 - \varepsilon}\right), \tag{6.25}$$
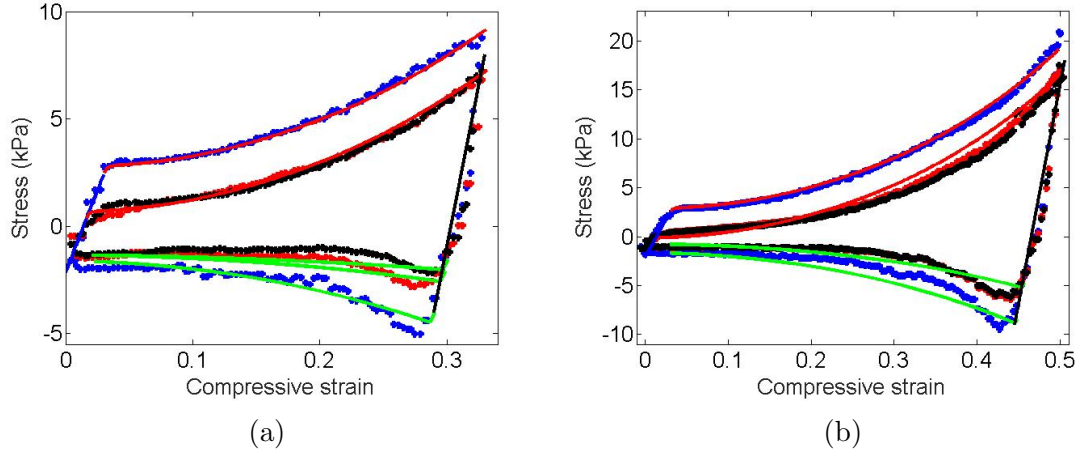
Figure 6.7: (a) Fitting of stress-strain curves of whole blood low strain rate, small compression degree. (b) Prediction for whole blood low strain rate, large compression degree. The coloring scheme of the lines and dots is the same as in figure 6.5. Again, first cycle is different from the second and subsequent cycles.

where $x(t) = s(t)/h$ is the fraction of the rarefied phase. The total stress is still given by Eqn. (6.15). In reality, the distribution of the RBCs in the blood clot is heterogeneous (see Figure 6.8). The deformed RBCs were found predominantly near the outer edge of the compressed (cylindrical) clots in the densified phase (see Figure 6.8C and D); these contribute to the stress in a big way. There were regular biconcave RBCs in the rarefied phase of the clots (see Figure 6.8), but these do not contribute much to the stress since they are undeformed. Our model above is a simplification since it assumes that the stress carrying RBCs (those in the densified phase) are uniformly distributed through the sample and that the sample itself has a uniform strain ε. I have used our phase transition model with this modification to fit the low strain rate, small compression degree experiments on whole blood samples in Figure 6.7(a). Again, the first loading/unloading cycle is different from the subsequent cycles. The fitting parameters are given in Table 6.1. They are not very different from the fitting parameters for PPP and PRP clots, except I have an extra parameter C_{neo} for whole blood that accounts for the RBCs, which are absent in PPP and PRP clots. Using these fitting parameters, I can predict the response for low strain rate, high compression degree experiments on whole blood (Figure 6.7(b)). The agreement between theoretical predictions and experiments is excellent. This is also evident in the metrics tabulated in Table 6.2.

101
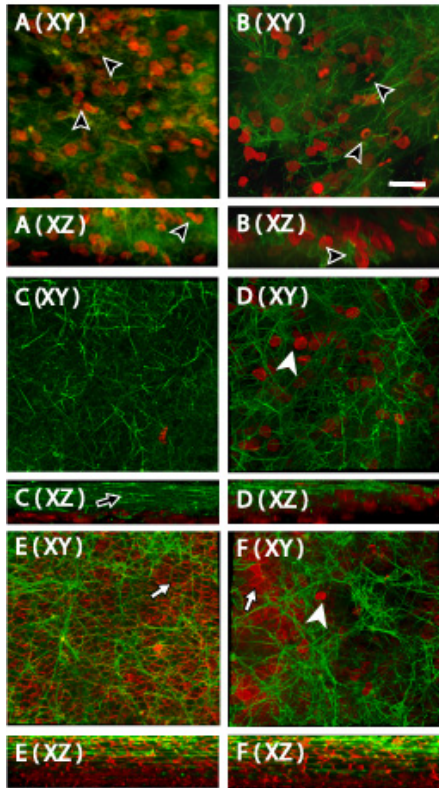
Figure 6.8: Three-dimensional reconstructions of different areas of compressed and decompressed whole blood clots, showing changes in fibrin network structure and the distribution of RBCs. Three-dimensional reconstructions (134 μm X 134 μm X 25 μm) from 45 optical sections of volumes of whole blood clots with and without compression, taken from the top toward the bottom. The clots were compressed 2X at a rate of 10 μm/sec and decompressed at the same rate. (XY) and (XZ) indicate the direction of view. Black arrowheads point to normal biconcave erythrocytes, while white arrowheads point to deformed erythrocytes. White arrows indicate polyhedrocytes and black arrows point to the aligned fibrin network in the densified phase. (A) Clot with no compression, and images taken from the middle part of the clot. (B) Clot with no compression, and images taken from the edge of the clot. (C) Compressed clot, and images taken from the middle part of the clot. (D) Compressed clot, and images taken from the edge of the clot. (E) Decompressed clot, and images taken from the middle part of the clot. (F) Decompressed clot, and images taken from the edge of the clot. Magnification bar = 25 μm
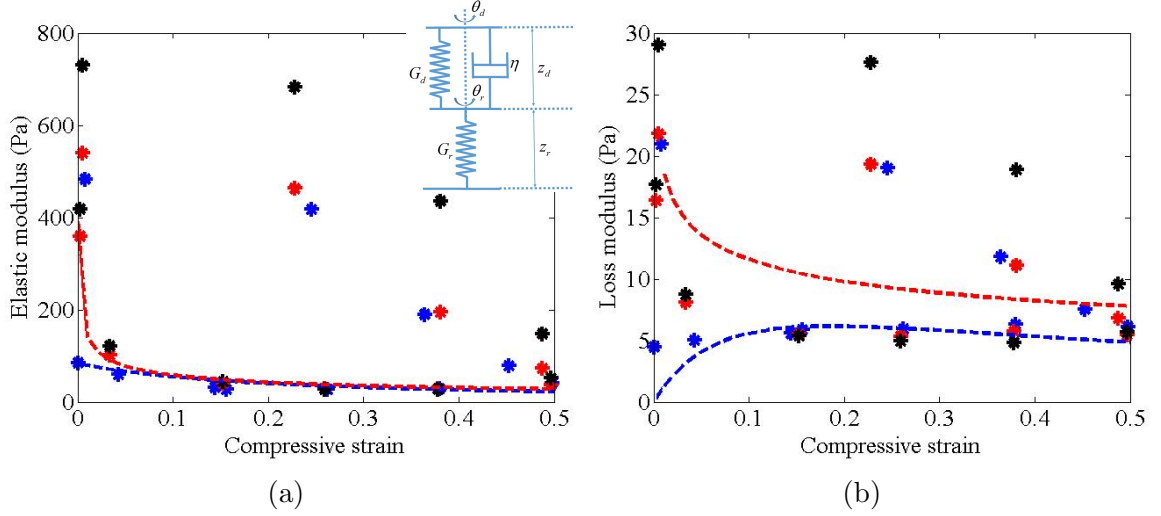
Figure 6.9: (a) Fitting of oscillatory shear experiment on PPP clots. Blue, red, and black dots are first, second, third cycles, respectively. Blue and red lines are theoretical predictions of G' and G'' during loading.

6.2.12 Shear storage and loss moduli as a function of compressive strain

We fit the experimental data using the formula given in the Section 6.1.3. Note that $z_r(\varepsilon)$ and $z_d(\varepsilon)$ for each compressive strain ε can be obtained for these PPP clots using our phase transition model with parameters given in Table 6.1. In our experiment, the oscillation frequency is 1.5 Hz. The combination of fitting parameters $G_r = 84$ Pa, $G_d = 30$ Pa, and $\eta = 6$ Pa·s gives a good match to the storage and loss moduli data for the first loading cycle. The combination of fitting parameters $G_r = 400$ Pa, $G_d = 30$ Pa, and $\eta = 6$ Pa·s gives a good match to the second and third loading cycles. In both cases, the shear modulus of the densified phase is smaller than that of the rarefied phase. This is because the buckled fibers in the densified phase bend easily to accommodate the small displacements due to shear, while the straight fibers in the rarefied phase have to rotate while being constrained by other fibers. Also, note that G_r for the second and third cycle is larger than that for the first cycle. This is consistent with our observations of the compression stress-strain curves for PPP clots in which the first cycle is different from the subsequent cycles and shows that there is rearrangement of the fibers after the first cycle, perhaps due to fibers adhering to each other.

The arguments given above validate our phase transition model. However, some conun-

103

drums still remain. First, note that while the storage modulus for small shear strains is in the range of 10^2 Pa for the rarefied phase, the Young's modulus for compression in the rarefied phase E_L is in the kPa range. This is not expected for a classical foam whose Young's modulus and shear modulus are of the same order of magnitude Gibson & Ashby (1999). Second, during unloading, both G' and G'' of the same clots are much larger than those during loading at the same compressive strains. This could be because of different values of z_r and z_d during unloading due to the different kinetic laws governing phase boundary motion in the upper and lower plateaus. However, the simple model above cannot capture the trends in G' and G'' during unloading even after accounting for the different kinetic law in the lower plateau. I do not yet understand the reason behind this disagreement during unloading, but speculate that the following could play a role: (a) energy dissipation due to the phase boundary motion itself, (b) different shear behavior of the fibers and bonds in tension (because the stress in the unloading plateau is tensile). A larger data set for the measured storage and loss modulus of PPP, PRP, whole blood clots in different cycles is given in the supplement. I have not attempted to fit that data set using the formula above, but the trends in measured G' and G'' are similar to those given in Figure 6.9.

6.3 Discussion

6.3.1 Stress-strain curves

In the present study, the mechanical response of PPP clots, PRP clots, and whole blood clots to axial compression and decompression was experimentally measured, correlated with structural changes for all components and modeled. We observed directly for the first time the stress-strain curves of all three types of clots and showed that they not only demonstrate foam-like behavior in response to compression/decompression, but also that they respond in a manner similar to carbon nanotube forests (Chapter 6). The stress-strain curves (Figure 6.1) for strains up to $\varepsilon = 0.5$ for each of the three types of clots revealed four characteristics portions: 1) linear elastic regime (a, b in Figure 6.1), where (b) is the first inflection point during compression; 2) a plateau or softening (b, c), where (c) is the end of compression and the beginning of decompression; 3) a non-linearly elastic regime or stretching of the network (c, d), where (d) is the first inflection point during decompression; 4) a second plateau in

which dissociation of some newly made connections in the network occurs (d, e), where (e) is second inflection point during decompression and (a) is the end of decompression and beginning of compression again. The same four regimes are present in the stress-strain curves of carbon nanotube forests as is well-documented in Maschmann et al. (2012), Pathak et al. (2012), Raney, Fraternali & Daraio (2013) and numerous other publications. Maschmann et al. (2012) have visualized the local strain profiles in compressed carbon nanotube forests; their images suggest the propagation of one or two interfaces through the sample (as explained in Chapter 6), which is similar to our observations in blood clots shown in Figure 6.2. Here I have demonstrated that the stress-strain curves depended on the type of clot structure, including the presence of platelets and RBCs, as well as the degree and rate of compression and decompression.

6.3.2 Role of platelets in mechanical response

The initial stiffness of PRP clots was higher than that of PPP clots. Platelets are able to generate contractile forces that apply tension to fibrin shortly after the clot is formed and, as a result, they exert internal stresses within the network Jen & McIntire (1982), Wen & Janmey (2011). Thus, a fibrin network that has been pre-stressed by platelets has a larger 'negative normal stress' before compression than does a fibrin clot without platelets. I show that PRP clots had higher than average normal stresses for all parameters: loading peaks, unloading peaks and hysteresis area, in comparison to PPP clots (Table 6.2). This finding is consistent with results on PPP clots for which the degree of clot stiffening during compression strongly depended on clot pre-compression history Kim et al. (2014).

6.3.3 Role of RBCs in mechanical response

The stress response of PPP and PRP clots for strains up to 0.5 seems piecewise linear, while whole blood clots showed a non-linear response for compressive strains greater than 0.2. This early onset of non-linear stress response could be attributed to differences in clot composition. Whole blood clots are considerably more complex in structure and their mechanical responses arise from the combination of fibrin, platelets, RBCs and other components arranged in a complex geometry. The effects of platelets were discussed in Section 6.2.11. Approximately 40% of the volume of whole blood is made up of RBCs and

in clots they tend to segregate themselves in the pores of the fibrin network during polymerization Gersh et al. (2009). RBCs can undergo large mechanical deformations without rupture in response to mechanical forces. Under compression, they can change shape from normal biconcave to polyhedrocyte Cines et al. (2014), and then return to their original shape with cessation of compression. This ability of RBCs could be attributed to their cytoskeleton, which is a two-dimensional spectrin network with triangular shape Discher et al. (1994), since spectrin filaments are considered to be soft elastic elements among cytoskeletal components Wen & Janmey (2011).

Our results show that compression of this complex structure consisting of a semi-flexible network (fibrin) arranged and pre-stressed by platelets, with pores partially filled with soft RBCs, caused some of the RBCs to escape from the network, due to their flexibility. RBCs moved from densified regions (with mostly compressed fibrin and platelets) to the rarefied areas below the phase boundary, as well as out of the clot. No biconcave RBCs were observed during the compressive part of the cycle, indicating that those RBCs that did not escape went through shape deformations. In most of the densified region only a few RBCs were observed. At the top of the densified region, where fibers were aligned perpendicular to the direction of compression, few RBCs were observed. Previous studies Weiss & Katzberg (1952), Corey et al. (2007) showed that, independent of any forces, an aligned matrix of fibers could direct cell growth along the fibers. We showed that during the compressive part of the cycle that fibrin fibers are aligned in a direction perpendicular to the direction of compression and parallel to the rheometer plate. Those aligned fibers could aid in guiding the RBCs out of the clot, consistent with the correlation of mostly aligned fibers in densified areas and no RBCs in those same areas during the compressive part of the cycle (Figure 6.8C-D). Also, it has been shown that substrate stiffness can control cell movements Lo et al. (2000), and a recent study employing strain-stiffening composites made from soft polymers comes to similar conclusions Ma et al. (2013). Thus, for whole blood clots I demonstrated the effects of both the direct role of forces or matrix stiffness and matrix alignment on the movement of RBCs. During the decompressive part of the cycle, RBCs moved back into the clot and filled the network, even though some irreversible changes to the fibrin network had occurred. Irreversible changes in the fibrin network as a result of cycling include bundling and criss-crossing of fibers, which caused decreases of the average pore size of the network (Figure 6.3). Decreasing the pore size of the network resulted in changes of RBC shape,

with most RBCs observed in the decompressive part of the cycle being of polyhedral or intermediate shapes.

6.3.4 Repeated cycles of compression-decompression

All blood clots were subjected to three loading and unloading cycles, and I found that the stress-strain curves of the first cycle differed from those of the second and third cycles. This effect has also been observed in compression of carbon nanotube forests Raney, Fraternali & Daraio (2013) in which after the first cycle the stress-strain curve does not change for dozens of cycles. As in the carbon nanotube forests, this suggests that there were structural changes in the clots, some which could be reversible and others irreversible. As I observed, clot structures for all blood clots were different after the first cycle of compression/decompression (Figure 6.3 and Supplemental Figure 2). The thickness of fibers increased, and the pore size of the network decreased as a result of fiber criss-crossing. These findings confirmed that not all structural changes during the compression/decompression cycle were reversible, consistent with the hysteresis observed in the stress-strain curves. These changes in clot structure were responsible for the changes observed in the viscoelastic properties as well as for hysteresis behavior for all types of blood clots upon cyclic loading. I showed that all structural modifications of all blood clots during the cycle and after each cycle result in changes of stiffness.

As compression proceeds, at first fibers buckle and bend and then with increasing strain fibers are forced into each other and become criss-crossed and bundle as the network density increases. The increasing strain also results in the reorientation of fibers, such that many fibers become aligned in the plane perpendicular to the direction of compression (Figure 6.2A-C and 6.8). Bent and buckled fibers can no longer contribute effectively to resisting deformation, resulting in decreasing the stiffness during the early compressive part of the cycle. Since unbuckling and unbending do not require energy, those changes are reversible upon decompression. However, the binding forces between fibers that are criss-crossing or bundled are strong Bonn et al. (2016), the dissociation of these linkages requires energy and resulted in energy dissipation in each cycle. During decompression, some fibers are separated while others stay associated, resulting in new clot structures after compression/decompression cycles (Figure 6.3). These morphological changes arising from an increase in criss-crossed

and bundled fibers result in decreasing pore size and increasing the fiber thickness, which means an increasing clot stiffness with each cycle. I found that for PPP and PRP clots, G' increased after each cycle, in agreement with these changes in clot structure. However, for whole blood clots, instead of increasing, the stiffness decreased after the first cycle, which may be attributed to differences in composition of whole blood clots. Many of the pores are filled up with soft RBCs before compression. Thus, compression of whole blood clot resulted in less criss-crossing and bundling, since the RBCs block these interactions, but more bending and buckling than in PPP and PRP clots.

Moreover, RBCs escape from the fibrin network during the compressive part of the cycle (see Supplemental video) and moved down from the densified region to the rarefied region (Figure 6.8C), which resulted in a dramatic decrease in stiffness during the compressive part of the cycle. During the decompressive part of the cycle, RBCs moved back into the clot distorted from irreversible changes in the network, and filled up new spaces that are now more compact. These changes resulted in shape transformation of some cells from biconcave to polyhedral such that the second cycle of compression starts with a clot with deformed RBCs. These deformations of RBCs and dissociation of newly formed fibrin fiber linkages within the network, resulted in higher energy dissipation for whole blood clots than for PPP and PRP clots. In addition, there is relatively less fibrin in whole blood clots because of the presence of RBCs, in comparison with PPP and PRP clots. All these differences resulted in decreasing G' in subsequent cycles for whole blood clots, instead increasing G' as observed in PPP and PRP clots after each cycle.

6.3.5   Effects of the rate and extent of compression-decompression on mechanical response

We observed that, in response to compression, the fibrin network for all blood clots was divided into two regions, a densified region (with bent and buckled fibers) and a rarefied region (with mostly straight fibers), with a boundary between them. The fluorescence intensity profile of compressed clots as a function of depth revealed that the boundary front propagates through the sample. The width and sharpness of the boundary depends on the rate of compression. At low compression/decompression rates, the phase boundary is sharp (or has a small width), while at high rates of compression/decompression, the boundary

is diffuse. The propagation of this boundary through the sample is the basis of our phase transition model to describe the compressive behavior of blood clots Abeyaratne & Knowles (2006). The strain-rate dependence of the phase boundary width remains a topic for future research since the model in Kim et al. (2016) does not fully capture the physics behind this effect. A new model for the phase boundary width will also result in a different kinetic law in the phase transition model required to explain the full stress-strain response.

6.3.6 Phase transition model

In terms of the stress-strain curves, the rarefied region corresponds to a linear response when strain is low and the entire clot is rarefied and the densified region has a non-linear stress-strain response. At the two plateaus, upper for the compressive part of the curves and lower for the decompressive part, the clot is a mixture of the rarefied and densified phases separated by a moving phase boundary. The mobility of the phase boundary is different for the loading and unloading plateaus and has been taken into account in our phase transition model for all three types of clots. Also, our phase transition model accounts for two criss-crossing fibers adhering to each other in the densified phase through a certain energy of adhesion (Section 6.1.3). The presence of platelets in the clot is represented through a specific pre-stress in the rarefied phase (Section 6.1.3). Poroelastic effects are necessary to account for the pumping of liquid through the clot during compression Gibson & Ashby (1999). Finally, the deformation of RBCs by compression (Section 6.2.11) makes a major contribution to the stress-strain relations in whole blood clots; it has been accounted for by using classical expressions based on a neo-Hookean constitutive law.

Our phase transition model captures the entire stress-strain response of all three types of clots. I evaluated the constants entering the model by fitting the low strain rate and low compression degree experiments for each type of clot. Then, I showed that the same parameters can predict the response of the clot for high rate and high degree of compression. The prediction of our model at high strain rates for PPP and PRP clots are not as good as the low strain rate prediction, likely because I assume a sharp phase boundary, which is in conflict with our observation of a diffuse phase boundary at high strain rates. For whole blood clots our model works very well for both high and low strain rates. The position of the phase boundary enters into a simple calculation for the shear storage and loss moduli

of compressed clots. I find that the trends in storage and loss moduli as a function of compressive strain for PPP clots during loading can be captured by our phase transition model. The trends in storage and loss moduli during unloading are not captured in our analysis and remain a topic for future research. A possible reason for this discrepancy could be that the physics behind the small strain shear behavior of the clots under tension is different from that in compression.

6.3.7 Significance of the compression behavior of blood clots

Clot mechanics is an important part of the field of hemostasis and thrombosis because blood clots and thrombi undergo dramatic deformations under (patho)physiological conditions such as hydrodynamic blood flow, retraction of platelets, and contraction of muscle surrounding blood vessels. Therefore, the outcomes of many bleeding and thrombotic disorders, including thromboembolism, are largely determined by mechanical behavior of the clot or thrombus. The mechanical response of blood clots and thrombi to compression is important for their hemostatic function, obstructiveness and stability. The modeling of compression front propagation as a dynamic phase transition and stress-strain curves in cyclic compression/decompression, as well as the rheological properties of clots containing platelets and RBCs, are predicted in this paper. This could become a useful diagnostic tool for diseased states since I can predict how the compression response and rheology of clots will change if platelet function is impaired (naturally or due to drugs), or the RBCs are too stiff (as in sickle cell disease), or fibers are too thick (e.g., if the clot is formed in the blood of a hemophiliac). Thus, studies on the compressive behavior of clots and thrombi may reveal how clot rheology under large compression in vivo varies in pathological conditions such as deep vein thrombosis, pulmonary embolism, hemophilia, and sickle cell anemia.

Aside from its significance to hemostasis and thrombosis, blood clot mechanics has become increasingly important in view of extensive new applications of fibrin and other clot components as a biomaterial, e.g., in tissue engineering, cell culturing, drug delivery, wound sealing, etc., where the mechanical support provided by a clot network, in combination with other properties, makes it a unique, versatile, and quite useful hydrogel. I have shown that blood clots with platelets and/or with RBCs are a biological composite material with unique mechanical properties. The information from these studies may enable design of

110

tissue sealants and scaffolds with precisely tunable mechanical and structural properties.

Chapter 7

Compression of CNT foams

In this chapter I apply a phase transitions based model to the compression response of vertically aligned carbon nanotube (CNT) forests, obtained via quantitative *in situ* micro-compression experiments. In doing so I assume that the CNT forest is an elastic foam whose stored energy function has two wells – one corresponding to the rarefied phase in which the CNTs are mostly straight, and the other corresponding to the densified phase in which the CNTs are mostly buckled with a large number of contacts between them. The existence of broad convex regions around the minima in the energy landscape of CNT forests is attributed in Radhakrishnan et al. (2013) to the reversibility of the deformation under moderate strains (as seen in experiments Qiu et al. (2011), McCarter et al. (2006) as well as simulations Radhakrishnan et al. (2013)). Such reversibility is also characteristic of phase changing materials whose Helmholtz free energy function has multiple minima, each of which correspond to different micro-structure Bhattacharya (2003), Gibson & Ashby (1999). In order to accommodate the deformations imposed on the boundary a phase changing material forms microstructure in the bulk in which different phases co-exist at the same stress Bhattacharya (2003), Gibson & Ashby (1999); analogously, there is a range of stresses at which the densified and rarefied phases of CNT forests can co-exist to accommodate deformations imposed at the boundary. The idea of a multi-well energy landscape A similar idea has appeared in a series of papers that describe the CNT forests as a one-dimensional mass-spring chain in which the springs are characterized by a double well potential Fraternali et al. (2011), Blesgen et al. (2012), Raney, Wang & Daraio (2013), Raney, Fraternali & Daraio (2013), Thevamaran et al. (2015). These models acknowledge the multi-scale nature

of the mechanical response of CNT forests and allow for the possibility that the properties could be graded Blesgen et al. (2012), so that the buckling load of the fibers could be a function of position. They also predict discrete jumps in the load-displacement curves (as the springs jump from one energy minimum to another) much like the discrete buckling events of CNT forests loaded in uniaxial compression. A continuum limit of this type of model has also been obtained and used to interpret the dissipation in loading/unloading experiments Raney, Fraternali & Daraio (2013). However, to the best of our knowledge, these models do not connect the micro-structural parameters of the CNT forests (such as, density, CNT diameter) with the constitutive parameters entering the model as is done in the literature on foams. A micro-structural connection based on the mechanics of foams has been presented by Hutchens et al. (2012) who recognize that CNTs can adhere to each other causing a reduction in the energy of the forest under compression (see also Zbib et al. (2008)). They connect the microscopic sticking behavior of CNTs to the visco-plastic hardening rule used in the fully three-dimensional computational framework of Hutchens et al. (2010). A more comprehensive nano-scale computational model which represents CNTs in a forest as elastica finite elements with van der Waals interactions was described by Torabi et al. (2014) and Volkov et al. (2009). Torabi et al. (2014) establish relationships between post-bulking stress, initial elastic modulus, and buckling wavelength on statistical parameters (tortuosity, density and connectivity) of a CNT forest which a macroscopic constitutive model, ideally, should reproduce. Separately, it has been argued that such a macroscopic constitutive law for describing coordinated buckling of CNT forests should be *local* because constitutive properties exhibit only statistical variations across a CNT forest from top to bottom as demonstrated by uniaxial compression and nanoindentation experiments of Qiu et al. (2011).

Here I use a local *continuum* phase transition theory to study the uniaxial compression of CNT forests and include phase boundary kinetics as well as a nucleation criterion to describe features seen in the stress-strain curves. In contrast to a discrete mass-spring chain, a continuum phase transition model describes layer buckling of CNT forests as continuous interface (separating rarefied and densified phases) propagation (see cartoon in Figure 7.2a). I (and others) have shown in recent work that the dynamics of discrete bi-stable mass-spring chains can be captured by a continuum phase transition theory if information lost in going from the discrete to continuum description is distilled into a kinetic relation and nucleation

113

criterion that are supplied as constitutive information to the continuum theory Zhao & Purohit (2016), Zhao et al. (2015), Truskinovsky & Vainchtein (2005). A continuum phase transitions model, in contrast to a discrete mass-spring chain, is needed to model the response of CNT forests under loading configurations that are more complex than uniaxial compression. Here I demonstrate this idea by using our constitutive model to interpret indentation experiments on the CNT forests in which the stress and strain fields are inherently three-dimensional (see Figure 7.2a). Phenomenological constitutive models that capture the load-indentation depth curves in nanoindentation experiments have been implemented recently using finite elements by Radhakrishnan et al. (2013), but to the best of our knowledge, these models have not been used to explain the collective buckling of CNT forests under uniaxial compression. In contrast, our continuum model can be applied to both uniaxial compression as well as nanoindentation experiments. It is characterized by a double-well energy landscape, much like the springs of Fraternali et al. (2011) and Blesgen et al. (2012), but it incorporates a rate-dependent kinetic law to describe the motion of phase boundaries in the spirit of Hutchens et al. (2010). Hutchens et al. (2010) used a visco-plastic computational model because the deformation of the CNT forests in their experiments was not fully recoverable. In contrast, the CNT forests in our experiments showed deformations that were largely recoverable with hysteresis, similar to Cao et al. (2005), Pathak et al. (2012).

This chapter is laid out as follows. In section 7.1 I describe the preparation of the CNT forest samples. In section 7.3 I describe the *in situ* scanning electron microscopy (SEM) experiments, and how the data from the compression experiments is interpreted using a phase transitions model. An insight that emerges from our analysis of the experimental data within a phase transitions model is that the buckling wave length of the CNT forests is related to the energy of the interface separating the rarefied and densified phases. In section 7.7 I briefly describe the nanoindentation experiments on the same samples, and how the data from these experiments can be interpreted by incorporating a linearized version of our phase transitions based model into solutions for indentation of an elastic half-space. The purpose of section 7.7 is to show that our phase transitions based model of section 7.3 can predict the response of the CNT forests to indentation even though the state of stress in indentation is very different from that in uniaxial compression.
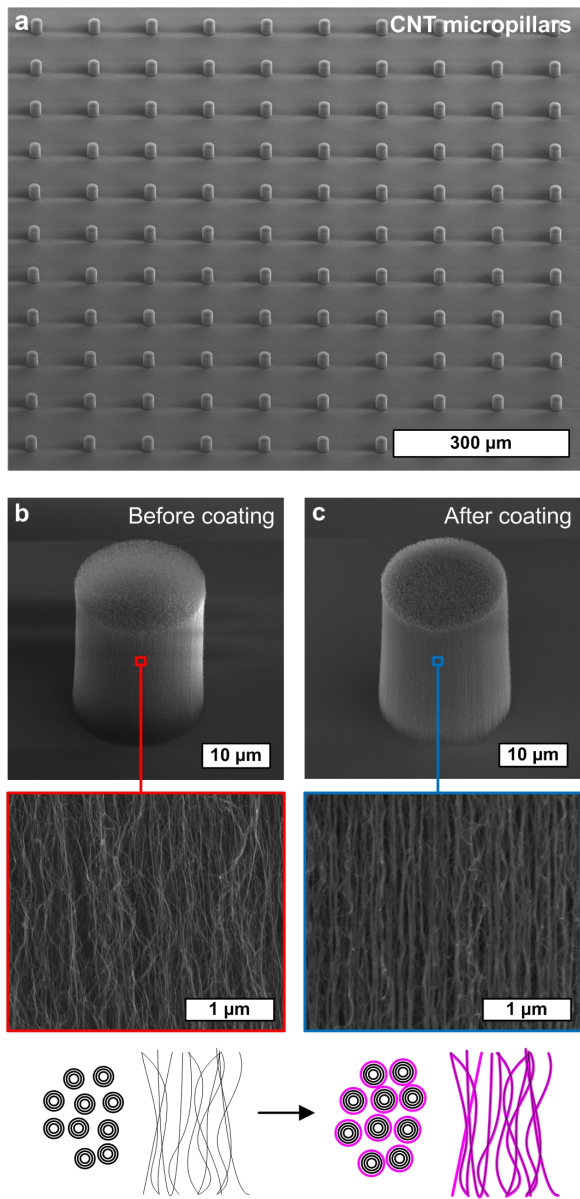
Figure 7.1: (a) SEM image of an array of CNT pillars used for mechanical characterization; (b) SEM image of individual pillar, close-up of CNT forests as viewed from sidewall, and top/side view schematic of CNT forests without ALD coating; (c) corresponding images after ALD coating with Al_2O_3.

7.1 CNT forest growth

For the growth of vertically aligned CNTs (see Figure 7.1), an Al_2O_3/Fe catalyst layer is first patterned on 4" (100) silicon wafers coated with 300 nm of thermally grown SiO_2, by lift-off processing using photo-lithography followed by ultrasonic agitation in acetone. The supported catalyst layer, 10 nm of Al_2O_3 and 1 nm of Fe, is sequentially deposited by

electron beam physical vapor deposition. The wafer with the deposited catalyst is diced into 1×1 cm pieces, and for each sample one piece is placed in the quartz tube furnace for the CNT growth. The growth recipe starts with flowing 100/400 s.c.c.m. of He/H_2 while heating the furnace up to 775 °C over 10 min (ramping step); then the temperature is held at 775 °C for 10 min with the same gas flow rates (annealing step). Then the gas flow is changed to 100/400/100 s.c.c.m. of $C_2H_4/He/H_2$ at 775° C for CNT growth for the selected duration based on the typical growth rate of approximately 100 μm/min (growth step). Once the desired growth time has passed, the same gas flow is maintained while the furnace is turned off, allowing the system to cool. Once the furnace temperature reaches below 100 °C, 1000 s.c.c.m. of He is maintained for 5 min to purge the quartz tube before the samples are retrieved.

7.2 ALD Al_2O_3 coating

Optionally, the as-grown CNT samples are then coated with Al_2O_3 via ALD (Arradiance, GEMStar XT); each cycle deposits 1.1-1.3 Å of Al_2O_3. Trimethylaluminum, $Al_2(CH_3)_6$, and ozone, O_3, were used as the precursors. The deposition is performed at 175 °C and 1 Torr, and between introduction of each precursor, the chamber is evacuated to ensure that no residual precursor remained in the chamber.

7.3 Compression of the CNT forests

After CNT growth and ALD coating, the CNT forests patterned as pillar compression specimens are placed in a custom nanomechanical testing apparatus for quantitative *in situ* mechanical testing in a scanning electron microscope (SEM). The testing apparatus consists of three key components: a 6DOF closed loop nano-positioning stage (SmarAct GmbH), a linear piezoelectric actuator (Physik Instrumente GmbH), and a MEMS-based silicon capacitive load cell (FemtoTools AG) as illustrated in Figure 7.2b. The apparatus has been described in detail previously Magagnosc et al. (2013), Zhao et al. (2015). The testing setup is installed in a high resolution SEM (FEI Quanta) for mechanical testing of the CNT pillars and simultaneous high resolution observation (see Figure 7.2c).

Testing was performed according to the following procedure. The SEM stage was tilted
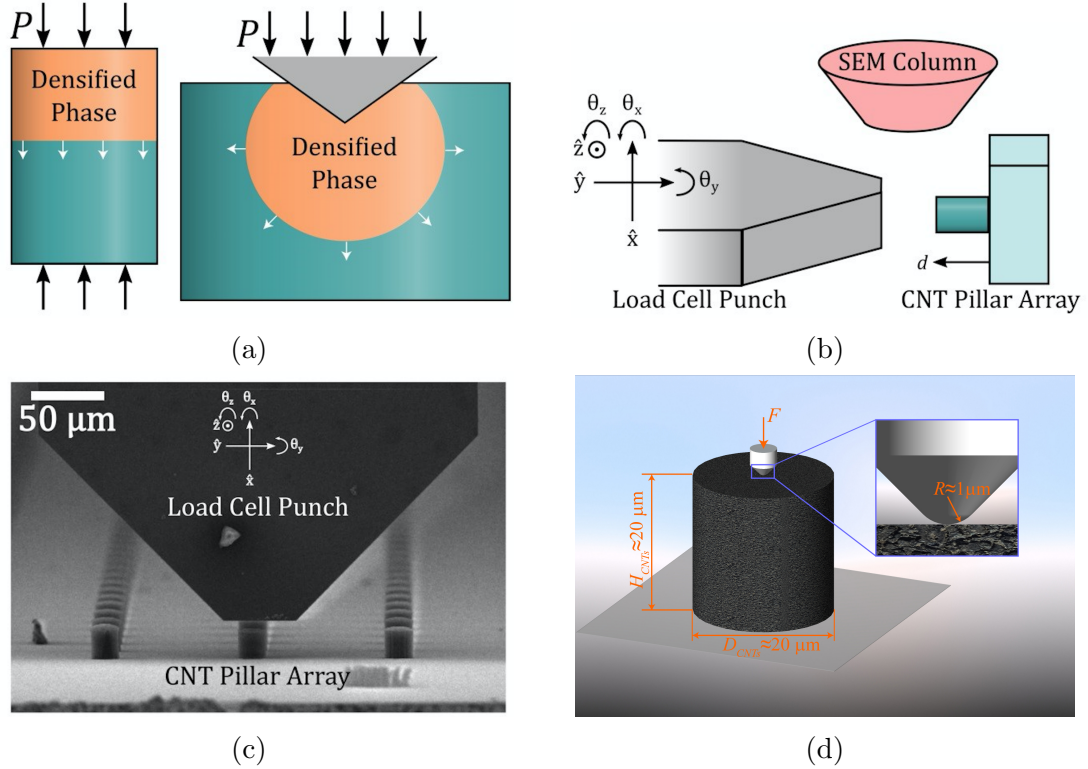
Figure 7.2: (a) Schematic of two experimental configurations (and, thus, stress states) investigated: uniaxial pillar compression (left) and nanoindentation(right). In each case an interface, or phase boundary, separates the densified and rarefied phases. The phase boundary is flat in the uniaxial compression experiments and has an axi-symmetric shape in the nanoindentation experiments. As the load P increases, the volume of the densified phase increases by the outward motion of the phase boundary (shown by arrows). (b) Schematic of *in situ* SEM mechanical testing configuration used for pillar compression, and (c) low-magnification SEM image of testing apparatus and pillar specimens. (d) Illustration of nanoindentation test on a CNT pillar.

by $< 5°$ to provide an unobstructed view of the CNT pillar array as depicted in Figure 7.2c. A coarse angular alignment of the load cell indenter to the CNT pillars was first performed visually. Fine angular alignment was achieved using the previously reported contact stiffness method Zhao et al. (2015) on the CNT growth substrate. By maximizing contact stiffness, good alignment of the CNT pillars and load cell was ensured, most notably in the y-z plane (out of the imaging plane). The load cell was then visually aligned in the x, y, and z directions with a selected pillar for testing. Quasi-displacement controlled uniaxial compression was performed while recording the actuator displacement, force, and an imaging sequence at nominal strain rates between 0.001 s^{-1} and 0.1 s^{-1}.

The pillars tested here generally showed different moduli and plateau stresses, yet con-
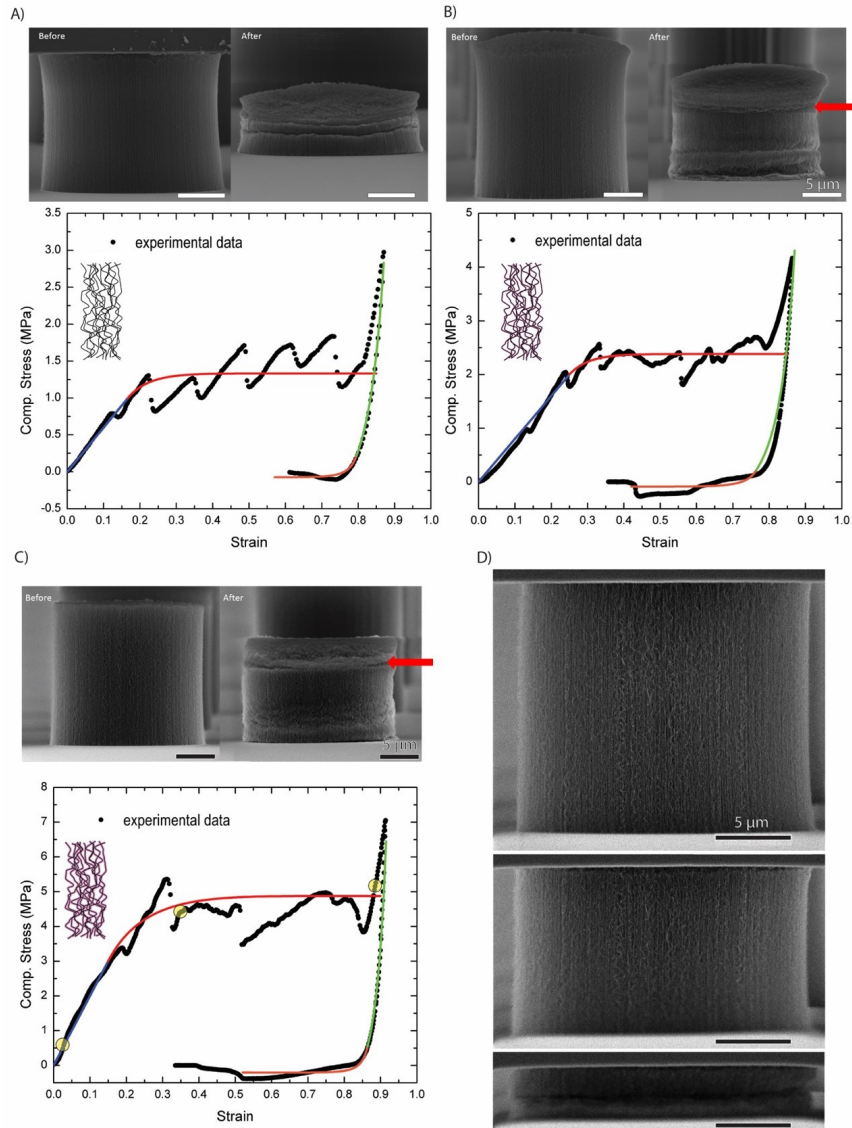
Figure 7.3: Quantitative in situ uniaxial compressive behavior and SEM images of (a) bare CNT, (b) ALD 5 cycles and (c)ALD 10 cycles pillars. An arrow next to the SEM images in (b) and (c) shows the position of the phase boundary above which the forest is densified. The dots in each plot are experimental data and the lines are from the phase transition model. Blue line corresponds to rarefied phase during loading, upper red line to a mixture of rarefied and densified phases during loading, green line to densified phase during unloading, and bottom red line to mixture of rarefied and densified phases during unloading. Note that around a strain of 0.8 there is a difference between the loading and unloading curves (for the densified phase) obtained from experiments. (d) SEM snapshots obtained from the highlighted regions of the stress-strain curve in (c) showing the elastic, plateau, and densification regimes.

sistent loading behavior regardless of ALD coating thickness, as shown in Figure 7.3 and

7.5. This general behavior is shown for uncoated (Figure 7.3a), ALD 5 cycles (Figure 7.3b),
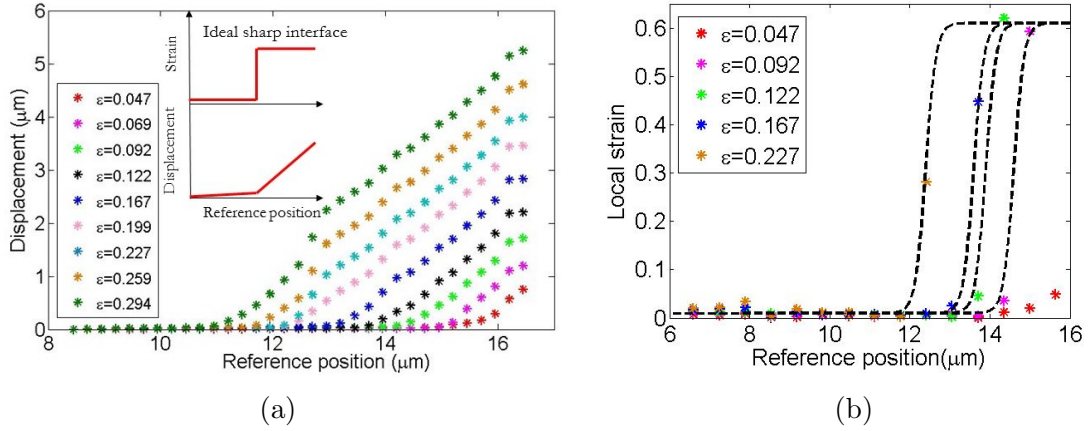
Figure 7.4: (a) DIC measurement of displacement at each reference position for various global compressive strains from 0.047 to 0.294. (b) DIC measurement of local strains for various global compressive strains from 0.047 to 0.227 and fitting with Eqn. (7.21).
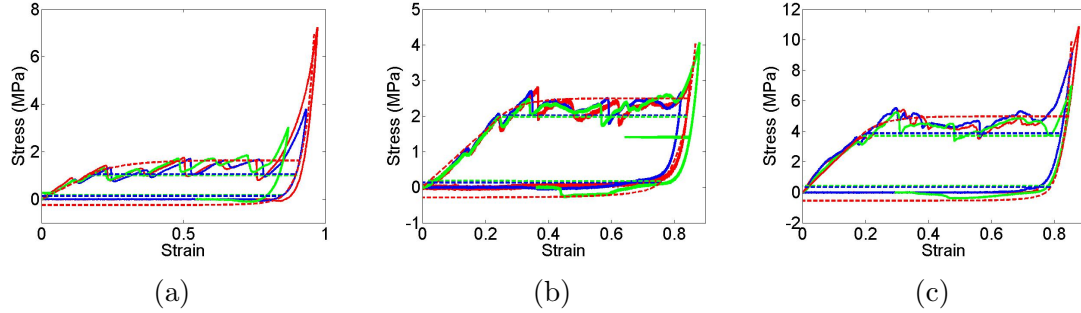
Figure 7.5: Compression stress-strain curves for three different strain rates 0.1 s^{-1}, 0.01 s^{-1}, and 0.001 s^{-1} (red, blue, and green solid line respectively) for (a) Bare CNT, (b) ALD 5 cycles, and (c) ALD 10 cycles pillars, respectively. Dashed lines are curves predicted by our phase transition model with parameters given in Table 7.1.

and ALD 10 cycles (Figure 7.3c) pillars. During initial loading, a flat surface between the punch face and the pillar top is created. Subsequently, the pillar undergoes elastic loading evident in the initial linear response of the stress strain curve. At a critical stress level, pillar scale buckling occurs, which is reflected in large softening events in the stress-strain curve. This pillar scale buckling propagates spatially along the pillar axis with nominally constant stress during the plateau region until it reaches the densification region. The stress rapidly rises in the densification region. The three loading regimes are indicated in Figure 7.3c by the highlighted circles. Snapshots of the deformation morphology from the three loading regimes are shown in Figure 7.3d.

While the stress-strain curves for the various sample conditions showed self-similar re-

sponse, images obtained during the compression tests indicate that the ALD coatings substantially altered the pillar scale deformation behavior. Beginning with the bare CNT samples, pillar scale buckling occurred at the top of the pillar and propagated entirely to the bottom as compression progressed. Buckling initiated at the top likely because the CNTs have more freedom to bend due to frictional interactions with the punch; in contrast, at the bottom they have less freedom since they are attached to the substrate. In such short CNT micropillars, I also expect that there is a density variation through the height, with a lower density at the top Park et al. (2013). However, Qiu et al. (2011) performed localized indentation and uniaxial compression experiments recently to show that coordinated buckling of CNT forests is most likely the result of the interplay between the rigid substrate and compliant forest and does not require variation in material properties through the height. Between the first and second buckling (or nucleation) events I could discern an interface marked by arrows in Figure 7.3b and 7.3c. Above this interface the CNT forests were densified, and below it they were rarefied. The first buckling event remained identical in coated samples. However, for the alumina coated pillars, another buckled region nucleated at the bottom following propagation of a portion of the first buckled zone. Notably, this second nucleation of pillar scale wrinkling was not clearly distinguishable in the stress-strain curve, signifying that the deformation mechanism during the plateau region remains the same.

We examined the effect of strain rate on the compressive stress-strain response as shown in Figure 7.5. Here, representative stress-strain curves for loading rates from 0.1 to 0.001 s^{-1} are shown in red blue, and green solid lines, respectively, for bare (Figure 7.5a), ALD 5 cycles (Figure 7.5b), and ALD 10 cycles (Figure 7.5c), all of which show some strain-rate dependence. However, the qualitative loading response was found to be self-similar regardless of the loading rate.

We used a digital image correlation (DIC) code Eberl et al. (2006) on the captured SEM images during the in-situ compression test to examine the local displacement and strains. The ALD 10 cycles pillar compressed with strain rate of 0.001/s was chosen for the DIC since this sample showed most reliable tracking due to its high contrast features. The SEM images were saved 1 per 2 seconds and the original SEM frame rate was 1 image per 1 second. I focused on the movement along the compression axis. A grid having a segment spacing of 250nm was used to monitor the displacement profile during pillar during compression. For this grid, nine global strain levels were selected and the results

120

Table 7.1: Fitting parameters of compression experiment on CNT forests.

Group	E (MPa)	B (MPa)	A (MPa)	σ_{LH} (MPa)	σ_{HL} (MPa)	M_{lh} (MPa^{-1}s^{-1})	M_{hl} (MPa^{-1}s^{-1})
ALD 10 cycle	20	1.37	1.36	3.7	0.5	0.09	0.12
ALD 5 cycle	8	0.61	0.60	2	0.2	0.5	0.3
Bare CNT	6	0.67	0.66	1	0	0.35	0.3

are plotted in Figure 7.4a. Dots of one color correspond to a particular global compressive strain. The profiles represented by dots of each color have roughly the same piecwise linear form depicted in the lower inset in Figure 7.4a. This piecewise linear displacement profile moves to the left as the global strain increases. An ideal strain profile corresponding to the piecewise linear displacement profile is shown in the upper inset. The strain discontinuity represents a sharp interface, or phase boundary, which moves to the left as the global strain increases. Motivated by this I used a 625 nm spaced grid to calculate local strains. Five levels of global strain were selected and the results are plotted in Figure 7.4b. The strain profiles in this figure are consistent with the idea of a moving interface.

7.4 CNT forests buckling viewed as a phase transition

In order to describe the CNT pillar compression process, I use a one-dimensional quasi-static version of the well-known Abeyaratne-Knolwes theory Abeyaratne & Knowles (2006) for phase transitions in continua. The discrete mass-spring model of Fraternali et al. (2011) with bi-stable springs can be thought of as a pre-cursor to our continuum model since it was shown in Purohit (2001) and Zhao & Purohit (2014) that the static and dynamic response of bi-stable chains is analogous to that of one-dimensional phase-transforming continua. In our continuum model the rarefied phase in which the CNTs are mostly straight is described by the stress-strain ($\sigma - \varepsilon$) relation:

$$\varepsilon = \Gamma_L(\sigma), \qquad 0 < \sigma < \sigma_M, \tag{7.1}$$

where σ_M is upper stress limit for the rarefied phase. While loading in compression, the densified phase nucleates at a stress $\sigma_{LH} < \sigma_M$, and is described by the stress-strain relation

:

$$\varepsilon = \Gamma_H(\sigma), \qquad \sigma_m < \sigma < \infty, \tag{7.2}$$

where σ_m is lower stress limit for the densified phase. Similarly, while unloading in compression, the rarefied phase nucleates at stress $\sigma_{HL} > \sigma_m$ (with $\sigma_{HL} < \sigma_{LH}$). Therefore, for $\sigma_m \leq \sigma \leq \sigma_M$, there are two possible stable phases corresponding to stress σ. I define a transformation strain $\gamma_T(\sigma)$ as:

$$\gamma_T(\sigma) = \Gamma_H(\sigma) - \Gamma_L(\sigma), \qquad \sigma_m \leq \sigma \leq \sigma_M. \tag{7.3}$$

We model the compression process of our CNT pillars as an one-dimensional initial-boundary-value problem of a continuum having the above stress-strain relation. I assume that the continuum extends along the x-direction and is confined to the interval $0 < x < L$ in the reference configuration. The displacement of a material point at reference position x is given by $u(x,t)$. The end at $x = 0$ is fixed so that $u(0,t) = 0$ for all t. At the end $x = L$ I apply a displacement boundary condition, so that $u(L,t) = \delta(t)$. I see that when the specimen is being loaded $\dot{\delta}(t) < 0$ and when it is being unloaded $\dot{\delta}(t) > 0$. The equation of motion for our one-dimensional continuum in the quasi-static setting is simply $\partial\sigma/\partial x = 0$, so that $\sigma(x,t)$ is constant for $0 < x < L$ at all t. So, the state of strain is: $\varepsilon = \Gamma_L(\sigma)$ if $\sigma < \sigma_M$ and $\varepsilon = \Gamma_H(\sigma)$ if $\sigma > \sigma_m$. If the stress σ is such that $\sigma_m < \sigma < \sigma_M$ then a mixture of phases is possible. Consequently, the elongation of the continuum is given by

$$u(L,t) = \delta(t) = \Gamma_H(\sigma(t))s(t) + \Gamma_L(\sigma(t))(L - s(t)), \tag{7.4}$$

where $s(t)/L$ is the fraction of material in the densified phase (see Figure 7.3). Note that if there was a single phase boundary separating the rarefied and densified phases (as is the case before the second nucleation event for all three types of CNT forest) then $s(t)$ denotes the position of the phase boundary in the reference configuration. Recall now that $\delta(t)$ is prescribed, but the evolution of $s(t)$ is as yet unknown. For describing the evolution of $s(t)$, which can be thought of as an internal variable, in this continuum theory I need a kinetic relation Abeyaratne & Knowles (2006). This kinetic relation is expressed in terms of the

some driving force f by the relation

$$\dot{s} = \Phi(f(t)), \tag{7.5}$$

where $\Phi(f)$ is a material property as in Abeyaratne & Knowles (2006). Now, I assume f is a unique function of σ, so the kinetic relation can be expressed as

$$\dot{s} = \bar{\bar{\Phi}}(\sigma). \tag{7.6}$$

Differentiating Eqn. (7.4) and eliminating $\dot{s}$ using Eqn. (7.6) I get the following equation relating $\sigma(t)$ and $\delta(t)$:

$$\left[p(\sigma) - \gamma'_T(\sigma)\frac{\delta}{L} \right] \dot{\sigma} + \gamma_T(\sigma)\frac{\dot{\delta}}{L} = \frac{\gamma_T^2}{L}\bar{\bar{\Phi}}(\sigma) \tag{7.7}$$

where

$$p(\sigma) = \Gamma_L(\sigma)\Gamma'_H(\sigma) - \Gamma'_L(\sigma)\Gamma_H(\sigma). \tag{7.8}$$

For given $\delta(t)$ Eqn. (7.7) can be integrated to get $\sigma(t)$. In our experiments $\dot{\delta}$ is typically a constant value for both loading and unloading.

7.5 Application to the CNT forests

We now write specific constitutive relations for the stress-strain response of the CNT forests given by Eqns. (7.1-7.2), and phase boundary kinetics in Eqn. (7.6). We assume that the stress-strain relation is linear in the rarefied phase as:

$$\sigma = E\varepsilon, \tag{7.9}$$

if $\varepsilon < \varepsilon_M = \sigma_M/E$, where E is a Young's modulus. In doing so I have assumed that the CNT forests behaves as a foam for which the stress-strain response at small strains can be computed in the terms of the properties of single fibers and the density of the network Cao et al. (2005), Zbib et al. (2008), Hutchens et al. (2010), Gibson & Ashby (1999). We point out, however, that density is not the only parameter that determines the Young's modulus of a CNT forest Torabi et al. (2014), Volkov et al. (2009); tortuosity (average curvature of

the CNTs) and connectivity (average number of contacts per unit length of CNTs) also play a role, although density dominates the overall modulus Qiu & Bahr (2013). In the densified phase, however, I will start with a non-linear power-law relation as given by Van Wyk (1946) and Toll (1998) as :

$$\sigma = kE\left(\phi^n - \phi_0^n\right), \tag{7.10}$$

where k is a coefficient around unity Mezeix et al. (2009), and n is derived to be 3 for three dimensional isotropic random networks Van Wyk (1946), Toll (1998), and also confirmed by several experiments Mezeix et al. (2009), Choong et al. (2013), Bouaziz et al. (2013), Masse & Poquillon (2013), Kim et al. (2016). While vertically aligned CNT forests may be better modeled as transversely isotropic materials, I do not do so here because such a model requires five constitutive parameters which are difficult to obtain from experiments. Furthermore, Hutchens et al. (2012) have demonstrated that an isotropic material model can capture the visco-plastic response quite well. In the above ϕ_0 is the volume fraction of fibers in the network when $\sigma = 0$ and ϕ is the current volume fraction of the fibers. They are related through the compressive strain ε as

$$\phi = \frac{\phi_0}{1 - \varepsilon}, \tag{7.11}$$

assuming that the cross-sectional area of our specimen does not change (as evident from the images in Figure 7.3). This stress-strain relation Eqn. (7.10) does not account for the possibility that fibers can adhere to one another when brought into contact Radhakrishnan et al. (2013), Torabi et al. (2014). In fact, a computational study by Torabi et al. (2014) has revealed that average number of contacts per unit CNT length, or connectivity, depends not just on the fiber volume fraction, but also on the growth process through the seed density (each CNT grows from a seed) and weakly through the cone angle (the limiting cone around link i within which the next link $i + 1$ of a growing CNT can lie). Here, in the interest of analytical tractability, I will account for fiber-to-fiber adhesion following Toll (1998) who shows that fiber contact point density scales with the square of the fiber volume fraction $N_c \propto \phi^2$. Assuming each newly formed contact point results in a bond which releases free energy U_{bond}, the bonding energy per unit volume is $E_{bond} = -C\phi^2 U_{bond}$, where C is a constant. I can add this contribution to the total strain energy stored in the network due to compression and then differentiate the resulting expression to get a new stress-strain law

124

in the densified phase that accounts for adhesion of fibers at contact points, yielding

$$\sigma = kE\left(\phi^3 - \phi_0^3\right) - \frac{2C\phi_0^2 U_{bond}}{(1-\varepsilon)^3} = \frac{B-A}{(1-\varepsilon)^3} - B, \qquad (7.12)$$

where $A = 2CU_{bond}\phi_0^2$, $B = kE\phi_0^3$ are two constants that are obtained by fitting to the experimental stress-strain curves in the densified phase. Finally,

$$\Gamma_L\left(\sigma\right) = \frac{\sigma}{E},$$
$$\Gamma_H\left(\sigma\right) = 1 - \sqrt[3]{\frac{B-A}{\sigma+B}}, \qquad (7.13)$$
$$\gamma_T\left(\sigma\right) = 1 - \sqrt[3]{\frac{B-A}{\sigma+B}} - \frac{\sigma}{E}$$

A similar exercise accounting for contacts with adhesion was also performed by Hutchens et al. (2012), but they simplified the resulting expressions to modify the visco-plastic hardening law in the plateau region of the stress-strain curve. I can use the results above to derive an expression for the driving force f in the quasi-static limit. I know from Abeyaratne-Knowles Gibson & Ashby (1999) that:

$$f(\sigma) = \int_{\sigma_0}^{\sigma} \gamma_T(\sigma')\,d\sigma', \qquad (7.14)$$

where σ_0 is a Maxwell stress. Recall that at the Maxwell stress the Helmholtz free energy density of the two phases is equal. The driving force f derived above enters a kinetic relation describing the evolution of the internal variable $s(t)$. For simplicity I will use the following kinetic relation:

$$\dot{s} = \Phi(f) = \begin{cases} M_{LH}(f - f_{LH}), & \text{if } f > f_{LH}, \\ 0, & \text{if } f_{HL} \leq f \leq f_{LH}, \\ M_{HL}(f - f_{HL}), & \text{if } f < f_{HL}. \end{cases} \qquad (7.15)$$

Here $M_{LH} > 0$ and $M_{HL} > 0$ are mobility parameters which I will later fit to the experimental data. Also, f_{LH} and f_{HL} correspond, respectively, to stresses σ_{LH} and σ_{HL} which may be determined using Eqn. (7.14). Our justification for choosing such a "stick-slip" type kinetic relation is as follows. We know from earlier work that thermal sliding of contacts between CNTs occurs when a CNT forest is compressed Radhakrishnan et al.

(2013), Mesarovic et al. (2007). Thermally activated processes are governed by Arrhenius type kinetics which can be linearized for small driving forces to give a linear kinetic law of the type $\dot{s} = Mf$ where M is a constant Abeyaratne & Knowles (2006). I also know from computations Torabi et al. (2014), Volkov et al. (2009) and experiments Qiu et al. (2011) that the CNTs reorient as the forest transforms from a rarefied phase to the densified phase. The kinetics of the reorientation is difficult to obtain, but it is clear that these processes produce a material that is heterogeneous at length scales much smaller than the specimen size. It has been shown that this sort of heterogeneity combined with a linear kinetic law at the microscopic scale leads to a stick-slip type of kinetic relation at the macroscopic scale Bhattacharya (1999). That said, the choice of kinetic relation above is not sacrosanct; the appropriate kinetic law should be deduced by fitting to experiment or nanoscale computations. The kinetic law, Eqn. (7.15), happens to fit the experiments described here quite well (as shown later).

In order to complete the formulation of the problem, I need a nucleation criterion. For loading, when the specimen is being compressed, the densified phase nucleates in the rarefied phase at stress σ_{LH} where σ_{LH} can be assumed to be where driving force f is just greater than f_{LH} so that the phase boundary makes its appearance and immediately moves. Similarly, for unloading, the rarefied phase nucleates in the densified phase at stress σ_{HL} where driving force f is just smaller than f_{LH}.

Now, the experiment is performed at a constant rate $\dot{\delta} < 0$ during loading. Initially, the entire continuum is in the rarefied phase. As the compressive strain ε increases, the stress σ increases linearly and reaches the critical value σ_{LH}; this is when a phase boundary nucleates at the top of CNT pillar ($x = 0$), with the densified phase on its top and the rarefied phase on its bottom. The stress in the continuum is now governed by Eqn. (7.7) with initial condition $\sigma = \sigma_{LH}$ given by the nucleation criterion. The kinetic relation enters the mechanics through $\bar{\Phi}(\sigma)$. The phase boundary moves through the continuum and converts all the material into the densified phase. Once the phase boundary has reached $x = L$, Eqn. (7.7), the nucleation criterion and the kinetic relation are no longer required. The stress is the determined by the constitutive law $\Gamma_H(\sigma)$ since all the material is in the densified phase. When I unload $\dot{\delta} > 0$, the stress declines along the curve $\Gamma_H(\sigma)$ until a critical value σ_{HL} is reached at which a phase boundary nucleates at $x = L$. Then $\sigma(t)$ is again governed by Eqn. (7.7) with initial condition $\sigma = \sigma_{HL}$. This differential equation

126

remains relevant until the phase boundary has traversed the full length of the specimen reaching $x = 0$. After this the stress follows the curve $\Gamma_L(\sigma)$ in the rarefied phase.

We have fitted the experimental data in Figure 7.3 from the measured loading and unloading response of three different samples using the methods described above. In Figure 7.3, the experimental data is represented by discrete markers and the model fit is shown as a continuous line. The strain rate $\dot{\delta}/L$ for these experiments was 0.001 s^{-1}. The parameters obtained from the fits are summarized in Table 7.1. Our phase transitions model captures the main features of the stress-strain curve quite well. The fitting parameters are E in the rarefied phase, A and B in the densified phase, σ_{LH} and M_{LH} for the upper plateau and σ_{HL} and M_{HL} in the lower plateau. The theoretical lines fall on top of the experimental data for the linear elastic response in the rarefied phase and the non-linearly elastic response in the densified phase. The plateaus in loading/unloading are also captured except for the stress-jumps seen in the loading plateau on which I will comment later. I note that the Young's moduli in the rarefied phase of the bare CNT pillar is the smallest. The Young's modulus in the rarefied phase increases as the thickness of the ALD alumina coating increases. Similarly, the stress at which the densified phase nucleates is also lowest for the bare CNT pillar and it increases as the thickness of the ALD layers increases. This is expected since increasing the thickness of the CNTs increases their stiffness causing an increase in the Young's modulus in the rarefied phase. In fact, this insight can be used to shed light on the microstructural components of the forests. For foams, $E \sim E_s \phi_0^2$ where E_s is the Young's modulus of a single fiber and ϕ_0 is the fiber volume fraction (see Gibson and Gibson & Ashby (1999)). In our bare CNT samples I estimate that the diameter of the CNTs is $d \approx 10$ nm and the spacing between adjacent CNTs is $D \approx 100$ nm, on average. Thus, $\phi_0 \approx (d/D)^2 \approx 0.01$. Thus, with $E = 6$ MPa for the bare CNT foam samples, I estimate that $E_{CNT} \approx 60$ GPa for one CNT fiber. This is smaller than the estimated Young's modulus of pristine CNTs, about 1 TPa, suggesting that our growth process produces CNTs with many defects. Similarly, I estimate that the fiber diameter in our ALD 5 cycle samples is about $d_5 \approx 1.1$ nm, and that in the ALD 10 cycle samples is about $d_{10} \approx 1.2$ nm (see section 2). If I assume that the Young's modulus of the ALD alumina coated fibers are $E_5 = E_{CNT} + E_{alumina}(1 - d^2/d_5^2)$ and $E_{10} = E_{CNT} + E_{alumina}(1 - d^2/d_{10}^2)$, then a similar calculation as above gives an estimate $E_{alumina} \approx 30$ GPa, which is again smaller than the measured value 180 GPa Tripp et al. (2006). The densified phase is nucleated when the fibers buckle. The critical stress σ_{LH} is

determined for foams from a knowledge of the buckling load of single fibers and the density of the network as was done in Cao et al. (2005). Hence, if the bending stiffness is higher due to increased thickness of the ALD layers then σ_{LH} also must increase. This is exactly what I see from our fits to the experimental data.

It is more difficult to physically justify the mobility parameters M_{LH} and M_{HL} that have been obtained by fitting our phase transition model to the experimental data. However, I can predict the stress-strain response in loading/unloading of the same samples at different strain rates $\dot{\delta}$. I have done this exercise for two other strain rates (0.01 s^{-1} and 0.1 s^{-1}) with the parameters shown in Table 7.1. The corresponding experimental stress-strain curves for these strain-rates are plotted together with the theoretical predictions in Figure 7.5. Remarkably, the agreement between theory and experiment indicates that the parameters I have obtained from fitting one set of experimental data are useful in describing the constitutive response of the material at other strain-rates as well. In particular, the nucleation stresses and our choice of the kinetic law gives a small strain-rate dependence of the hysteresis which is consistent with earlier experiments Pathak et al. (2012), Raney, Fraternali & Daraio (2013), Raney, Wang & Daraio (2013). If the motion of the phase boundary was independent of the stresses then our model would reduce to the rate-independent hysteresis models of Fraternali et al. (2011), Blesgen et al. (2012), Raney, Fraternali & Daraio (2013), Raney, Wang & Daraio (2013).

Finally, I point to an important feature that has not been captured by our phase transition model described above. Note in Figure 7.3 and Figure 7.5 that near a strain of 0.8 (which corresponds to most of the pillar being in the densified phase) the experimental loading and unloading curves are not identical at the end of unloading. This was observed in simulations of fiber networks by Barbier et al. (2009). and attributed to friction between contacting fibers. In our experiments, the increased contact between the CNTs in the densified phase exacerbates this effect. In fact, the loading and unloading curves in our nanoindentation experiments are also different, leading to dissipation. I quantify this dissipation in our analysis of the nanoindentation experiments by connecting it to the high density of contacts in the densified phase.

7.6   Stress jumps at the plateau

Our constitutive model yields a plateau in the stress-strain curve that is smooth. This is not what I see in experiments. In fact, the stress-plateau in the experimental data invariably has a few jumps in the stress (shown in Figure 7.5 for various strain rates), which are caused by nucleation of the densified phase away from the moving phase boundary. In this section I will quantify these jumps using energetic arguments. Nucleation events create new interfaces between the rarefied and densified phases, which are characterized by an interfacial energy U_{inter}. We require that the change in Gibbs free energy of the two phases during a jump should equal the energy U_{inter} as:

$$\Delta s \left[G_L\left(\sigma_2\right) - G_L\left(\sigma_1\right)\right] - \Delta s \left[G_H\left(\sigma_2\right) - G_H\left(\sigma_1\right)\right] = U_{inter}, \tag{7.16}$$

where the subscript $1, 2$ indicates variables before and after the jump, respectively, and $\Delta s = s_2 - s_1$, and G is the Gibbs free energy per unit reference length which is given by $G = W - \sigma\varepsilon$. In the equation above L in the sub-script denotes the rarefied phase and H denotes the densified phase. From Abeyaratne-Knowles theory Abeyaratne & Knowles (2006), the driving force across an interface (given by f in Eqn. (7.14)) is simply the jump in Gibbs free energy density across it. Hence, the equation above reduces to:

$$\Delta s \left[f\left(\sigma_2\right) - f\left(\sigma_1\right)\right] = U_{inter}. \tag{7.17}$$

For each jump the phase fraction also changes and I can estimate the phase fractions from the strains before and after the jumps using:

$$
\begin{aligned}
s_1 &= \frac{\varepsilon_1 - \Gamma_L(\sigma_1)}{\Gamma_H(\sigma_1) - \Gamma_L(\sigma_1)}, \\
s_2 &= \frac{\varepsilon_2 - \Gamma_L(\sigma_2)}{\Gamma_H(\sigma_2) - \Gamma_L(\sigma_2)}.
\end{aligned}
\tag{7.18}
$$

Using Eqns. (7.14), (7.17), and (7.18), I am able to estimate U_{inter} from the experimental data $\sigma_1, \sigma_2, \varepsilon_1, \varepsilon_2$ for all visible stress jumps in Figure 7.5. I present the results in Table 7.2. Next I am going to relate the obtained interfacial energy U_{inter} and phase fraction change Δs with the strain profiles obtained by digital image correlation as described below.

The above analysis assumed that the interface is sharp (a discontinuity in strain $\varepsilon(Z)$),

but in experiments the interface is diffuse with a continuous $\varepsilon(Z)$. Diffuse interfaces are characterized by an interfacial energy that can be written as:

$$U_{inter} = \lambda \int_{-\infty}^{\infty} \left(\frac{d\varepsilon}{dZ}\right)^2 dZ, \tag{7.19}$$

where λ is a constant. As $\lambda \to 0$, the interface becomes sharp. I want to check if our estimates of the interfacial energy obtained from the sudden nucleation events can be correlated with the diffuse interfaces seen in experiments on CNT forests. Such diffuse interfaces in a quasistatically loaded specimen are often modeled as traveling waves moving at velocity V_m in viscosity-strain gradient theories of phase boundary motion Abeyaratne & Knowles (2006). If the stress-strain relation of our CNT forests is modeled as a cubic $\sigma - \sigma_0 = \alpha(\varepsilon - \varepsilon_*) - \beta(\varepsilon - \varepsilon_*)^3$ then a viscosity-strain gradient model Abeyaratne & Knowles (2006) with $V_m = 0$ gives a differential equation for $\epsilon(Z) = \varepsilon(Z) - \varepsilon_*$:

$$\lambda \frac{d^2\epsilon}{dZ^2} + \alpha\epsilon - \beta\epsilon^3 + \sigma - \sigma_0 = 0. \tag{7.20}$$

The solution to this differential equation is

$$\epsilon(Z) = \varepsilon(Z) - \varepsilon_* = a + b\tanh(\frac{Z - Z_0}{c}), \tag{7.21}$$

when the remote conditions at $\pm\infty$ are constant strains $\varepsilon(\infty) = a + b$ in the densified phase, and $\varepsilon(-\infty) = a - b$ in the rarefied phase. The width of the interface, $2c$, is related to λ through $c^2 = 2\lambda/\left(\beta b^2\right)$. I fit the experimental strain profiles $\varepsilon(Z)$ for the 10 ALD cycles pillars in the Figure 7.4b using Eqn. (7.21) and obtain $a = 0.31$, $b = 0.3$, $c = 0.2$ μm. This is a relatively sharp interface, consistent with the displacement profiles shown in Figure 7.4a. Using the values of b and c from this fit I computed an interfacial energy $U_{inter} = 0.17$ J/m^2 from Eqn. (7.20), which agrees very well with the result from the analysis of stress jumps summarized in Table 7.2. We performed similar calculations on the CNT compression experiments in Maschmann et al. (2012) and obtained $a = 0.315$, $b = 0.3$, $c = 2$ μm from fits to the experimental strain profiles in Figure 5(b) of Maschmann et al. (2012). From these values I computed an interfacial energy $U_{inter} = 0.72$ J/m^2 which is in the same range as $U_{inter} = 0.14 \pm 0.09$ J/m^2 obtained by applying our procedure above to the jumps in the stress-strain curves in Figure 5(a) of Maschmann et al. (2012).

For comparison, the interfacial energy for a graphite-graphite interface is around 0.2 J/m^2 Zacharia et al. (2004), for an ice-water interface it is 0.041±0.009 J/m^2 Jones & Chadwick (1970), for an In-Bi interface it is 0.047±0.005 J/m^2 Akbulut et al. (2008), and for a Zn-Sn interface it is 0.106±0.009 J/m^2 Keşlioğlu & Maraşlı (2004). Hence, our estimates of U_{inter} for the CNT forests studied in this manuscript seem robust.

The interface width, $2c$, is directly proportional to the buckling wavelength. According to Zbib et al. (2008) the presence of this buckling wavelength indicates that a continuum model with an intrinsic material length scale is required to model CNT forests. How this internal length scale depends on statistical parameters of the CNT forest was investigated by Torabi et al. (2014) who showed that the buckling wavelength depends on tortuosity K, density l and connectivity γ (these are symbols used in Torabi et al. (2014)) in the undeformed state. They deduced an empirical relation $c\sqrt{l} = \beta_1 + \beta_2\gamma/K$ where β_1, β_2 are constants. On the other hand, the buckling stress σ_b in Torabi et al. (2014) increased linearly with increasing l and was only weakly dependent on γ/K. Thus, I expect from Torabi et al. (2014) that c should vary inversely with σ_b. Now, in our CNT forests with 10 ALD cycles c = 0.2 μm and $\sigma_b \approx 4.5$ MPa (for bare CNT forests $\sigma_b \approx 1.3$ MPa), while in Maschmann et al. (2012) $c = 2$ μm and $\sigma_b \approx 0.6$ MPa. The inverse relationship between σ_b and Δs (Δs is proportional to c) can also be seen in Table 7.1 and 7.2. Thus, our results for trends in c vs. σ_b are consistent with those of Torabi et al. (2014). I relate c to an interfacial energy between the rarefied and densified phases, while Torabi et al. (2014) relate c to tortuosity, density and connectivity, all of which should increase as I cross the interface from the rarefied to the densified phase. Intuitively, these two descriptions of the intrinsic length scale are not unrelated – interfacial energy arises because the environment of a material point on the two sides of an interface are different Israelachvili (2011). A final point to note is that our interfacial energy depends on the square of the strain-gradient in Eqn. (7.19). Strain-gradient elasticity theories Toupin (1962), Koiter (1964), Mindlin & Eshel (1968) in which the elastic energy depends quadratically on both strains and strain-gradients naturally have intrinsic length scales.

Table 7.2: Stress jumps and interfacial energy values fitted from the data.

Group	Number of jumps studied	Δs (μm)	U_{inter} (J/m^2)
Bare CNTs	9	0.27±0.09	0.13±0.04
CNTs with 5 ALD cycles	6	0.21±0.1	0.11±0.05
CNTs with 10 ALD cycles	8	0.20±0.16	0.12±0.10

7.7 Indentation of CNT forests

The experiments and analysis discussed thus far have resulted in a micro-structurally motivated continuum model based on the mechanics of foams and the theory of phase transitions. Our goal now is to test this model by using it to interpret nanoindentation experiments (Figure 7.2d) on the same materials.

The nanoindentation experiments were performed using a Hysitron$^®$ TI-950 Triboindenter^{TM}, fitted with a conical diamond indenter tip with spherical end. As shown in Figure 7.2d, the indenter has a radius of about 1μm and an included angle of 90°, which is much smaller than the height and diameter of the CNT pillars (both 20 μm). I performed a series of loading and partial unloading tests with controlled peak load as shown in Figure 7.6a. Specially, there were 10 cycles of loading and unloading at each location. In each cycle, except the last cycle, the load was ramped up to a certain peak load in 2 s and then unloaded to 5% of its peak load in another 2 s (see Figure 7.6a inset). In the last cycle, the sample was fully unloaded and the indenter was completely withdrawn from the surface. The peak load was increased uniformly from 5μN up to 50μN. Three different samples, i.e. bare CNT, 5, and 10 cycles of ALD coated CNT pillars, were measured. For each material, 6 different pillars were tested. The indentation tests were always performed at the center of each individual pillar. Force-displacement curves were collected during experiments. One such curve is shown as the black solid line in Figure 7.6a. Notice that there is hysteresis in each cycle of loading/unloading and it increases at larger forces. This is true for bare CNT, as well as ALD 5 cycles and 10 cycles pillars. Also notice that the residual displacement at zero load at the end of each cycle keeps increasing as the peak load increases. I show below that such a result is a consequence of the phase transition in the CNT forest.

Table 7.3: Fitting parameters of nanoindentation experiment.(The error-bars account for distinct nanoindentation groups.)

Group	Bare CNT	ALD 5 cycles	ALD 10 cycles
z_0 (μm)	1.8	1.38	1.06
E_1 (MPa)	6.14$\pm$0.42	5.44$\pm$1.01	13.30$\pm$1.11
E_H (MPa)	38.82$\pm$0.89	62.76$\pm$1.58	111.11$\pm$2.33
γ_T (indentation)	0.562$\pm$0.007	0.655$\pm$0.044	0.362$\pm$0.026

7.8 Point load on a half-space capable of phase transitions

We will now show that our phase transition model can also be applied to nanoindentation experiments on these CNT pillars. Since the indenter is small compared to the sample size (1/20), I will approximate its response using the Boussinesq solution for a half-space with a point-load as in Craig (2013). The load is applied perpendicular to the surface of the half-space and the displacement underneath the load is given by:

$$u = \frac{3P}{2\pi E z},\tag{7.22}$$

where P is the applied point load, z is reference depth to surface and E is a reduced modulus with effect of Poisson ratio absorbed. The stress distribution $\sigma(r,z)$ within the half space for this axis-symmetric problem is given by:

$$\begin{aligned}
\sigma_z &= \frac{3Pz^3}{2\pi R^5}; \\
\sigma_r &= \frac{P}{2\pi R^2}\left[\frac{3r^2 z}{R^3} - \frac{(1-2\nu)R}{R+z}\right]; \\
\sigma_\theta &= \frac{(1-2\nu)P}{2\pi R^2}\left[\frac{R}{R+z} - \frac{z}{R}\right]; \\
\tau_{rz} &= \frac{3Prz^2}{2\pi R^5}.
\end{aligned}\tag{7.23}$$

where r is reference radius in the polar coordinate system, and $R = \sqrt{r^2 + z^2}$. This solution is valid for infinitesimal strains and isotropic linear elastic materials. But, the CNT forests I study are capable of phase transitions. Hence, underneath the applied load, where the stresses are very large, I expect that the CNT forests will be in the densified phase as

133
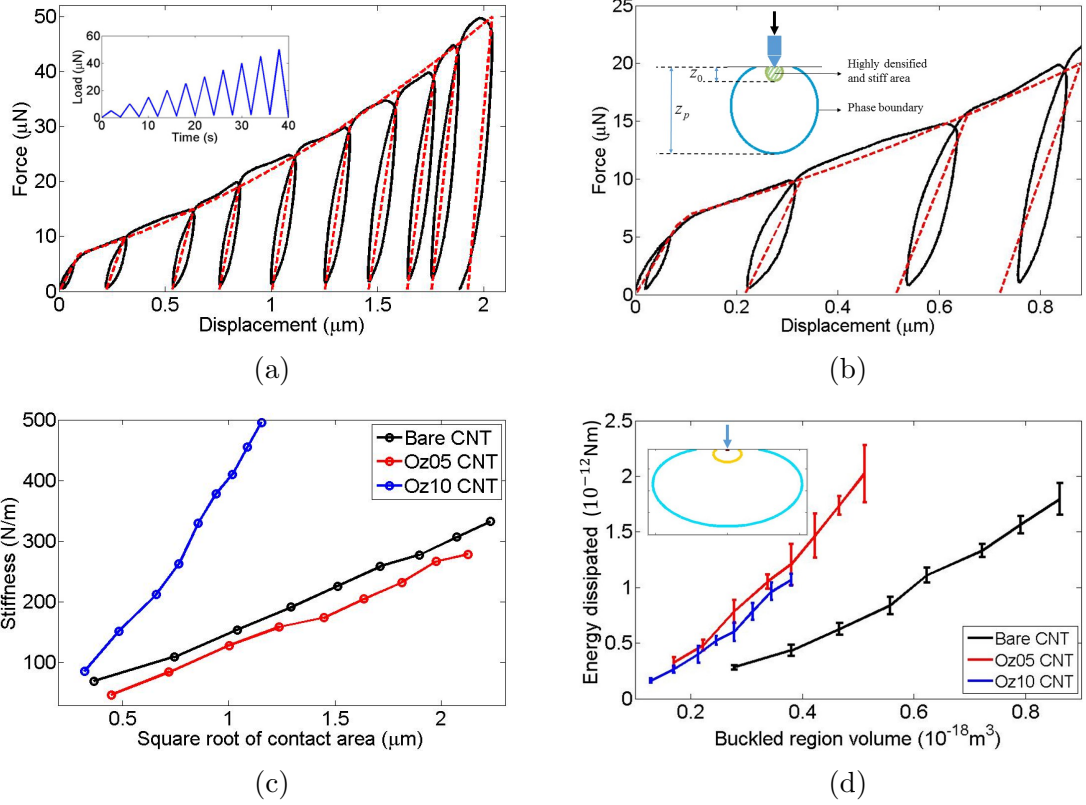
Figure 7.6: (a) Force-displacement curve for bare a CNT pillar in a nanoindentation experiment (black solid line). Hysteresis increases with increasing load. The red dashed lines are fits obtained with a combination of the Bussinesq solution and phase transition model, using distinct values of reduced Young's modulus for each cycle. The inset shows the scheme of loading and unloading cycles in our nanoindentation experiment. (b) Prediction of second, third and fourth cycles from Eqn. (7.26) using parameters for bare CNT pillars obtained from the first cycle. The extracted parameters are reported in Table 7.3. (c) The slope of the load indentation curves during unloading depends linearly of $E\sqrt{A}$ where E is a reduced modulus and A is the contact area of the indenter. (d) Plot showing hysteresis in nanoindentation experiments is linear in the volume of the densified region. The error bars are standard deviation from six distinct experiments. The inset is a figure showing cross-sectional view of the axis-symmetric phase boundary determined using Eqn. (7.25) at two different loads. The network inside the phase boundary is in the densified phase.

shown in Figure 7.2a. In order to accommodate this possibility I replace Eqn. (7.10) in the densified phase with a linearized version $\Gamma_H(\sigma) = \gamma_T + \sigma/E_H$, where the stiffness E_H in the densified phase is much larger than that in the rarefied phase. One way to obtain E_H would be to linearize the stress-strain curve in the densified phase at an appropriate strain ε, but it is not clear which ε to use since the strains vary all over the sample. Hence, I obtain E_H by fitting the last cycle of unloading in the indentation experiments in which

the compressive load is so large that I could assume the CNT forests is densified over a large volume underneath the load. This simplifying assumption enables us to exploit the Boussinesq solution. Eqn. (7.22) for the displacement underneath the point load is modified by adding the effect of the transformation strain γ_T as:

$$u = \frac{3P}{2\pi E z} + \int \gamma_T \mathrm{d}z, \tag{7.24}$$

where the limits of the integral are determined by the position of the phase boundary between the densified and rarefied phases and E depends on the Young's moduli in both phases. The boundary location (r, z) for given P is determined by setting σ_z (from Eqn. (7.23)) equal to a critical stress of nucleation σ_C, or:

$$3Pz^3 = 2\pi\sigma_C \left(r^2 + z^2\right)^{\frac{5}{2}}. \tag{7.25}$$

This critical stress σ_C is taken to be σ_{LH} in compression. As the load increases, the phase boundary will move deeper into the half space, and thus the region containing the densified phase will increase its volume as shown in the inset of Figure 7.6d. In this inset the yellow and blue curves show the position of the phase boundary for low and high load, respectively. There is a jump in strain across this phase boundary, but there is no jump in stress since the phase boundary moves in a quasi-static manner. Since the expressions in Eqn. (7.23) for the stress field do not involve the Young's modulus and I assume that the material is linear elastic in both phases, they are valid on both sides of the phase boundary. Eqn. (7.24) above has a singularity in the displacements at $z = 0$. This happens because linear elasticity is not a valid model near $z = 0$. In order to circumvent this difficulty I choose a reference position z_0 to calculate displacements u (in Eqn. (7.24)) such that at a critical load when the densified phase nucleates, $\sigma_z(z_0) = \sigma_c$, where this critical stress $\sigma_c = \sigma_{LH}$, obtained from fitting the uniaxial compression data. I assume that the CNT forests above this reference position z_0 is in a highly densified and stiff state due to large stresses. Hence, the displacement at z_0 will be nearly equal to the displacement underneath the indenter. We are now in a position to calculate load-displacement curves which can be fit to the experimental data.

In the experiments each sample is loaded and unloaded in a cyclic manner according to the protocol shown in the inset of Figure 7.6a. In the first cycle the load is increased

135

at a constant rate up to P_1, and then it is decreased to nearly zero at a constant rate. In the second cycle the same protocol is followed but the maximum load is $P_2 > P_1$. In the third cycle the maximum load is $P_3 > P_2$, and so on for all subsequent cycles. A typical load indentation curve is plotted in Figure 7.6a as the black line. Notice that there is a change in the slope of the line at $P \approx 8\mu N$, due to softening, presumably caused by the phase transition. I determine z_0 for this sample by setting $\sigma_z(z_0) = \sigma_c$ at $P \approx 8\mu N$. σ_c are chosen based on the nucleation stress σ_{LH} in Table 7.2, respectively, for the three different CNT pillars, and the calculated z_0 are reported in Table 7.3. For $P > \approx 8\mu N$ the phase boundary moves to $z_p > z_0$ along the line $r = 0$. During unloading, the phase boundary does not move inward because of our choice of the kinetic relation and also because the nucleation stress for the rarefied phase is very small as can be seen in Table 7.1. Hence, the phase boundary remains static and the region inside is unloaded along the stress-strain curve of the densified phase. Therefore, the slope of the re-loading curve is larger than the initial loading curve. In order to quantitatively predict this behavior I utilize Eqn. (7.23) to obtain the strain distribution. Note that outside phase boundary the Young's modulus is E_1, while inside it is E_H. So, by integrating ε_z with respect to z along the center line $r = 0$ and realizing that the Young's modulus for $z > z_p$ is E_1, while that for $z < z_p$ is E_H, where z_p is the position of the phase boundary at $r = 0$, I get

$$u = \frac{3P}{2\pi}\left(\frac{1}{E_1 z_p} + \frac{1}{E_H z} - \frac{1}{E_H z_p}\right) + \int \gamma_T \mathrm{d}z. \tag{7.26}$$

As a result, the equivalent reduced modulus E of Eqn. (7.24) extracted from Eqn. (7.26) is some value between E_1 and E_H. This equivalent reduced modulus depends on z_p, the position of the phase boundary. I show in the Appendix Table 2 that z_p does not change much if I compute it using the Hertz contact solution for a paraboloid indenter, although I have used the point load solution here. In particular, z_p increases by the same amount as I go from one peak load to the next (say P_2 to P_3) in the Hertz solution and the point load solution. When the load is reduced to zero, there is some residual deformation due to the transformation strain γ_T in Eqn. (7.26) above. When the load is increased again the phase boundary moves outward only when the load exceeds P_1, and it stops when $P = P_2$. Hence, I can compute the new z_p and a new reduced modulus for the second re-loading curve. By following the same procedure for all the loading/unloading cycles I

can predict the reduced moduli for all the re-loading, as well as the entire load-indentation curves. The result of this exercise is shown in Figure 7.6b for the bare CNT pillar in the first four cycles as the red dashed lines. The fitting parameters are tabulated in Table 7.3 for three different samples. I see that the values of E_1 are close to E obtained from fitting the uniaxial compression data. The transformation strains γ_T are close to the magnitude of the strain jumps at the stress plateaus for each of the three types of CNT pillars and the trend in the E_H values indicates that the Young's modulus in the densified phase increases as the ALD alumina coating thickness increases. In the appendix I use a linear stress-strain relation for the densified phase to refit the uniaxial compression experimental data and obtain Young's modulus of both rarefied and densified phases E_L, E_H respectively, and transformation strain γ_T. I compare them with the same parameters extracted from fitting the nanoindentation experiments and find that all of them are consistent. This shows that the same phase transition model can quantitatively describe both uniaxial compression as well as nanoindentation experiments.

In Figure 7.6b, the red dashed lines (model) show good agreement with the experimental data for only the first few cycles of loading and unloading. The discrepancy between the prediction and experiments increases in the following cycles. In these cycles, the point load assumption becomes invalid as the contact depth and contact area increase. In order to quantitatively account for this I follow the work of Oliver & Pharr (1992) which shows that $S \propto E_r\sqrt{A}$, where S is the stiffness of each cycle, E_r is reduced modulus and A is the contact area which depends on the contact depth and indenter's geometry through:

$$A = \begin{cases} \pi\left(2Rd - d^2\right), & d < \left(1 - \frac{\sqrt{2}}{2}\right), \\ \pi\left[\left(\sqrt{2} - 1\right)R + d\right], & \text{otherwise.} \end{cases} \tag{7.27}$$

Here d is the displacement at the peak load for each cycle and R is the indenter radius. I plot the reduced modulus E from phase transition model vs $S/\sqrt{A}$ for the three different samples in Figure 7.6c. I find that dependence is linear. The proportionality constants extracted are respectively 0.1091 for bare CNT pillars, 1.5976 for the ALD 5 cycles pillars, and 8.5554 for ALD 10 cycles pillars. The proportionality constant is affected by (a) the material, (b) the indenter shape, and (c) the sample geometry (it is not a half-space).

7.9 Hysteresis in the nanoindentation experiments

In the nanoindentation experiments I also observe hysteresis in the cyclic loading/unloading of the CNT pillars as shown in Figure 7.6. This cannot be captured by the linear elastic Boussinesq solution given above. However, it is possible to make some estimates of the hysteresis magnitude. A few papers claim that the energy dissipation can be attributed to the friction and viscous dissipation caused by the airflow during loading and unloading Kumar et al. (2015), Davami et al. (2016). From the poro-viscoelasticity theory of foams Kim et al. (2016), Gibson & Ashby (1999), the stress due to air flow during compression is given by:

$$\sigma = \frac{\mu \dot{\varepsilon}}{1 - \varepsilon} \left(\frac{D}{l} \right)^2, \tag{7.28}$$

where ε and $\dot{\varepsilon}$ are the compressive strain and its rate, D is the horizontal dimension of the CNT pillars, l is distance between single CNTs, and μ is the dynamic viscosity of the air. If I plug experimental parameters into Eqn. (7.28), the resulting stress is very small and hence unlikely to be a major source of dissipation. I therefore think that the hysteresis has its origins in friction between fibers at the large number of contacts created in the densified phase. The density of contacts is related to fiber volume fraction as in Van Wyk (1946) $N_c \propto \phi^2$. Since the stress-strain curve in the densified region is steep the strain does not vary much over the volume of the densified region. Thus, I can approximate the fiber volume fraction and the density of inter-fiber contacts in the densified region as nearly constant. Under these circumstances the energy dissipated due to inter-fiber contacts should scale linearly with the volume of the densified region in our samples (which evolves with load as shown in the inset of Figure 7.6d). I can compute the volume of the densified region as a function of load in the indentation experiments using our phase transition model described above and plot the hysteresis as a function of this volume. The plot in Figure 7.6d confirms that the hysteresis does indeed vary linearly with the volume of densified region confirming our hypothesis that inter-fiber friction is responsible for the dissipation. Note also that for the same volume of the densified region the energy dissipated is much larger for the ALD alumina coated CNT pillars than for the bare CNT pillars. The likely cause is the rough surface morphology of the alumina coated CNTs.

Chapter 8

Conclusions

In **Part I** of this thesis we deal with flexible two-dimensional systems undergoing thermal fluctuation. In **Chapter 2** we proposed a new approach to compute the partition function of a thermally fluctuating lipid membrane. This approach, based on the discretization of the membrane into equilateral triangles, deviates from many computational/simulation methods which start from a similar discretization in that we compute the partition function using Gaussian integrals. Our method can accommodate any type of boundary condition and is not limited to homogeneous membranes. Furthermore, since it is based on triangular elements, a wealth of knowledge from the field of computational mechanics of shells can be brought to bear on membrane fluctuation problems through our techniques. An advantage of our method is that we can compute membrane free energies for only a modest computational cost; these are otherwise computationally intensive to calculate using Monte Carlo or TDGL methods. The disadvantages of our method are that we are restricted to (a) fluctuations small enough that there are no overhangs in the membrane (similar to the Monge gauge), and (b) quadratic Hamiltonians. On the other hand, Monte Carlo methods can handle large deformations including overhangs and self-contact, as well as non-quadratic Hamiltonians.

In **Chapter 3** we generalize our idea to compute the partition function of a thermally fluctuating solid membrane, especially graphene. We account for the non-linear coupling of in-plane strains and out-of-plane deflections using a penalty method. Once the partition function of the fluctuating membrane is known, several thermodynamic quantities can be determined by calculating its derivatives. We have utilized this idea to illuminate

how loading and boundary conditions affect the fluctuation profile (or ripples) of graphene sheets. We have also shown that our method can quantitatively explain the dependence of the negative thermal expansion coefficient of graphene on temperature. We have made predictions for how shear loads can affect the thermal expansion coefficient that can be tested in experiments. Our method can be used to make quantitative predictions for other two dimensional materials.

In **Chapter 4** we apply our finite element plate model and semi-analytic computational method to determine the conditions under which elastic and entropic forces on inclusions in membranes can conspire to produce a maximum in the free energy landscape. It was known from earlier work that the elastic interactions between two inclusions decreases, and the entropic interaction increases, as the separation between them increases. The lowest order term in the elastic energy scales as $K_b \psi_A^2$ where K_b is the membrane bending modulus and ψ_A is the contact angle between the inclusion and the membrane; the lowest order term in the entropic part of the free energy scales as $k_B T$. We find that for large values of $K_B \psi_A^2$ the elastic energy completely dominates the entropy and we do not see local minima or maxima in the free energy landscape. However, for membranes whose bending modulus is in the 1 $k_B T$ range (e.g. some surfactant monolayers Rekvig et al. (2004)) or for very low contact angles ψ_A the elastic and entropic interactions can balance each other and produce a local maximum at spacing r_{cr} in the free energy landscape. For separtations greater than r_{cr} the bending energy dominates and the inclusions repel each other, but for separations smaller than r_{cr} entropy dominates and the inclusions will attract. In such a scenario, the preferred spacing between the inclsions will be dictated by short-range interactions. We have shown that this is true not just for two interacting inclusions, but also for a cluster of inclusions. The interactions between the inclusions described here fall under the category of 'curvature mediated' interactions. Interactions between inclusions in lipid membranes can arise also due to bilayer thickness mediated interactions. We have not considered this second set of interactions here, but we know that they too can lead to a preferred lattice spacing between inclusions on a lipid membrane as summarized in recent work by Kahraman et al. (2016). This work minimizes an energy that is quadratic in u/a and its gradients where $u(x,y)$ is half the bilayer thickness and a is half the unperturbed bilayer thickness. We believe that our methods of computing the partition function summarized here can be extended to this type of energy. Such a modification would more accurately capture the physics of

interactions between inclusions in a lipid bilayer. Another important ingredient that leads to a preferred spacing between inclusions, such as proteins, on membranes is the interfacial energy at the protein's boundary with the membrane as shown by Agrawal et al. (2016). In the work of Agrawal et al. (2016) the interfacial energy is assumed to depend quadratically on the jumps in displacement and slope at the protein-membrane boundary and moduli characterizing this interfacial energy are extracted from molecular simulations of proteins embedded in lipid membranes. Once again, since the energies in this method are also quadratic in the displacements or its gradient our technique can potentially be applied to obtain entropic corrections.

In **Part II** of this thesis we deal with foam-like densification of fiber networks under compression. In **Chapter 5** we have shown that fibrin networks are natural cellular materials. The theoretical description of the fibrin mechanical behavior is novel and treats fibrin networks in the context of a broad class of natural and synthetic foam-like materials which share some key features. Among these is the tri-phasic stress-strain response with a rarefied low-strain phase, a densified high-strain phase, and a plateau phase consisting of a mixture of these two. Like most foams we also see a moving phase boundary separating the two phases when fibrin networks are compressed Gaitanaros et al. (2012), Jang & Kyriakides (2009). The phase boundary and several other features quantifying the structural non-uniformity of fibrin networks under compression were revealed by collaborative three-dimensional microscopy studies. Because of the complexity of the analysis, non-uniform fibrin networks under loads have not been previously quantified. However, it is clear that under physiological conditions fibrin networks are frequently exposed to dynamic forces, which could result in non-isotropy and structural heterogeneities. Since in many cases, fibrin networks participate in the permeation of blood clotting factors Kim et al. (2013) variations in fibrin matrix density can affect the spatial-temporal distribution of factors and hence, alter their biochemical interaction. Our results indicate that even a uniform compression can produce structural gradients in fibrin networks, therefore, suggesting a non-uniform alteration of fibrin matrix transport properties with compression.

In **Chapter 6** we summarize an experimental and theoretical study of the compression response of PPP clots, PRP clots and whole blood clots. Our collaborators measure the compression stress-strain curves together with the evolution of clot structure using a custom built apparatus that combines a rheometer and a confocal microscope. Our observations of

the fluorescence intensity of compressed clots as a function of depth reveals that a front, or phase boundary, propagates through the sample. On one side of this phase boundary the fibrin network is in the rarefied phase with mostly straight fibers, and on the other side the network is in the densified phase with buckled fibers and numerous contacts. The width of the phase boundary depends on the rate of compression – it is small (sharp phase boundary) for low strain rates and large (diffuse phase boundary) for high strain rates. The propagation of this boundary through the sample is the basis of our phase transitions based model to describe the compressive behavior of blood clots. We propose an analytic model based on phase transitions which accounts for the coexistence of rarefied and densified fibrin networks to analyze the experimental results described above. We account for the adhesion of fibers in the densified phase and the presence of platelets through a pre-stress in the rarefied phase. The pumping of liquid through the clot during compression also contributes a stress which is modeled using an expression from the foam literature. The deformation of red blood cells makes a major contribution to the stress in whole blood clots and we account for this using classical expressions based on a neo-Hookean constitutive law for these cells. We also propose a simple model to capture the shear storage and loss moduli as a function of compressive strain. The position of the phase boundary is an input to this model which is obtained from our phase transition theory.

Finally, in **Chapter 7** we show that the same model for phase transitions in continua can also describe the deformation of CNT forests both in uniaxial compression and nanoindentation experiments. We have used specialized constitutive laws in the rarefied and densified phases that are based on the bending of individual fibers. We have modified well-known models for the compression of fiber networks in the densified phase to account for sticking of the fibers. We have shown that hysteresis in the indentation experiments likely has its origins in inter-fiber friction. Some features in our model, such as, rate-dependence and fiber-to-fiber adhesion are also present in the models of Hutchens et al. (2010, 2012), but we describe reversible deformations with hysteresis, while Hutchens et al. (2010, 2012) focus on irrecoverable deformation. Our model also shares some features with those of Fraternali et al. (2011), Blesgen et al. (2012), such as, the multi-well energy landscape of the springs. However, ours is a continuum model which can be used to study a broader class of materials and mechanical behaviors. As an example, our collaborators have performed experiments on ALD alumina coated CNT pillars and we have shown how their mechanical parameters

are affected by ALD coating thickness.

In conclusion, in my thesis we have applied knowledge from solid mechanics, statistical mechanics, thermodynamics, and the finite element method to theoretically study the thermal and mechanical properties of common systems in biology and materials science. We collaborate with experimental colleagues and apply a model of phase transitions to fibrin networks, blood clots, and CNT forests. Our studies in both topics could eventually be used to inform further research in the mechanics of cells and tissues, as well as design of biomaterials and CNT foam materials for optimizing desired mechanical properties.

Appendix

Structure of the Compression Front

In our analysis above I assumed that the compression front is sharp. However, our experiments reveal that it has a thickness over which there is a large gradient in the strain profile. Fortunately, these descriptions are connected and have been discussed at length in the literature Abeyaratne & Knowles (2006). Recall that I fitted the strain profile in our compressed sample using Eqn. (5.1). In the following, I briefly describe why I use the strain profile given by Eqn. (5.1). I follow the analysis in Abeyaratne & Knowles (2006). Our network can exist in multiple phases at the same stress. Such materials have an up-down-up type stress-strain curve that can be described using

$$\sigma - \sigma_0 = -\alpha(\varepsilon - \varepsilon_*) + \beta(\varepsilon - \varepsilon_*)^3, \tag{1}$$

where σ is the stress, ε is the strain, and α, β, σ_0 and ϵ_* are material parameters. If we remember that $\sigma = \partial W / \partial \varepsilon$, where $W(\varepsilon)$ is a stored energy function, then it is not difficult to see that W is a quartic function of ε with two wells. The well at low strains corresponds to a network in which the fibers are straight, while the well at high strains corresponds to a densified network with buckled fibers. Without loss of generality I will now refer to $\sigma - \sigma_0$ as σ and to $\varepsilon - \varepsilon_*$ as ε. As an example, $\sigma_0 = 5$ Pa, $\epsilon_* = 0.32$, $\alpha = 51$ Pa and $\beta = 651$ Pa captures the compression curve for $E_s = 5$ MPa in Figure 1a. In Figure 1b I have plotted the Gibbs free energy density ($\Psi = W - \sigma\varepsilon$) landscape using the above parameters for three different values of σ to show which phase has lower energy at each stress. Since the motion of the compression front causes energy dissipation I augment this constitutive equation with a linear viscosity term and since interfaces cost energy I add a linear strain

gradient term as follows Abeyaratne & Knowles (2006):

$$\sigma = \alpha\varepsilon - \beta\varepsilon^3 + \rho\nu\frac{\partial\varepsilon}{\partial t} - \rho\lambda\frac{\partial^2\varepsilon}{\partial Z^2}, \tag{2}$$

where ρ is the density of the material, ν is a viscosity and λ accounts for the energy required to create an interface. I assume that the compression front travels at velocity v and define a new variable $\xi = Z - vt$. Since the stress σ in our sample is constant I wish to find a profile for $\varepsilon(z,t)$ that satisfies

$$\rho\lambda\frac{d^2\varepsilon}{d\xi^2} + \rho\nu v\frac{d\varepsilon}{d\xi} + \alpha\varepsilon - \beta\varepsilon^3 + \sigma = 0, \tag{3}$$

with remote conditions $\varepsilon \to \varepsilon^+$ as $\xi \to \infty$ and $\varepsilon \to \varepsilon^-$ as $\xi \to -\infty$. It is easy to show that

$$\varepsilon(z,t) = a + b\tanh(\frac{Z - vt - Z_0}{c}), \tag{4}$$

gives such a profile for a particular choice of a, b, c and v that depend nonlinearly on α, β, ν, λ, ρ and σ. In particular, a is a solution to the cubic $\sigma + 2\alpha a - 8\beta a^3 = 0$, $b = \sqrt{\frac{\alpha}{\beta} - 3a^2}$, $c = \frac{2\rho\lambda}{\beta b^2}$ and $v = \sqrt{\frac{3\beta abc}{\rho\nu}}$. I recover Eqn. (5.1) by setting $v = 0$, justifying its use to fit the strain profile in our compressed samples. Note that in accordance with our assumption in Eqn. (5.19) the front velocity v in this augmented theory depends on σ. A sharp front corresponds to the limit as $c \to 0$. In this limit the dissipation caused by the motion of the front can be captured by a kinetic equation like Eqn. (5.19) as in Abeyaratne & Knowles (2006).

Sensitivity analysis of fitting in PPP and PRP

In section 6.2.9, we fitted the low strain rate, small compression degree compression experiments on PPP and PRP clots using several different material parameters. Each material parameter has its physical meaning; for example, E_L is the Young's modulus in the rarefied phase, σ_{pre} is a pre-stress, both of which can be read off from the stress-strain plot and have a clear physical basis that has been explained in the text. However, although the mobility parameters M_{LH} and M_{HL} represent how fast the phase boundary between rarefied and densified regions moves due to external loading, it is difficult to design an
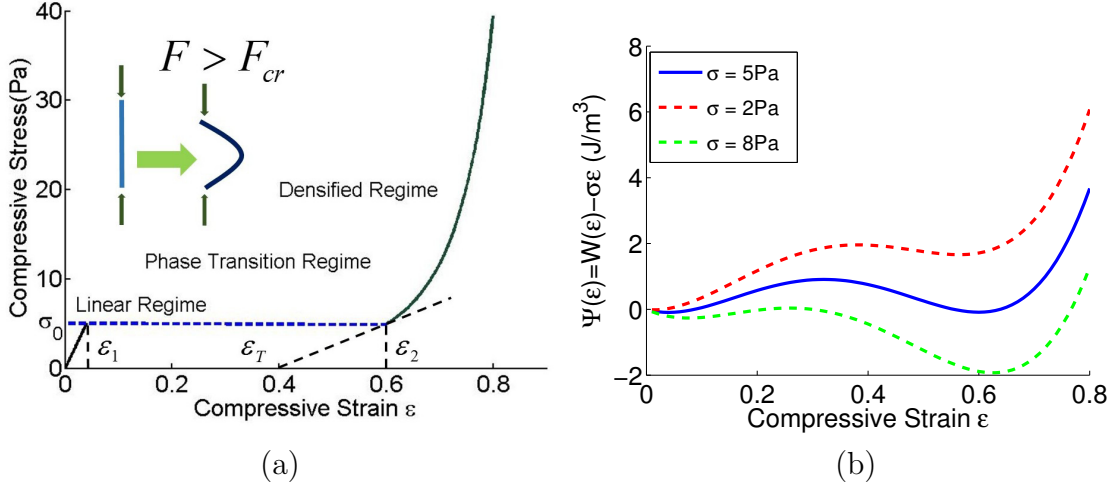
Figure 1: (a) The tri-phasic stress-strain response of such a material assuming quasi-static loading. Theoretical curves are plotted according to Eqns. (5.3) and (5.8). I have used $l = 1.32\mu$m, $d = 0.22\mu$m, $\nu = 0.1\mu$m^{-3}, and the two coefficients $n = 3$, $k = 0.5$ corresponding to a fibrin network.(b)Multi-well Gibbs free energy landscape for various stresses. At the plateau stress $\sigma = 5$Pa both wells are at equal height, meaning that the straight and densified phases of the network can co-exist. For lower σ the straight phase has lower energy and for higher σ the densified phase has lower energy.

experiment to directly measure them. Here we present a sensitivity analysis by varying our fitting result of M_{LH} and M_{HL} by $\pm 10\%$. The results are shown using dashed lines in Figure 2. The dashed line are very close to the solid lines indicating the sensitivity of our results to a change in mobilities is very small.

Compression of clots under high compression rate 100 μm/s

We have observed changes in the structure of whole blood clots during compression/ decompression as shown in Figure 3. We have also done high strain-rate compression experiments on PPP, PRP, as well as whole blood clot samples. The experimental data of whole blood clot samples are shown in Figure 4.

Oscillatory shear of PPP, PRP, and whole blood in different cycles

We have done oscillatory shear experiments on PPP, PRP, and whole blood clot samples in three different cycles, and measured the shear storage and loss moduli at the beginning
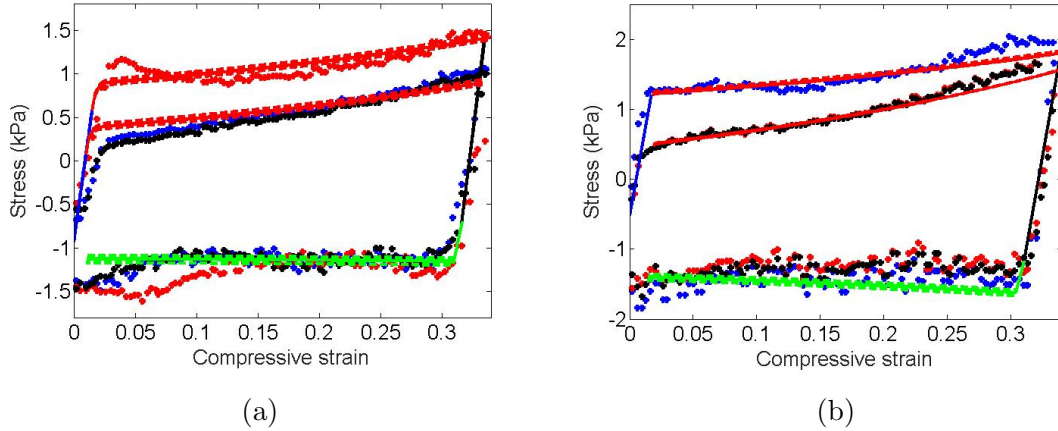
Figure 2: Sensitivity analysis of fitting of the plateau region in the (a) PPP and (b) PRP low strain rate, small compression degree experiments. The coloring scheme for the lines and dots is the same (Figure 6.4). Changing the mobilities M_{LH} and M_{HL} by $\pm 10\%$ does not affect the curves by much.

and end of each of each compression/decompression. The experimental data are shown in Table 1.

Fitting the CNT uniaxial compression experiment using a piece-wise linear stress-strain relation

Our goal here is to show that a piece-wise linear stress-strain law, like the one I used to describe the nano-indentation experiment, can also quantitatively capture the stress-strain plots of the uniaxal compression experiments. In the main text I had used a non-linear relation to model the densified phase which I could not exploit in the solution of the Boussinesq problem for nanoindentation. A piece-wise linear stress-strain relation for the rarefied and densified phases is:

$$
\begin{aligned}
\Gamma_L\left(\sigma\right) &= \frac{\sigma}{E_L}, \\
\Gamma_H\left(\sigma\right) &= \gamma_T + \frac{\sigma}{E_H},
\end{aligned}
\tag{5}
$$

We have used this to refit the compression experiment in Figure 5. The fitting parameters are summarized in Table 2. I compare them with the same parameters from nanoindentation and show the consistency.
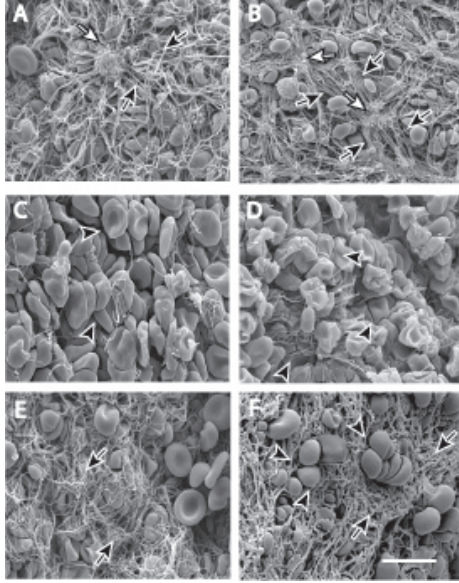
Figure 3: Structural changes in whole blood clots after the first cycle of compression decompression as observed by scanning electron microscopy The clots were compressed 2x at a rate of 10 μm/sec and decompressed at the same rate. (A, C, E) Control clots with no compression. (B, D, F) Clots after the first cycle of compression/decompression. (A) Whole blood clot before compression, showing the fibrin network. (B) Whole blood clot after compression, showing the changes to the fibrin network. Fibers stick to each other, and most of them were present as bundles. Also, some fibers stretched due to tension that was created by RBCs pushing on them. (C) Moderately deformed RBCs in the middle part of the clot before compression. (D) After the first cycle of compression decompression, many RBCs were deformed, with most of them being polyhedrocytes. (E) Clot with no compression, with this image being taken near the lateral edge of the clot. RBCs were slightly deformed. (F) Decompressed clot, and images taken from the lateral edge of the clot. Fibers are denser with smaller pore size. Some RBCs were deformed to a balloon - like shape, as if they were trapped while trying to escape from the network. Black arrows indicate the fibrin network; white arrows point to platelets; black arrowheads point to RBCs. Magnification bar = 10 μm.

Predicting phase boundary using Hertz contact solution for a paraboloid indenter

Following Johnson (1974), the vertical stress along the z-axis ($r = 0$) in the Hertz contact problem can be calculated as

$$\sigma_z\left(0, z\right) = \frac{3P}{2\pi a^2\left(1 + z^2/a^2\right)}, \tag{6}$$

148
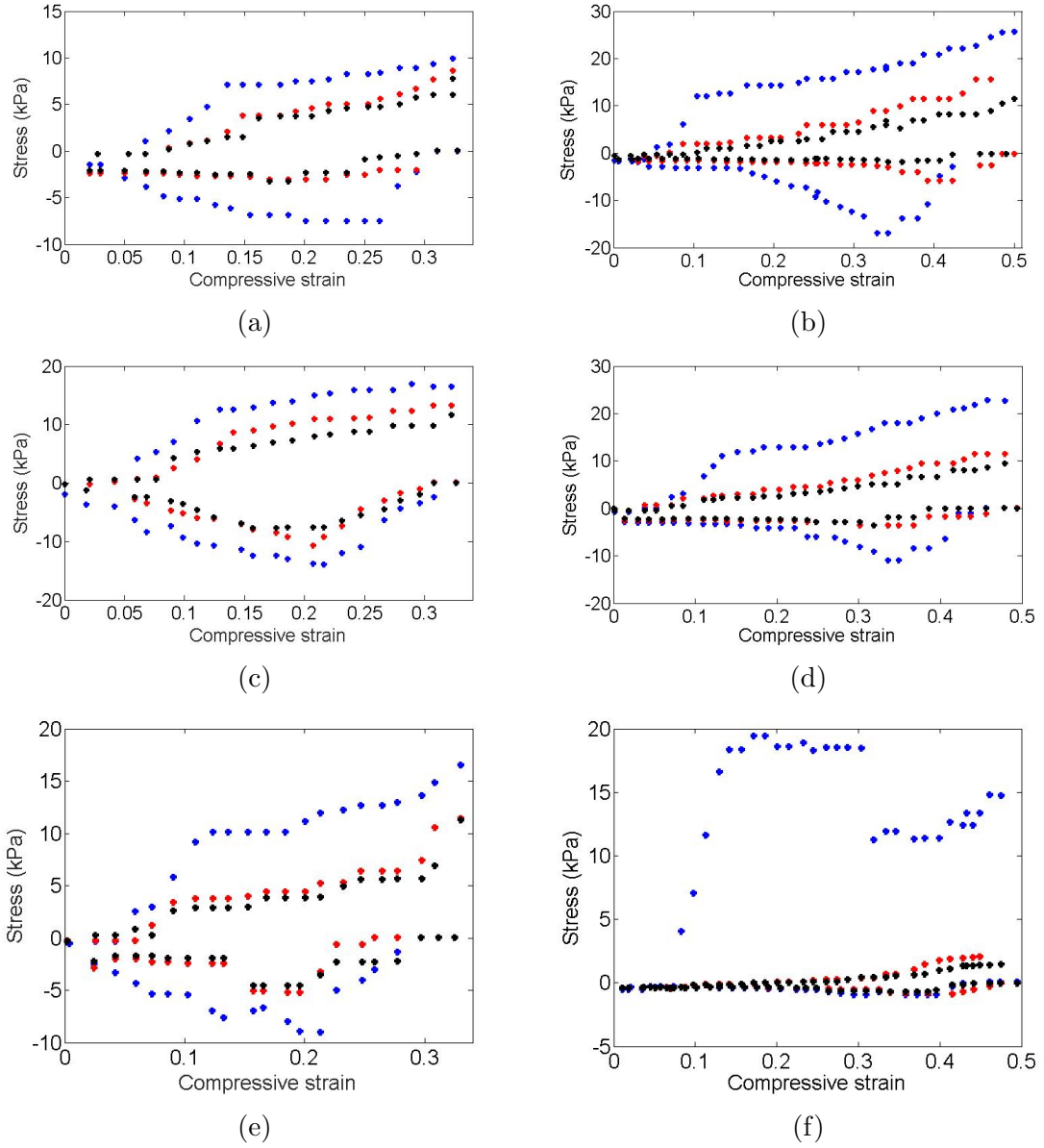
Figure 4: (a) (b) Experimental data for PPP high strain rate experiments (dots), both small and large compression degree. (c) (d) Experimental data for PRP high strain rate experiments (dots), both small and large compression degree. (e) (f) Experimental data for whole blood high strain rate experiments (dots), both small and large compression degree.

where a is the radius of the contact area between the indenter and half-space. a is related to the total load P and reduced Young's modulus E as:

$$a = \left(\frac{3PR}{4E}\right)^{1/3}, \tag{7}$$

Table 1: Shear storage and loss moduli of PPP, PRP, whole blood clots in each compression-decompression cycle. Here 1st means before compression; 2nd means after one compression; 3rd means after one decompression; 4th means after the second compression; 5th means after the second decompression; 6th means after the third compression; 7th means after the third decompression.

Group	1st G'	2nd G'	3rd G'	4th G'	5th G'	6th G'	7th G'
PPP clot 2X G'	285±48	32±1	750±2	33±1	855±1	33.5±0.6	866 ±1
PPP clot 1.5X G'	122±15	22.5±0.4	397±2	24.6±0.5	494±1	24.0±0.5	515±1
PRP clot 2X G'	228±19	31±1	487±1	30.4±1.1	640±3	33.3±1.0	754 ± 3
PRP clot 1.5X G'	175±11	31.6±1.2	305±1	32.1±0.8	364±1	33±1	389±1
Whole blood clot 2X G'	151±4	13.9±0.3	36.1±0.6	12.3±0.4	41.2±0.3	11.7±0.2	43.9±0.3
Whole blood clot 1.5X G'	102±4	18.9±0.5	56.4±1.1	17.8±0.5	66.3±0.7	18.2±0.4	73.9±0.4

Group	1st G''	2nd G''	3rd G''	4th G''	5th G''	6th G''	7th G''
PPP clot 2X G''	5.5±1.6	5.5±0.1	19.6±0.8	4.8±0.1	22.2±1.1	4.6±0.1	22.3±1.4
PPP clot 1.5X G''	12.7 ±4.3	9.3±0.1	33.8 ±0.6	8.5±0.1	35.7±1.0	8.2±0.1	36.2±0.8
PRP clot 2X G''	20.1±3.1	6.3±0.1	27.4±0.5	5.7± 0.1	32.0±0.7	5.8±0.1	34.4±1.4
PRP clot 1.5X G''	9.5±0.9	5.8±0.2	18.6±1.5	5.6±0.1	19.0±2.0	5.3±0.2	20.1±2.4
Whole blood clot 2X G''	10.1±.0.1	2.5±0.1	2.7±0.1	1.8±0.1	2.8±0.2	1.7±0.1	3.0±0.1
Whole blood clot 1.5X G''	7.3±0.4	2.6±0.12	4.4±0.5	2.5±0.1	4.5±0.3	2.4±0.1	4.8±0.1

All moduli are in units of Pa.
Number before X indicates compression degree.
All the experiments are performed at compression rate of 100 μm/s.

where R is the curvature of indenter. $R = 1$ μm in our indentation experiment. The Hertz solution is a good approximation only for small peak loads at which the indentation depths are much smaller than R. I can now predict the position of the phase boundary z_p at each peak load in the nanoindentation experiment using the equivalent E extracted from experiment for that peak load and setting $\sigma_z = \sigma_{LH}$ in Eqn. (6). I compare z_p from the Hertz solution against those from the point load (Boussinesq) solution in Table 2. z_p is smaller for the Hertz solution in all cases because the point load is spread over a small area
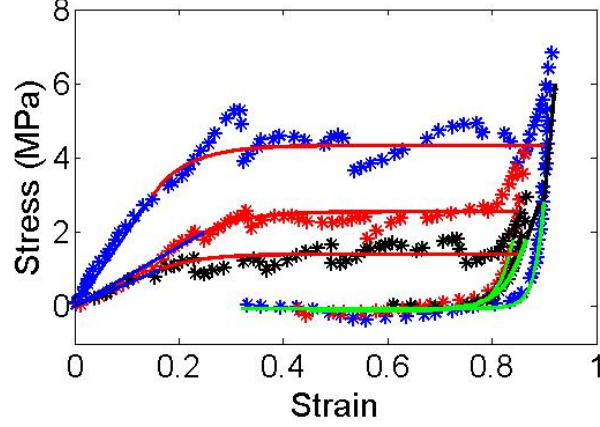
Figure 5: Fitting of compression experiment using a linear stress-strain relation in densified phase for bare CNT (black dots), ALD 5 cycles (red dots) and ALD 10 cycles pillars(blue dots). The lines are obtained from the phase transition model with parameters listed Table 2.

Table 2: Comparison of linear phase transition model parameters used in nanoindentation vs compression, and comparison of phase boundary position z_p predicted from Boussinesq vs. Hertz solutions.

Group	Bare CNTs	CNTs with 5 ALD cycles	CNTs with 10 ALD cycles
E_L(MPa) (indentation)	6.14±0.42	5.44±1.01	13.30±1.11
E_L(MPa) (compression)	6	8	20
E_H(MPa) (indentation)	38.82±0.89	62.76±1.58	111.11±2.33
E_H(MPa) (compression)	40	60	150
γ_T (indentation)	0.562±0.007	0.655±0.044	0.362±0.026
γ_T (compression)	0.747	0.70	0.76
z_p (μm) at P_2 (Boussinesq)	2.19	1.55	1.13
z_p (μm) at P_2 (Hertz)	1.92	1.22	0.89
z_p (μm) at P_3 (Boussinesq)	2.68	1.88	1.38
z_p (μm) at P_3 (Hertz)	2.40	1.54	1.13
z_p (μm) at P_4 (Boussinesq)	3.10	2.17	1.60
z_p (μm) at P_4 (Hertz)	2.81	1.82	1.33

in the Hertz solution. z_p changes by the same amount in both solutions as I go from P_2 to P_3, or P_3 to P_4.

Bibliography

Abad, J., Asorey, M. & Cruz, A. (1986), *New perspectives in quantum field theories: proceedings*, World Scientific.

Abeyaratne, R. & Knowles, J. K. (2006), *Evolution of phase transitions: a continuum theory*, Cambridge University Press.

Abraham, F. F. & Nelson, D. R. (1990), 'Diffraction from polymerized membranes', *Science* **249**(4967), 393–397.

Agrawal, H., Liu, L. & Sharma, P. (2016), 'Revisiting the curvature-mediated interactions between proteins in biological membranes', *Soft Matter* **12**(43), 8907–8918.

Agrawal, N. J. & Radhakrishnan, R. (2009), 'Calculation of free energies in fluid membranes subject to heterogeneous curvature fields', *Physical Review E* **80**(1), 011925.

Akbulut, S., Ocak, Y., Maraşlı, N., Keşlioğlu, K., Böyük, U., Çadırlı, E. & Kaya, H. (2008), 'Interfacial energy of solid in 2 bi intermetallic phase in equilibrium with in–bi eutectic liquid at 72 c equilibrating temperature', *Materials Characterization* **59**(8), 1101–1110.

Audoly, B. & Pomeau, Y. (2010), *Elasticity and geometry*, Oxford University Press.

Auth, T. & Gompper, G. (2013), 'Fluctuation pressure of biomembranes in planar confinement', *Physical Review E* **88**(1), 010701.

Bao, W., Miao, F., Chen, Z., Zhang, H., Jang, W., Dames, C. & Lau, C. N. (2009), 'Controlled ripple texturing of suspended graphene and ultrathin graphite membranes', *Nature nanotechnology* **4**(9), 562–566.

Barbier, C., Dendievel, R. & Rodney, D. (2009), 'Role of friction in the mechanics of nonbonded fibrous materials', *Physical Review E* **80**(1), 016115.

Bathe, K.-J. (2006), *Finite element procedures*, Klaus-Jurgen Bathe.

Baumgart, T., Hess, S. T. & Webb, W. W. (2003), 'Imaging coexisting fluid domains in biomembrane models coupling curvature and line tension', *Nature* **425**(6960), 821–824.

Bhattacharya, K. (1999), 'Phase boundary propagation in a heterogeneous body', *Proceedings: Mathematical, Physical and Engineering Sciences* pp. 757–766.

Bhattacharya, K. (2003), *Microstructure of martensite: why it forms and how it gives rise to the shape-memory effect*, Vol. 2, Oxford University Press.

Blesgen, T., Fraternali, F., Raney, J., Amendola, A. & Daraio, C. (2012), 'Continuum limits of bistable spring models of carbon nanotube arrays accounting for material damage', *Mechanics Research Communications* **45**, 58–63.

Boal, D. & Boal, D. H. (2012), *Mechanics of the Cell*, Cambridge University Press.

Bonn, D., de Cagny, H. C., Vos, B. E., Vahabi, M., Kurniawan, N. A., Koenderink, G. H., MacKintosh, F. C. et al. (2016), 'Porosity governs normal stresses in polymer gels'.

Bouaziz, O., Masse, J., Allain, S., Orgéas, L. & Latil, P. (2013), 'Compression of crumpled aluminum thin foils and comparison with other cellular materials', *Materials Science and Engineering: A* **570**, 1–7.

Brown, A. E., Litvinov, R. I., Discher, D. E., Purohit, P. K. & Weisel, J. W. (2009), 'Multiscale mechanics of fibrin polymer: gel stretching with protein unfolding and loss of water', *science* **325**(5941), 741–744.

Bunch, J. S., Van Der Zande, A. M., Verbridge, S. S., Frank, I. W., Tanenbaum, D. M., Parpia, J. M., Craighead, H. G. & McEuen, P. L. (2007), 'Electromechanical resonators from graphene sheets', *Science* **315**(5811), 490–493.

Burstein, M. & Lewi, S. (1952), 'Platelets and structure of the plasma clot; the mode of action of platelets during retraction', *Comptes rendus des séances de la Société de biologie et de ses filiales* **146**(11-12), 829.

Cao, A., Dickrell, P. L., Sawyer, W. G., Ghasemi-Nejhad, M. N. & Ajayan, P. M. (2005), 'Super-compressible foamlike carbon nanotube films', *Science* **310**(5752), 1307–1310.

Chen, C., Lu, T. & Fleck, N. (2001), 'Effect of inclusions and holes on the stiffness and strength of honeycombs', *International Journal of Mechanical Sciences* **43**(2), 487–504.

Chen, L. & Rong, Y. (2010), 'Digital topological method for computing genus and the betti numbers', *Topology and its Applications* **157**(12), 1931–1936.

Choong, L. T., Mannarino, M. M., Basu, S. & Rutledge, G. C. (2013), 'Compressibility of electrospun fiber mats', *Journal of Materials Science* **48**(22), 7827–7836.

Christian, J. W. (2002), *The theory of transformations in metals and alloys*, Pergamon Press, Oxford, U.K.

Cines, D. B., Lebedeva, T., Nagaswami, C., Hayes, V., Massefski, W., Litvinov, R. I., Rauova, L., Lowery, T. J. & Weisel, J. W. (2014), 'Clot contraction: compression of erythrocytes into tightly packed polyhedra and redistribution of platelets and fibrin', *Blood* **123**(10), 1596–1603.

Collet, J. P., Montalescot, G., Lesty, C. & Weisel, J. (2002), 'A structural and dynamic investigation of the facilitating effect of glycoprotein iib/iiia inhibitors in dissolving platelet-rich clots', *Circulation research* **90**(4), 428–434.

Collet, J.-P., Shuman, H., Ledger, R. E., Lee, S. & Weisel, J. W. (2005), 'The elasticity of an individual fibrin fiber in a clot', *Proceedings of the National Academy of Sciences of the United States of America* **102**(26), 9133–9137.

Corey, J. M., Lin, D. Y., Mycek, K. B., Chen, Q., Samuel, S., Feldman, E. L. & Martin, D. C. (2007), 'Aligned electrospun nanofibers specify the direction of dorsal root ganglia neurite growth', *Journal of Biomedical Materials Research Part A* **83**(3), 636–645.

Craig, R. F. (2013), *Soil mechanics*, Springer.

D, L. L. & M., L. E. (1980), *Statistical Physics: Theory of the Condensed State*, Butterworth-Heinemann.

Dao, M., Lim, C. T. & Suresh, S. (2003), 'Mechanics of the human red blood cell deformed by optical tweezers', *Journal of the Mechanics and Physics of Solids* **51**(11), 2259–2280.

Davami, K., Jiang, Y., Cortes, J., Lin, C., Shaygan, M., Turner, K. T. & Bargatin, I. (2016), 'Tuning the mechanical properties of vertical graphene sheets through atomic layer deposition', *Nanotechnology* **27**(15), 155701.

Discher, D., Mohandas, N., Evans, E. et al. (1994), 'Molecular maps of red cell deformation: hidden elasticity and in situ connectivity', *SCIENCE-NEW YORK THEN WASHINGTON-* pp. 1032–1032.

Dommersnes, P. G. & Fournier, J.-B. (2002), 'The many-body problem for anisotropic membrane inclusions and the self-assembly of saddle defects into an egg carton', *Biophysical journal* **83**(6), 2898–2905.

Eberl, C., Thompson, R., Gianola, D., Sharpe Jr, W. & Hemker, K. (2006), 'Digital image correlation and tracking', *MatLabCentral, Mathworks file exchange server, FileID* **12413**.

Evans, E. A. (1974), 'Bending resistance and chemically induced moments in membrane bilayers', *Biophysical journal* **14**(12), 923.

Evans, E. & Hochmuth, R. (1976), 'Membrane viscoelasticity', *Biophysical Journal* **16**(1), 1–11.

Evans, E. & Rawicz, W. (1990), 'Entropy-driven tension and bending elasticity in condensed-fluid membranes', *Physical Review Letters* **64**(17), 2094.

Farsad, K., Ringstad, N., Takei, K., Floyd, S. R., Rose, K. & De Camilli, P. (2001), 'Generation of high curvature membranes mediated by direct endophilin bilayer interactions', *The Journal of cell biology* **155**(2), 193–200.

Fasolino, A., Los, J. & Katsnelson, M. I. (2007), 'Intrinsic ripples in graphene', *Nature materials* **6**(11), 858–861.

Finnie, I. & Patel, M. (1970), 'Structural features and mechanical properties of rigid cellular plastics(rigid cellular plastics mechanical properties based on model assuming pentagonal dodecahedron cell form)', *Journal of Materials* **5**, 909–932.

Fletcher, D. A. & Mullins, R. D. (2010), 'Cell mechanics and the cytoskeleton', *Nature* **463**(7280), 485–492.

Flory, P., Volkenstein, M. et al. (1969), 'Statistical mechanics of chain molecules'.

Franck, C., Hong, S., Maskarinec, S., Tirrell, D. & Ravichandran, G. (2007), 'Three-dimensional full-field measurements of large deformations in soft materials using confocal microscopy and digital volume correlation', *Experimental Mechanics* **47**(3), 427–438.

Fraternali, F., Blesgen, T., Amendola, A. & Daraio, C. (2011), 'Multiscale mass-spring models of carbon nanotube foams', *Journal of the Mechanics and Physics of Solids* **59**(1), 89–102.

Fraternali, F. & Marcelli, G. (2012), 'A multiscale approach to the elastic moduli of biomembrane networks', *Biomechanics and modeling in mechanobiology* **11**(7), 1097–1108.

Fung, Y.-c. (1965), *Foundations of solid mechanics*, Prentice Hall.

Gaitanaros, S., Kyriakides, S. & Kraynik, A. M. (2012), 'On the crushing response of random open-cell foams', *International Journal of Solids and Structures* **49**(19), 2733–2743.

Garcia-Sanchez, D., van der Zande, A. M., Paulo, A. S., Lassagne, B., McEuen, P. L. & Bachtold, A. (2008), 'Imaging mechanical vibrations in suspended graphene sheets', *Nano letters* **8**(5), 1399–1403.

Gent, A. & Thomas, A. (1963), 'Mechanics of foamed elastic materials', *Rubber Chemistry and Technology* **36**(3), 597–610.

Gent, A. & Thomas, A. G. (1959), 'The deformation of foamed elastic materials', *Journal of Applied Polymer Science* **1**(1), 107–113.

Gersh, K. C., Nagaswami, C. & Weisel, J. W. (2009), 'Fibrin network structure and clot mechanical properties are altered by incorporation of erythrocytes', *Thrombosis and haemostasis* **102**(6), 1169.

Gibson, L. J. (2005), 'Biomechanics of cellular solids', *Journal of biomechanics* **38**(3), 377–399.

Gibson, L. J. & Ashby, M. F. (1982), The mechanics of three-dimensional cellular materials, *in* 'Proceedings of the Royal Society of London A: Mathematical, Physical and Engineering Sciences', Vol. 382, The Royal Society, pp. 43–59.

Gibson, L. J. & Ashby, M. F. (1999), *Cellular solids: structure and properties*, Cambridge university press.

Golestanian, R., Goulian, M. & Kardar, M. (1996), 'Fluctuation-induced interactions between rods on a membrane', *Physical Review E* **54**(6), 6725.

Gompper, G. & Kroll, D. (1996), 'Random surface discretizations and the renormalization of the bending rigidity', *Journal de Physique I* **6**(10), 1305–1320.

Guidotti, G. (1972), 'Membrane proteins', *Annual review of biochemistry* **41**(1), 731–752.

Hanlumyuang, Y., Liu, L. & Sharma, P. (2014), 'Revisiting the entropic force between fluctuating biological membranes', *Journal of the Mechanics and Physics of Solids* **63**, 179–186.

Harmandaris, V. A. & Deserno, M. (2006), 'A novel method for measuring the bending rigidity of model lipid membranes by simulating tethers', *The Journal of chemical physics* **125**(20), 204905.

He, Y., Li, H., Si, P., Li, Y., Yu, H., Zhang, X., Ding, F., Liew, K. M. & Liu, X. (2011), 'Dynamic ripples in single layer graphene', *Applied Physics Letters* **98**(6), 063101.

Helfrich, W. (1973), 'Elastic properties of lipid bilayers: theory and possible experiments', *Zeitschrift für Naturforschung C* **28**(11-12), 693–703.

Helfrich, W. (1975), 'Out-of-plane fluctuations of lipid bilayers', *Zeitschrift für Naturforschung C* **30**(11-12), 841–842.

Hochmuth, R., Worthy, P. & Evans, E. (1979), 'Red cell extensional recovery and the determination of membrane viscosity.', *Biophysical journal* **26**(1), 101.

Howard, J. et al. (2001), 'Mechanics of motor proteins and the cytoskeleton'.

Huang, C., Yuan, H. & Zhang, S. (2011), 'Coupled vesicle morphogenesis and domain organization', *Applied Physics Letters* **98**(4), 043702.

Hughes, T. J. R. (2000), *The Finite Element Method*, Dover Publications, Mineola, NY.

Huisman, E. M., van Dillen, T., Onck, P. R. & Van der Giessen, E. (2007), 'Three-dimensional cross-linked f-actin networks: relation between network architecture and mechanical behavior', *Physical review letters* **99**(20), 208103.

Hutchens, S. B., Hall, L. J. & Greer, J. R. (2010), 'In situ mechanical testing reveals periodic buckle nucleation and propagation in carbon nanotube bundles', *Advanced Functional Materials* **20**(14), 2338–2346.

Hutchens, S. B., Needleman, A. & Greer, J. R. (2012), 'A microstructurally motivated description of the deformation of vertically aligned carbon nanotube structures', *Applied Physics Letters* **100**(12), 121910.

Israelachvili, J. N. (2011), *Intermolecular and surface forces*, Academic press.

Jahnel, M., Waigh, T. A. & Lu, J. R. (2008), 'Thermal fluctuations of fibrin fibres at short time scales', *Soft Matter* **4**(7), 1438–1442.

Jang, W.-Y. & Kyriakides, S. (2009), 'On the crushing of aluminum open-cell foams: Part i. experiments', *International Journal of Solids and Structures* **46**(3), 617–634.

Jen, C. J. & McIntire, L. V. (1982), 'The structural properties and contractile force of a clot', *Cell motility* **2**(5), 445–455.

Johnson, K. (1974), 'Contact mechanics, 1985'.

Jones, D. & Chadwick, G. (1970), 'Experimental measurement of the solid-liquid interfacial energies of transparent materials', *Philosophical Magazine* **22**(176), 291–300.

Kahraman, O., K. P. D. K. W. S. H. C. A. (2015), 'Architecture and function of membrane protein lattices', *Scientific Reports* **6**, 19214.

Kahraman, O., Koch, P. D., Klug, W. S. & Haselwandter, C. A. (2016), 'Architecture and function of mechanosensitive membrane protein lattices', *Scientific reports* **6**.

Keşlioğlu, K. & Maraşlı, N. (2004), 'Solid–liquid interfacial energy of the eutectoid β phase in the al–zn eutectic system', *Materials Science and Engineering: A* **369**(1), 294–301.

Kim, K., Neu, J. & Oster, G. (1998), 'Curvature-mediated interactions between membrane proteins', *Biophysical journal* **75**(5), 2274–2291.

Kim, O. V., Liang, X., Litvinov, R. I., Weisel, J. W., Alber, M. S. & Purohit, P. K. (2016), 'Foam-like compression behavior of fibrin networks', *Biomechanics and modeling in mechanobiology* **15**(1), 213–228.

Kim, O. V., Litvinov, R. I., Weisel, J. W. & Alber, M. S. (2014), 'Structural basis for the nonlinear mechanics of fibrin networks under compression', *Biomaterials* **35**(25), 6739–6749.

Kim, O. V., Xu, Z., Rosen, E. D. & Alber, M. S. (2013), 'Fibrin networks regulate protein transport during thrombus development', *PLOS Comput Biol* **9**(6), e1003095.

Ko, W. (1965), 'Deformations of foamed elastomers', *Journal of Cellular Plastics* **1**(1), 45–50.

Koiter, W. (1964), 'On the dynamic boundary conditions in the theory of thin shells', *Proc. Konikl. Ned. Acad. Wetenscap* pp. 117–126.

Košmrlj, A. & Nelson, D. R. (2014), 'Thermal excitations of warped membranes', *Physical Review E* **89**(2), 022126.

Kumar, A., Maschmann, M. R., Hodson, S. L., Baur, J. & Fisher, T. S. (2015), 'Carbon nanotube arrays decorated with multi-layer graphene-nanopetals enhance mechanical strength and durability', *Carbon* **84**, 236–245.

Kurniawan, N. A., Vos, B. E., Biebricher, A., Wuite, G. J., Peterman, E. J. & Koenderink, G. H. (2016), 'Fibrin networks support recurring mechanical loads by adapting their structure across multiple scales', *Biophysical Journal* **111**(5), 1026–1034.

Landau, L. & Lifshitz, E. (1986), *Theory of Elasticity, 3rd*, Pergamon Press, Oxford, UK.

Le Doussal, P. & Radzihovsky, L. (1992), 'Self-consistent theory of polymerized membranes', *Physical review letters* **69**(8), 1209.

Lee, C., Wei, X., Kysar, J. W. & Hone, J. (2008), 'Measurement of the elastic properties and intrinsic strength of monolayer graphene', *science* **321**(5887), 385–388.

Liang, X. & Purohit, P. K. (2016*a*), 'A fluctuating elastic plate and a cell model for lipid membranes', *Journal of the Mechanics and Physics of Solids* **90**, 29–44.

Liang, X. & Purohit, P. K. (2016*b*), 'A fluctuating elastic plate model applied to graphene', *Journal of Applied Mechanics* **83**(8), 081008.

Lim, C., Dao, M., Suresh, S., Sow, C. & Chew, K. (2004), 'Large deformation of living cells using laser traps', *Acta Materialia* **52**(7), 1837–1845.

Lin, L. C.-L., Gov, N. & Brown, F. L. (2006), 'Nonequilibrium membrane fluctuations driven by active proteins', *The Journal of chemical physics* **124**(7), 074903.

Lindahl, E. & Edholm, O. (2000), 'Mesoscopic undulations and thickness fluctuations in lipid bilayers from molecular dynamics simulations', *Biophysical journal* **79**(1), 426–433.

Lipowsky, R. & Girardet, M. (1990), 'Shape fluctuations of polymerized or solidlike membranes', *Physical review letters* **65**(23), 2893.

Lo, C.-M., Wang, H.-B., Dembo, M. & Wang, Y.-l. (2000), 'Cell movement is guided by the rigidity of the substrate', *Biophysical journal* **79**(1), 144–152.

Los, J., Katsnelson, M. I., Yazyev, O., Zakharchenko, K. & Fasolino, A. (2009), 'Scaling properties of flexible membranes from atomistic simulations: application to graphene', *Physical Review B* **80**(12), 121405.

Ma, X., Schickel, M. E., Stevenson, M. D., Sarang-Sieminski, A. L., Gooch, K. J., Ghadiali, S. N. & Hart, R. T. (2013), 'Fibers in the extracellular matrix enable long-range stress transmission between cells', *Biophysical journal* **104**(7), 1410–1418.

Magagnosc, D., Ehrbar, R., Kumar, G., He, M., Schroers, J. & Gianola, D. (2013), 'Tunable tensile ductility in metallic glasses', *Scientific reports* **3**.

Magid, E., Soldea, O. & Rivlin, E. (2007), 'A comparison of gaussian and mean curvature estimation methods on triangular meshes of range image data', *Computer Vision and Image Understanding* **107**(3), 139–159.

Maschmann, M. R., Ehlert, G. J., Park, S. J., Mollenhauer, D., Maruyama, B., Hart, A. J. & Baur, J. W. (2012), 'Visualizing strain evolution and coordinated buckling within cnt arrays by in situ digital image correlation', *Advanced Functional Materials* **22**(22), 4686–4695.

Maskarinec, S. A., Franck, C., Tirrell, D. A. & Ravichandran, G. (2009), 'Quantifying cellular traction forces in three dimensions', *Proceedings of the National Academy of Sciences* **106**(52), 22108–22113.

Masse, J.-P. & Poquillon, D. (2013), 'Mechanical behavior of entangled materials with or without cross-linked fibers', *Scripta Materialia* **68**(1), 39–43.

McCarter, C., Richards, R., Mesarovic, S. D., Richards, C., Bahr, D., McClain, D. & Jiao, J. (2006), 'Mechanical compliance of photolithographically defined vertically aligned carbon nanotube turf', *Journal of Materials Science* **41**(23), 7872–7878.

Mesarovic, S. D., McCarter, C., Bahr, D., Radhakrishnan, H., Richards, R., Richards, C., McClain, D. & Jiao, J. (2007), 'Mechanical behavior of a carbon nanotube turf', *Scripta materialia* **56**(2), 157–160.

Mezeix, L., Bouvet, C., Huez, J. & Poquillon, D. (2009), 'Mechanical behavior of entangled fibers and entangled cross-linked fibers during compression', *Journal of Materials Science* **44**(14), 3652–3661.

Milner, S. T. & Safran, S. (1987), 'Dynamical fluctuations of droplet microemulsions and vesicles', *Physical Review A* **36**(9), 4371.

Min, K. & Aluru, N. (2011), 'Mechanical properties of graphene under shear deformation', *Applied Physics Letters* **98**(1), 013113.

Mindlin, R. & Eshel, N. (1968), 'On first strain-gradient theories in linear elasticity', *International Journal of Solids and Structures* **4**(1), 109–124.

Mounet, N. & Marzari, N. (2005), 'First-principles determination of the structural, vibrational and thermodynamic properties of diamond, graphite, and derivatives', *Physical Review B* **71**(20), 205214.

Müller, M. M. & Deserno, M. (2010), 'Cell model approach to membrane mediated protein interactions', *Progress of Theoretical Physics Supplement* **184**, 351–363.

Nelson, D. & Peliti, L. (1987), 'Fluctuations in membranes with crystalline and hexatic order', *Journal de physique* **48**(7), 1085–1092.

Nelson, D., Piran, T. & Weinberg, S. (2004), *Statistical mechanics of membranes and surfaces*, World Scientific.

Ogden, R. W. (1997), *Non-linear elastic deformations*, Courier Corporation.

Oliver, W. C. & Pharr, G. M. (1992), 'An improved technique for determining hardness and elastic modulus using load and displacement sensing indentation experiments', *Journal of materials research* **7**(06), 1564–1583.

Onck, P., Koeman, T., Van Dillen, T. & Van der Giessen, E. (2005), 'Alternative explanation of stiffening in cross-linked semiflexible networks', *Physical review letters* **95**(17), 178102.

Pan, W., Xiao, J., Zhu, J., Yu, C., Zhang, G., Ni, Z., Watanabe, K., Taniguchi, T., Shi, Y. & Wang, X. (2012), 'Biaxial compressive strain engineering in graphene/boron nitride heterostructures', *Scientific reports* **2**.

Pannuzzo, M., Raudino, A., Milardi, D., La Rosa, C. & Karttunen, M. (2013), 'α-helical structures drive early stages of self-assembly of amyloidogenic amyloid polypeptide aggregate formation in membranes', *Scientific reports* **3**.

Park, S. J., Schmidt, A. J., Bedewy, M. & Hart, A. J. (2013), 'Measurement of carbon nanotube microstructure relative density by optical attenuation and observation of size-dependent variations', *Physical Chemistry Chemical Physics* **15**(27), 11511–11519.

Park, Y., Diez-Silva, M., Popescu, G., Lykotrafitis, G., Choi, W., Feld, M. S. & Suresh, S. (2008), 'Refractive index maps and membrane dynamics of human red blood cells parasitized by plasmodium falciparum', *Proceedings of the National Academy of Sciences* **105**(37), 13730–13735.

Pathak, S., Lim, E. J., Pour Shahid Saeed Abadi, P., Graham, S., Cola, B. A. & Greer, J. R. (2012), 'Higher recovery and better energy dissipation at faster strain rates in carbon nanotube bundles: an in-situ study', *ACS nano* **6**(3), 2189–2197.

Paulose, J., Vliegenthart, G. A., Gompper, G. & Nelson, D. R. (2012), 'Fluctuating shells under pressure', *Proceedings of the National Academy of Sciences* **109**(48), 19551–19556.

Piechocka, I. K., Bacabac, R. G., Potters, M., MacKintosh, F. C. & Koenderink, G. H. (2010), 'Structural hierarchy governs fibrin gel mechanics', *Biophysical journal* **98**(10), 2281–2289.

Purohit, P. K. (2001), Dynamics of phase transitions in strings, beams and atomic chains, PhD thesis, California Institute of Technology.

Purohit, P. K., Arsenault, M. E., Goldman, Y. & Bau, H. H. (2008), 'The mechanics of short rod-like molecules in tension', *International Journal of Non-Linear Mechanics* **43**(10), 1056–1063.

Purohit, P. K., Litvinov, R. I., Brown, A. E., Discher, D. E. & Weisel, J. W. (2011), 'Protein unfolding accounts for the unusual mechanical behavior of fibrin networks', *Acta biomaterialia* **7**(6), 2374–2383.

Qiu, A. & Bahr, D. F. (2013), 'The role of density in the mechanical response of cnt turfs', *Carbon* **55**, 335–342.

Qiu, A., Bahr, D., Zbib, A., Bellou, A., Mesarovic, S. D., McClain, D., Hudson, W., Jiao, J., Kiener, D. & Cordill, M. (2011), 'Local and non-local behavior and coordinated buckling of cnt turfs', *Carbon* **49**(4), 1430–1438.

Radhakrishnan, H., Mesarovic, S. D., Qiu, A. & Bahr, D. (2013), 'Phenomenological constitutive model for a cnt turf', *International Journal of Solids and Structures* **50**(14), 2224–2230.

Raj, R. & Purohit, P. K. (2011), 'Phase boundaries as agents of structural change in macromolecules', *Journal of the Mechanics and Physics of Solids* **59**(10), 2044–2069.

Ramakrishnan, N., Kumar, P. S. & Ipsen, J. H. (2010), 'Monte carlo simulations of fluid vesicles with in-plane orientational ordering', *Physical Review E* **81**(4), 041922.

Ramakrishnan, N., Kumar, P. S. & Radhakrishnan, R. (2014), 'Mesoscale computational studies of membrane bilayer remodeling by curvature-inducing proteins', *Physics reports* **543**(1), 1–60.

Raney, J., Fraternali, F. & Daraio, C. (2013), 'Rate-independent dissipation and loading direction effects in compressed carbon nanotube arrays', *Nanotechnology* **24**(25), 255707.

Raney, J. R., Wang, R. Y. & Daraio, C. (2013), 'Control of microstructural heterogeneities in carbon nanotube foams', *Carbon* **52**, 193–200.

Rekvig, L., Hafskjold, B. & Smit, B. (2004), 'Simulating the effect of surfactant structure on bending moduli of monolayers', *The Journal of chemical physics* **120**(10), 4897–4905.

Reynwar, B. J., Illya, G., Harmandaris, V. A., Müller, M. M., Kremer, K. & Deserno, M. (2007), 'Aggregation and vesiculation of membrane proteins by curvature-mediated interactions', *Nature* **447**(7143), 461–464.

Rodríguez-García, R., Mell, M., López-Montero, I., Netzel, J., Hellweg, T. & Monroy, F. (2011), 'Polymersomes: smart vesicles of tunable rigidity and permeability', *Soft Matter* **7**(4), 1532–1542.

Ruiz-Herrero, T. & Hagan, M. F. (2015), 'Simulations show that virus assembly and budding are facilitated by membrane microdomains', *Biophysical journal* **108**(3), 585–595.

Ryan, E. A., Mockros, L. F., Weisel, J. W. & Lorand, L. (1999), 'Structural origins of fibrin clot rheology', *Biophysical journal* **77**(5), 2813–2826.

Schweitzer, Y. & Kozlov, M. M. (2015), 'Membrane-mediated interaction between strongly anisotropic protein scaffolds', *PLoS Comput Biol* **11**(2), e1004054.

Shah, J. V. & Janmey, P. A. (1997), 'Strain hardening of fibrin gels and plasma clots', *Rheologica Acta* **36**(3), 262–268.

Sharma, R. C., Papagiannopoulos, A. & Waigh, T. A. (2008), 'Optical coherence tomography picorheology of biopolymer solutions', *Applied Physics Letters* **92**(17), 173903.

Silva, M. J., Hayes, W. C. & Gibson, L. J. (1995), 'The effects of non-periodic microstructure on the elastic properties of two-dimensional cellular solids', *International Journal of Mechanical Sciences* **37**(11), 1161–1177.

Simo, J. C. & Pister, K. S. (1984), 'Remarks on rate constitutive equations for finite deformation problems: computational implications', *Computer Methods in Applied Mechanics and Engineering* **46**(2), 201–215.

Stricker, J., Falzone, T. & Gardel, M. L. (2010), 'Mechanics of the f-actin cytoskeleton', *Journal of biomechanics* **43**(1), 9–14.

Su, T. & Purohit, P. K. (2010), 'Thermomechanics of a heterogeneous fluctuating chain', *Journal of the Mechanics and Physics of Solids* **58**(2), 164–186.

Su, T. & Purohit, P. K. (2011), 'Fluctuating elastic filaments under distributed loads', *Mol. Cell. Biomech* **8**, 215.

Su, T. & Purohit, P. K. (2012), 'Semiflexible filament networks viewed as fluctuating beam-frames', *Soft Matter* **8**(17), 4664–4674.

Thevamaran, R., Meshot, E. R. & Daraio, C. (2015), 'Shock formation and rate effects in impacted carbon nanotube foams', *Carbon* **84**, 390–398.

Toll, S. (1998), 'Packing mechanics of fiber reinforcements', *Polymer Engineering & Science* **38**(8), 1337–1350.

Torabi, H., Radhakrishnan, H. & Mesarovic, S. D. (2014), 'Micromechanics of collective buckling in cnt turfs', *Journal of the Mechanics and Physics of Solids* **72**, 144–160.

Toupin, R. A. (1962), 'Elastic materials with couple-stresses', *Archive for Rational Mechanics and Analysis* **11**(1), 385–414.

Tourdot, R. W., Ramakrishnan, N. & Radhakrishnan, R. (2014), 'Defining the free-energy landscape of curvature-inducing proteins on membrane bilayers', *Physical Review E* **90**(2), 022717.

Tripp, M. K., Stampfer, C., Miller, D. C., Helbling, T., Herrmann, C. F., Hierold, C., Gall, K., George, S. M. & Bright, V. M. (2006), 'The mechanical properties of atomic layer deposited alumina for use in micro-and nano-electromechanical systems', *Sensors and Actuators A: Physical* **130**, 419–429.

Truskinovsky, L. & Vainchtein, A. (2005), 'Kinetics of martensitic phase transitions: lattice model', *SIAM Journal on Applied Mathematics* **66**(2), 533–553.

Van der Burg, M., Shulmeister, V., Van der Geissen, E. & Marissen, R. (1997), 'On the linear elastic properties of regular and random open-cell foam models', *Journal of Cellular Plastics* **33**(1), 31–54.

Van Wyk, C. (1946), 'Note on the compressibility of wool', *Journal of the Textile Institute Transactions* **37**(12), T285–T292.

Volkov, A., Simiov, K. & Zhigilei, L. (2009), Mesoscopic simulation of self-assembly of carbon nanotubes into a network of bundles, *in* '47th AIAA Aerospace Sciences Meeting including The New Horizons Forum and Aerospace Exposition', p. 1544.

Vorjohann, S., Fish, R. J., Biron-Andreani, C., Nagaswami, C., Weisel, J. W., Boulot, P., Reyftmann, L., de Moerloose, P. & Neerman-Arbez, M. (2010), 'Hypodysfibrinogenaemia due to production of mutant fibrinogen alpha-chains lacking fibrinopeptide a and polymerisation knob a', *Thrombosis and haemostasis* **104**(5), 990.

Weeks, J. D. (1977), 'Structure and thermodynamics of the liquid–vapor interface', *The Journal of Chemical Physics* **67**(7), 3106–3121.

Weertman, J. & Weertman, J. R. (1992), 'Elementary dislocation theory'.

Weiner, J. H. (2012), *Statistical mechanics of elasticity*, Courier Corporation.

Weiss, P. & Katzberg, A. A. (1952), '" attraction fields" between growing tissue cultures', *Science* **115**(2985), 293–296.

Wen, Q. & Janmey, P. A. (2011), 'Polymer physics of the cytoskeleton', *Current Opinion in Solid State and Materials Science* **15**(5), 177–182.

Yang, Y., Bai, M., Klug, W. S., Levine, A. J. & Valentine, M. T. (2013), 'Microrheology of highly crosslinked microtubule networks is dominated by force-induced crosslinker unbinding', *Soft Matter* **9**(2), 383–393.

Yolcu, C., Haussman, R. C. & Deserno, M. (2014), 'The effective field theory approach towards membrane-mediated interactions between particles', *Advances in colloid and interface science* **208**, 89–109.

Yoon, D., Son, Y.-W. & Cheong, H. (2011), 'Negative thermal expansion coefficient of graphene measured by raman spectroscopy', *Nano letters* **11**(8), 3227–3231.

Yuan, H., Huang, C. & Zhang, S. (2011), 'Membrane-mediated inter-domain interactions', *BioNanoScience* **1**(3), 97–102.

Zacharia, R., Ulbricht, H. & Hertel, T. (2004), 'Interlayer cohesive energy of graphite from thermal desorption of polyaromatic hydrocarbons', *Physical Review B* **69**(15), 155406.

Zagar, G., Onck, P. R. & Van der Giessen, E. (2011), 'Elasticity of rigidly cross-linked networks of athermal filaments', *Macromolecules* **44**(17), 7026–7033.

Zakharchenko, K., Los, J., Katsnelson, M. I. & Fasolino, A. (2010), 'Atomistic simulations of structural and thermodynamic properties of bilayer graphene', *Physical Review B* **81**(23), 235439.

Zbib, A., Mesarovic, S. D., Lilleodden, E., McClain, D., Jiao, J. & Bahr, D. (2008), 'The coordinated buckling of carbon nanotube turfs under uniform compression', *Nanotechnology* **19**(17), 175704.

Zhang, Y. & Crothers, D. M. (2003), 'Statistical mechanics of sequence-dependent circular dna and its application for dna cyclization', *Biophysical journal* **84**(1), 136–153.

Zhao, Q. & Purohit, P. K. (2014), 'Extracting a kinetic relation from the dynamics of a bistable chain', *Modelling and Simulation in Materials Science and Engineering* **22**(4), 045004.

Zhao, Q. & Purohit, P. K. (2016), '(adiabatic) phase boundaries in a bistable chain with twist and stretch', *Journal of the Mechanics and Physics of Solids* **92**, 176–194.

Zhao, X., Strickland, D. J., Derlet, P. M., He, M.-r., Cheng, Y.-J., Pu, J., Hattar, K. & Gianola, D. S. (2015), 'In situ measurements of a homogeneous to heterogeneous transition in the plastic response of ion-irradiated¡ 111¿ ni microspecimens', *Acta Materialia* **88**, 121–135.